The decay $B^{\pm} \to D^0 K^{*\pm}$ and constraints on the angle γ of the unitarity triangle using the *BABAR* detector

Paul Stephen Jackson

Physics Department,
Royal Holloway, University of London

A thesis submitted to the University of London
for the Degree of Doctor of Philosophy.
September 2006.

Abstract

This thesis presents a study of the decay $B^- \to D^0 K^{*-}$ and its charge conjugate, $B^+ \to \overline{D}^0 K^{*+}$. It uses B mesons produced by the PEP-II e^+e^- accelerator and recorded by the *BABAR* detector at the Stanford Linear Accelerator Center in California. This study provides information on the matter anti-matter asymmetry known as CP violation by measuring the difference in decay rates of B^+ and B^- mesons. These measurements can be used by the Gronau-London-Wyler (GLW) method to quantify the amount of CP violation that occurs by constraining the angle γ of the unitarity triangle.

The GLW method requires several decays of $B^- \to D^0 K^{*-}$ and its charge conjugate to be studied. These decays can be separated into three categories based upon the decay of the D^0: non-CP eigenstates ($K^-\pi^+$, $K^-\pi^+\pi^0$, $K^-\pi^+\pi^-\pi^+$); CP-even eigenstates (K^+K^-, $\pi^+\pi^-$); CP-odd eigenstates ($K^0_S\pi^0$, $K^0_S\omega$, $K^0_S\phi$). The K^{*-} is reconstructed in the decay $K^{*-} \to K^-\pi^0$.

This analysis presents the measurement of four quantities which can be used to constrain the angle γ. These are the GLW CP parameters $\mathcal{A}_\pm$ and $\mathcal{R}_\pm$ which are specific functions of the decay rates mentioned above. This work is part of a wider effort within the *BABAR* collaboration to constrain γ by combining the results from several GLW analyses. A joint effort is required because the difficulty with these analyses is that they are statistically limited.

Using a dataset of 204 million $B\overline{B}$ pairs, the Gronau-London-Wyler CP parameters are measured to be:

$$
\begin{aligned}
\mathcal{A}_+ &= -0.40 \pm 0.40\ (\text{stat})\ \pm\ 0.19\ (\text{syst}),\\
\mathcal{A}_- &= -1.00 \pm 3.67\ (\text{stat})\ \pm\ 0.19\ (\text{syst}),\\
\mathcal{R}_+ &= 2.06 \pm 0.80\ (\text{stat})\ \pm\ 0.41\ (\text{syst}),\\
\mathcal{R}_- &= 0.19 \pm 0.50\ (\text{stat})\ \pm\ 0.30\ (\text{syst}).
\end{aligned}
$$

Declaration

The work presented in this thesis has been performed by myself.

Paul Stephen Jackson.

Contents

Acknowledgements

First I must thank Tania McMahon, my supervisor, for her support and encouragement over the course of this PhD. I also need to thank Glen Cowan for supervising me while Tania was on maternity leave, for all statistical advice and for helping in the final push to finish this thesis.

I would like to express my gratitude to Mike Green for his support, especially in the final months of this analysis. A big thank you goes to Stefania Ricciardi for always taking the time to answer my questions in detail.

I would like to thank Tania, Glen, Mike and Stefania once more for their careful reading and comments on this manuscript.

Thanks go to those students I have had the pleasure of working with while at Royal Holloway and while based at SLAC. Of particular note are Mark Winter, Clare Brown, Scott McGarvie, Matthew Barrett, David Hopkins and Guillaume Therin.

I have had the pleasure of attending RHUL for seven of the last eight years and so I would like to thank Thomas and Jane Holloway for founding Royal Holloway with the profits of quack medicine. I believe that the good achieved has out done the disappointment of those seeking cures for "gout, rheumatism, inverterate ulcers, sore breasts, sore heads, bad legs &c."

Thanks must go to my Mum and Dad who have always been there for me, and always been supportive of the goals I have set myself. Without their unwavering encouragement I'm sure that I would not have had the opportunity to perform these studies.

Most importantly I would like to thank my fiance, Alex. To list all of the ways in which she has supported me would take up more than this space allows, however, I must make special mention of her support when I quit a well paid job to "be a professional student", for putting up with me spending a year in America without her and for correcting the worst of my spelling and grammar before I passed drafts of this thesis to my supervisors. I may have done the work, but I feel that we met the challenge together, and I look forward to meeting many more together.

London, 13$^{\text{th}}$ September 2006.

Preface

This thesis describes original work performed by the author as part of the B Reconstruction Analysis Working Group (BReco AWG) within the *BABAR* collaboration.

The author has played a leading role in the work, in partnership with his supervisors Dr T. McMahon and Dr S. Ricciardi. Dr Ricciardi adapted the Mathematica model, created by Dr R. Kass of Ohio State University, to estimate the non-resonant systematic error.

List of Tables

List of Figures

Chapter 1

Introduction

The Standard Model of particle physics has been very successful at describing the interactions of quarks and leptons. It does however contain many free parameters including the masses of the quarks, leptons and the elements of the Cabibbo-Kobayashi-Maskawa (CKM) matrix. The presence of so many free parameters in the model suggests that it may not be the final word.

The natural way to look for new physics is to test the best models we currently have available. This analysis attempts to do this by studying the decay $B^- \to D^0 K^{*-}$ and its charge conjugate. By looking at the difference in the decay rates of the B^+ and B^- mesons CP violation can measured. This is done by using the Gronau-London-Wyler (GLW) method to constrain the angle γ of the unitarity triangle.

The GLW method makes use of the quantum mechanical interference that occurs between $B^- \to D^{(*)0} K^{(*)-}$ decays, which involve $b \to c\overline{u}s$ quark transitions, and $B^- \to \overline{D}^{(*)0} K^{(*)-}$ decays, which involve $b \to u\overline{c}s$ transitions. This analysis uses $B^- \to D^0 K^{*-}$ decays which can be split into three categories based upon the decay of the D^0: non-CP eigenstates ($K^-\pi^+$, $K^-\pi^+\pi^0$, $K^-\pi^+\pi^-\pi^+$); CP-even eigenstates (K^+K^-, $\pi^+\pi^-$); CP-odd eigenstates ($K^0_S\pi^0$, $K^0_S\omega$, $K^0_S\phi$). The K^{*-} is reconstructed in the decay $K^{*-} \to K^-\pi^0$.

The GLW method uses the measurement of these decay rates to form four quantities which can be used to constrain γ. These four quantities are:

$$\mathcal{A}_\pm = \frac{\Gamma_\pm(B^-) - \Gamma_\pm(B^+)}{\Gamma_\pm(B^-) + \Gamma_\pm(B^+)}, \tag{1.1}$$

$$\mathcal{R}_{\pm} = \frac{\Gamma_{\pm}(B^-) + \Gamma_{\pm}(B^+)}{\Gamma_{non-CP}(B^-) + \Gamma_{non-CP}(B^+).} \quad (1.2)$$

Here Γ is a decay rate and the subscript indicates the type of D^0 decay with $+$ indicating the use of CP-even modes, $-$ the use of CP-odd modes and non-CP the use of the non-CP modes.

Using the GLW method, this analysis was able to make a measurement of $\mathcal{A}_+$, $\mathcal{A}_-$, $\mathcal{R}_+$, and $\mathcal{R}_-$. Because of the low branching fraction of the D^0 decaying to CP eigenstates, analyses of this type are statistically limited. This means that the information from several analyses must be used in combination to provide a constraint on γ. This analysis forms part of this joint effort in the *BABAR* collaboration.

This thesis is structured as follows: Chapter 2 describes the theoretical background to the measurement made; Chapter 3 gives an overview of the accelerator and detector that have made the measurements possible; Chapter 4 details the preselection of events while Chapter 5 presents the final selection criteria; Chapter 6 describes the fit procedure used to measure the signal yields; Chapter 7 presents the results found and gives an assessment of the systematic errors of the measurements; Chapter 8 summarises the work performed, looks to the results' implications and discusses possible future improvements to the analysis.

Chapter 2

Theoretical overview

This chapter discusses the theoretical concepts related to this analysis and explains the reasons for choosing the B decay modes studied. Although the extraction of the angle γ is covered in detail, the rest of the chapter does not aim to give a complete overview of the subject as the Standard Model [1], [2] and CP violation [3] are well documented in textbooks. First a brief review of the Standard Model will be given. This leads to a discussion of the CKM matrix and the unitarity triangle. Next CP violation is defined before looking at how CP violation arises in B meson decays. An in-depth review of the method used to extract information about the weak phase γ is given. This is followed by a review of the current experimental status of related measurements.

2.1 The Standard Model

The Standard Model of particle physics is currently the best description available of the interactions of matter and the forces that propagate these interactions. Matter has been found to consist of three families of quarks and leptons. Each quark and lepton also has an anti-particle which has the same mass but opposite additive quantum numbers including its charge. Quarks have never been observed directly, they are always found in two or three quark bound states called mesons and baryons. There are currently searches ongoing for four and five quark bound states but nothing conclusive has been found to date.

The constituents of matter interact by exchanging gauge bosons. The four forces are gravity mediated by the graviton, the weak interaction with W and Z bosons,

the strong interaction with gluons and electromagnetism with photons.

The electromagnetic and weak forces can be seen as a unified electroweak force. The interactions involving the $W^{\pm}$ and Z^0 are weaker as their masses suppress the amplitudes where they are exchanged.

2.1.1 What is CP violation?

The C or charge conjugation operation reverses the charges of the constituents of a state. The P or parity operation reverses the spatial coordinates, therefore applying the CP operation reverses the charge, spatial coordinates and thus also the helicity of a state. CP violation is observed if the decay rate of a state is observed to differ from the rate of decay of its CP conjugate.

2.1.2 Is the Standard Model correct?

As accurate as its predictions are, the Standard Model is not expected to be the final word. The model contains 19 free parameters which include the masses of the quarks and leptons and the four free parameters of the CKM matrix. An additional 9 free parameters must be included if neutrinos with mass are included. Many people feel that a true underlying theory of the universe would not allow free parameters but would dictate the values of all (or most) quantities within the theory.

Another reason for believing that there is more to be discovered is the lack of understanding of the matter/antimatter asymmetry of the observable universe. It is expected that equal amounts of matter and antimatter should have been created in the earliest moments after the big bang. However, our experience is that there is relatively little antimatter around us. Observations of the universe show no distinctive signatures to suggest that other galaxies are made of antimatter. Although the Standard Model allows for the CP violation required in order for an asymmetry to arise, currently it is only possible to explain a tiny fraction of the difference observed [4, 5].

By testing all predictions of the Standard Model we are seeking to confirm the theory or discover new areas of physics. The B-factories like *BABAR* have been designed with the intention of measuring the CKM matrix and unitarity triangle as accurately as possible to test the Standard Model in this area.

2.2 The CKM matrix and unitarity triangle

The Cabibbo-Kobayashi-Maskawa (CKM) matrix relates the mass eigenstates to the weak eigenstates of the quarks. The elements of the CKM matrix V_{ij} are proportional to the coupling constants for decays where a quark changes flavour by emitting a $W^{\pm}$. It is only these charged current processes that have the ability to change the flavour of a quark. Figure 2.1 shows a diagram of this charged current interaction.

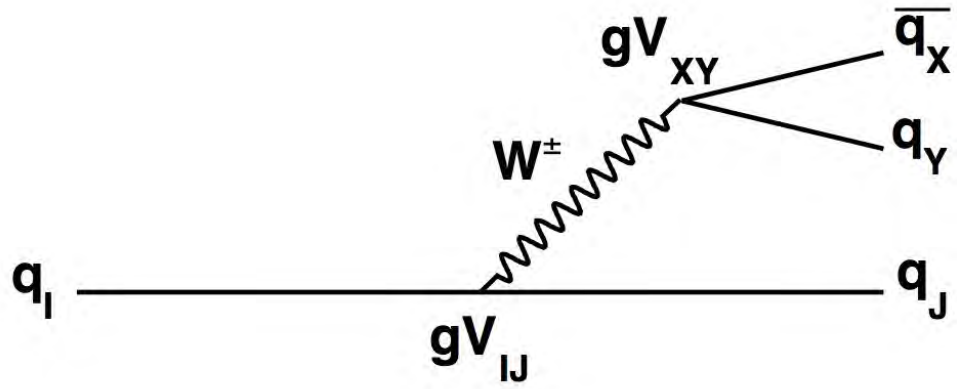

Figure 2.1: Feynman diagram of a quark flavour changing decay. For a W^+ decay $q_i = u$, c, t and $q_j = d$, s, b. Here g is the gauge coupling constant and V_{ij} is the required CKM matrix element.

Equation 2.1 shows how the CKM matrix relates the mass-eigenstates to the weak-eigenstates.

$$\begin{pmatrix} d' \\ s' \\ b' \end{pmatrix} = \begin{pmatrix} V_{ud} & V_{us} & V_{ub} \\ V_{cd} & V_{cs} & V_{cb} \\ V_{td} & V_{ts} & V_{tb} \end{pmatrix} \begin{pmatrix} d \\ s \\ b \end{pmatrix} . \tag{2.1}$$

The Standard Model requires that this matrix be unitary, i.e.,

$$VV^{\dagger} = I. \tag{2.2}$$

An arbitrary complex 3×3 matrix would have eighteen free parameters. The unitary nature gives nine constraints and an additional five constraints come from the freedom to redefine the phases of the quark states. So in the context of the Standard Model the CKM matrix has four free parameters.

The Wolfenstein parameterisation shown in Equation 2.3 is a convenient parameterisation of the elements of the CKM matrix. It contains four real parameters: λ,

A, ρ and η. The value of η determines the size of the imaginary component that leads to the possibility of complex coupling strengths, which allow CP violation to occur in the Standard Model. The size of the CP violating effect will be proportional to η and so a value of zero for this parameter will prevent CP violation from existing. The Wolfenstein parameterisation is not exactly unitary as shown by the $\mathcal{O}(\lambda^4)$ term in Equation 2.3.

$$V_{\mathrm{CKM}} = \begin{pmatrix} 1-\frac{\lambda^2}{2} & \lambda & A\lambda^3(\rho - i\eta) \\ -\lambda & 1-\frac{\lambda^2}{2} & A\lambda^2 \\ A\lambda^3(1-\rho-i\eta) & -A\lambda^2 & 1 \end{pmatrix} + \mathcal{O}(\lambda^4)\,. \tag{2.3}$$

Note that CP violation cannot arise in this way if there are only two families of quarks and leptons. This is because a 2×2 transformation matrix does not require a complex component. In the case of a 3×3 transformation matrix, in general, at least one element must have a complex component independent of the parameterisation chosen.

The unitarity of the CKM matrix allows the formation of six relations which must equal zero. These relations are formed from the summation of three terms and so can be represented as a triangle in the ρ, η plane of the Wolfenstein parameterisation. When referring to "the" unitary triangle, we are referring to the triangle where each of the sides are of most comparable length and hence each angle is also of most comparable size. This shorthand is used because four of the triangles that can be formed are actually flattened, two of the angles being much smaller, making the CP violation associated with those angles much harder to measure experimentally.

The unitarity triangle then is the triangle that in the complex plane (ρ, η) is represented by the relation:

$$V_{ud}V_{ub}^* + V_{cd}V_{cb}^* + V_{td}V_{tb}^* \;=\; 0. \tag{2.4}$$

Figure 2.2 shows these elements in the Wolfenstein parameterisation. It can be seen that the weak phase (γ) is given by

$$\gamma \;=\; Arg\left(-\frac{V_{ud}V_{ub}^*}{|V_{cd}V_{cb}^*|}\right). \tag{2.5}$$

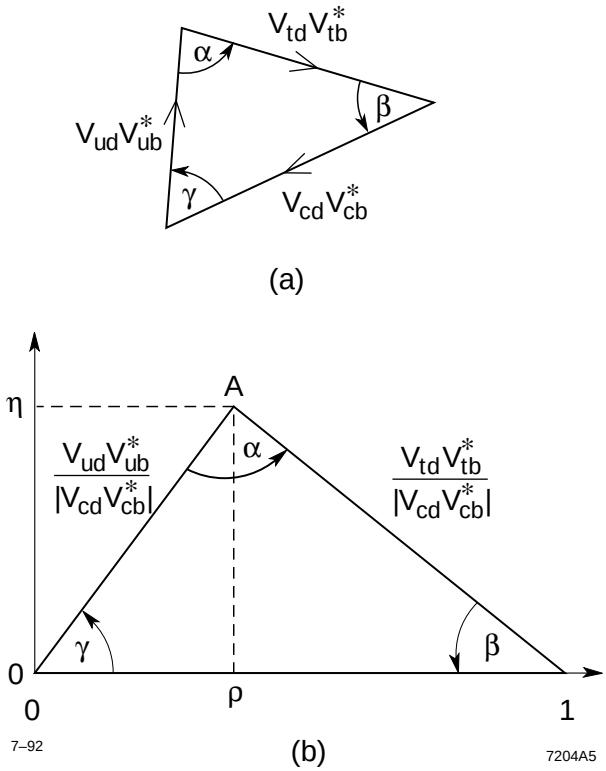

Figure 2.2: The unitarity triangle. (a) Shows an unscaled version. (b) Shows the triangle where all sides have been divided by $V_{cb}^* V_{cd}$ [6].

By substituting in the V_{ud} and V_{cd} elements taken from the Wolfenstein parameterisation (Equation 2.3) and ignoring terms of λ^2 we find

$$\gamma \;=\; Arg\left(-\frac{V_{ub}^*}{\lambda V_{cb}^*}\right). \tag{2.6}$$

Therefore to probe this angle, decays with $b \to u$ and $b \to c$ transitions are required. This points towards the need to use B mesons in order to constrain or measure γ directly.

2.3 CP violation in the B meson system

Three types of CP violation are possible: direct, indirect and interference. Each requires at least two paths from an initial state i to a final state f in order for quantum mechanical interference to occur [3].

Direct CP violation can occur when two diagrams interfere so that,

$$i \to f \quad \neq \quad \bar{i} \to \bar{f},$$

This is the type of CP violation that this analysis is trying to measure.

Indirect CP violation is where a meson can decay into its own anti-particle before decaying to the final state, but the reverse decay is not equally likely, that is

$$i \to \bar{i} \to f \quad \neq \quad \bar{i} \to i \to f.$$

CP violation arising from interference occurs when a B meson can decay both directly to the final state f, and via decaying to its own anti-particle before again decaying to f. The asymmetry arises if the anti-particle version has a different overall rate. These decays can be represented by:

$$\begin{array}{ccc} i \to f & & \bar{i} \to f \\ + & \neq & + \\ i \to \bar{i} \to f & & \bar{i} \to i \to f \end{array}$$

A charged B meson cannot exhibit indirect or mixing CP violation because charge conservation prevents the required oscillation into its anti-particle.

2.4 Measuring the angle γ

This section covers the theory that underpins the choice of decay modes studied.

2.4.1 The GLW method

Equation 2.6 showed that to measure γ, quantum mechanical interference between modes that involve $b \to c$ and $b \to u$ quark transitions are required. Decays of the type $B^- \to D^0 X$ are therefore an obvious choice as can be seen in the Feynman diagrams of Fig. 2.3.

The $B^- \to D^0 X$ decay modes are theoretically clean because tree decays dominate. In general it is found that the measurements required are infeasible experimentally because these decays have $b \to u$ transitions, which for the decays in Fig 2.3 are colour suppressed, while the $b \to c$ transitions are colour allowed. This leads to

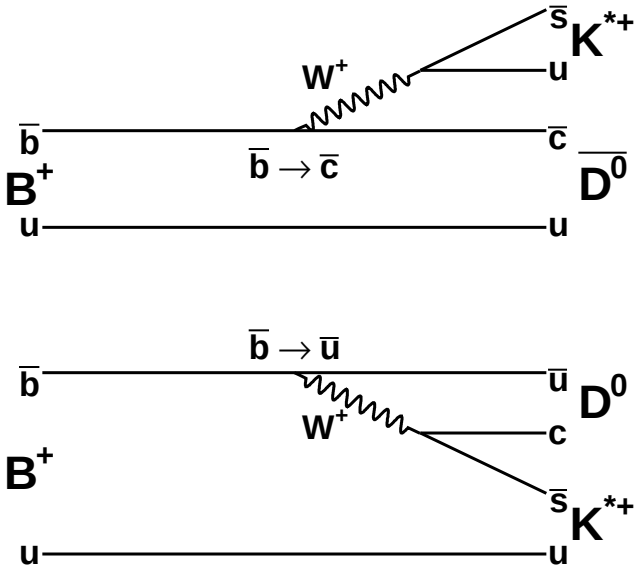

Figure 2.3: The leading order Feynman diagrams for the decay $B^+ \to D^0 K^{*+}$.

large differences in the relative amplitudes and so any interference effects are small. The colour suppression arises from the W being forced to decay into two quarks which have the same colour as the spectator quark while the colour allowed process has no such constraint.

This issue is tackled in the Gronau-London-Wyler [7–10] (GLW) method which uses a subset of this decay type where the measurements can be performed, namely $B^- \to D^0 X_S$. Here the colour allowed $b \to c$ transition is combined with a Cabibbo suppressed V_{us} process, while the colour suppressed $b \to u$ process is combined with a Cabibbo favoured V_{cs} process. This can be seen in the Feynman diagram in Figure 2.3. This means that the two diagrams have comparable amplitudes and so the interference effects should be easier to measure.

The obvious disadvantage is that these decays are very rare, with a total branching ratio on the order of 10^{-5} to 10^{-7} for the modes studied in this thesis. A reconstruction efficiency below 10% for these decays contributes to the problem. This means that for the key CP modes measured in this analysis on the order of 10 signal events are expected to be measured on the data sample of 204 million $B\overline{B}$

events. Indeed the measurement is only possible due to both PEP-II producing, and *BABAR* coping with, luminosities well above those specified in the original design of the experiment.

Several modes give the quark content required by the GLW method including D^0K^-, D^0K^{*-} and $D^{*0}K^-$. This analysis studies decays of the type $B^- \to D^0K^{*-}$ where $K^{*-} \to K^-\pi^0$.

In general we expect an asymmetry in the decay rates of $B^\pm \to f(\bar{f})$ if two amplitudes contribute with different strong and different weak phases. The GLW method creates three independent quantities from three measurable quantities: r_B, δ and γ. The quantity r_B is formed from the ratio of the $b \to u$ amplitude to that of the $b \to c$ amplitude, i.e,

$$r_B = \frac{|A(b \to u)|}{|A(b \to c)|}. \tag{2.7}$$

The value of δ is given by the difference of the strong phase of the two amplitudes and γ is the difference in the weak phase of the amplitudes. The key difference between these two phases is that on applying charge conjugation, the sign of the weak phase reverses while the sign of the strong phase remains unchanged.

The method defines:

$$A(B^- \to D^0K^{*-}) = a, \tag{2.8}$$

$$A(B^- \to \overline{D}^0K^{*-}) = ar_Be^{i\delta}e^{i\gamma}. \tag{2.9}$$

If the D^0 and $\overline{D}^0$ decay to the same final state, which must therefore be a CP eigenstate, quantum interference is seen. It must be assumed that any D^0 $\overline{D^0}$ mixing is negligible in order to attribute any asymmetry seen as being entirely due to the magnitude of γ. This assumption should be valid as the amount of D^0 mixing in the Standard Model is predicted to be negligible [7].

The CP-even and CP-odd D^0 eigenstates can be written as,

$$D^0_\pm = (D^0 \pm \overline{D}^0)/\sqrt{2}, \tag{2.10}$$

where the subscript $+(-)$ refers to a CP-even (CP-odd) eigenstate. A D^0 decaying to K^+K^- or $\pi^+\pi^-$ has CP $= +1$ while decays to $K^0_S\pi^0$, $K^0_S\phi$ or $K^0_S\omega$ have CP$= -1$.

So by combining Equation 2.10 with Equations 2.8 and 2.9 the following holds:

$$\sqrt{2}\mathrm{A}\left(B^- \to D^0_\pm K^{*-}\right) = a \pm a r_B e^{i\delta} e^{i\gamma}. \tag{2.11}$$

Similarly the charge conjugate reaction has the amplitude

$$\sqrt{2}\mathrm{A}\left(B^+ \to D^0_\pm K^{*+}\right) = a \pm a r_B e^{i\delta} e^{-i\gamma}. \tag{2.12}$$

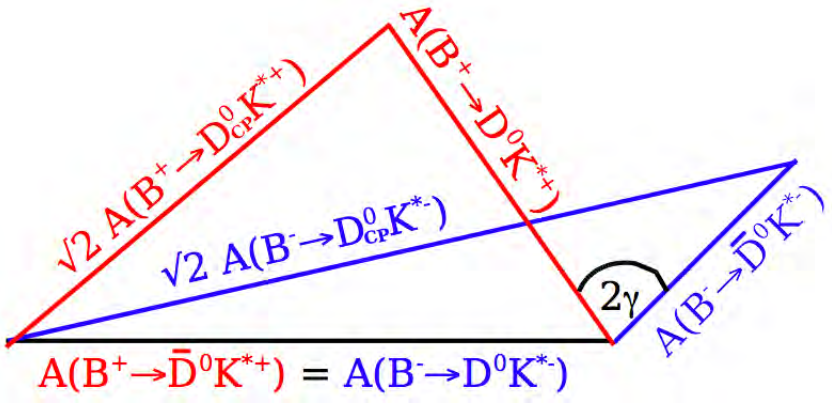

Figure 2.4: These triangles demonstrate how γ can be found from a measurement of six branching fractions. The asymmetry is a result of the sides associated with the $D^0_\pm$ decays being unequal

These relations can be represented geometrically in the complex plane shown in Fig. 2.4.

The amplitudes must now be squared to obtain the rates of these decays. By combining Equations 2.11 and 2.12 we find,

$$\begin{aligned} \left|A\left(B^- \to D^0_\pm K^{*-}\right)\right|^2 \;+\; & \left|A\left(B^+ \to D^0_\pm K^{*+}\right)\right|^2 \\ = \; & a^2\left(1 + r_B^2 \pm 2 r_B \cos\delta\cos\gamma\right), \end{aligned} \tag{2.13}$$

and,

$$\begin{aligned} \left|A\left(B^- \to D^0_\pm K^{*-}\right)\right|^2 \;-\; & \left|A\left(B^+ \to D^0_\pm K^{*+}\right)\right|^2 \\ = \; & \pm 2 a^2 r_B \sin\delta\sin\gamma. \end{aligned} \tag{2.14}$$

Using these equations, four quantities can be built and expressed in terms of the

three unknown parameters, δ, γ and r_B. These are:

$$\mathcal{A}_\pm = \frac{\Gamma\left(B^-\to D^0_\pm K^{*-}\right)-\Gamma\left(B^+\to D^0_\pm K^{*+}\right)}{\Gamma\left(B^-\to D^0_\pm K^{*-}\right)+\Gamma\left(B^+\to D^0_\pm K^{*+}\right)} = \frac{\pm 2r_B \sin\delta\sin\gamma}{1 \pm 2r_B\cos\delta\cos\gamma + r_B^2}; \quad (2.15)$$

$$\mathcal{R}_\pm = \frac{\Gamma\left(B^-\to D^0_\pm K^{*-}\right)+\Gamma\left(B^+\to D^0_\pm K^{*+}\right)}{\Gamma(B^-\to D^0 K^{*-})} = 1 \pm 2r_B\cos\delta\cos\gamma + r_B^2. \quad (2.16)$$

The subscript sign indicates CP-even (+) or CP-odd (−) modes are used. In fact not all of these quantities are independent as we have

$$\mathcal{A}_\pm = \frac{\Gamma\left(B^-\to D^0_\pm K^{*-}\right)-\Gamma\left(B^+\to D^0_\pm K^{*+}\right)}{\Gamma\left(B^-\to D^0_\pm K^{*-}\right)+\Gamma\left(B^+\to D^0_\pm K^{*+}\right)} = \frac{\pm 2r_B \sin\delta\sin\gamma}{\mathcal{R}_\pm}. \quad (2.17)$$

Thus there is an additional constraint,

$$\mathcal{A}_+\mathcal{R}_+ = -\mathcal{A}_-\mathcal{R}_-. \quad (2.18)$$

So effectively there are three independent measurables and three unknowns.

Both the weak (γ) and strong (δ) phases must be non-zero to have a non-zero value for $\mathcal{A}_+$ and $\mathcal{A}_-$. An asymmetry is expected to be observed because it is anticipated that there will be a relative difference in both the strong [11] and the weak phases.

It should also be noted that the value of r_B has been measured to be of the order 0.1 to 0.2 [18]. This means that any CP asymmetry is limited to the order of 10 to 20%.

2.4.2 Resolving the discrete ambiguities

Equations 2.15 and 2.16 show that the sin and cos terms lead to ambiguities in the sign of both the weak phase γ and the strong phase δ.

As well as the ambiguity that results from the addition of π to these angles ($\gamma+\pi$ and $\delta+\pi$) there is the fact that no single measurement can distinguish between γ and δ, i.e we don't know how much interference is due to the strong phase and how much is due to the weak phase. So explicitly the same numerical value of $\mathcal{A}_\pm$ will be given for (γ, δ), (-γ, -δ), (δ, γ), (-δ, -γ), ($\pi+\gamma$, $\pi+\delta$), ($\pi-\gamma$, $\pi-\delta$), ($\pi+\delta$,

$\pi + \gamma)$ and $(\pi - \delta, \pi - \gamma)$.

The ambiguity related to the sign of γ is reduced thanks to indirect constraints on the physical range of γ which have measured it to be in the range $40° < \gamma < 100°$ [18]. To reduce the ambiguity we can take several measurements made with different modes. These modes should share the same weak phase, but the strong phase could differ, therefore helping to remove some of the ambiguities.

2.5 Treatment of the additional strong phase from $B^- \to D^0 K^- \pi^0$ decays

The GLW analyses that make use of $D^0 K^{*-}$ decays suffer from an irreducible background because decays of the type $B^- \to D^0 K^- \pi^0$ have the same final state as the signal mode $B^- \to D^0 K^{*-}$ ($K^{*-} \to K^- \pi^0$). Unfortunately it is not possible to distinguish these background events from signal in the fit strategy. Indeed it is quantum mechanically impossible to separate them on an event by event basis.

Further difficulties arise from the branching ratio of $B^- \to D^0 K^- \pi^0$ being unmeasured to-date. This makes it impossible to predict the amount of this background from this source with certainty. Another difficulty is that these modes interfere with the signal modes which potentially introduces an additional strong phase. This means that the decay amplitudes and hence the measurables $\mathcal{A}_\pm$ and $\mathcal{R}_\pm$ are modified. It is clear that an understanding of the effect of this mode is required.

2.5.1 Modelling the effect of the non-resonant background

The differences between the resonant (K^{*-}) and non-resonant ($K^-\ \pi^0$) decays are that the K^{*-} mass line shape can be modelled by a Breit-Wigner in the resonant case, while in the non-resonant case it will be a broad spectrum. The angular distribution in the resonant case should have a $\cos\theta$ dependence as the K^{*-} is a spin 1 particle [12]. The angle θ is defined as the angle between the momentum vector of the K^- in the rest frame of the K^{*-} and the momentum vector of the K^{*-} in the rest frame of the B^-. The angular dependence of the non-resonant mode, however, should be flat as this is a spin 0 state. An attempt to measure the effect of the non-resonant modes can be made by looking at these variables and taking into account the effect of the possible amplitude interference. Further details are

provided in Chapter 7.

2.6 Status of current results

The decay $B^- \to D^0 K^{*-}$ has been studied previously at *BABAR*. A measurement of the branching fraction [13] was made with $81.9\,\text{fb}^{-1}$ of data reconstructing the D^0 to non-CP final states with the K^{*-} decaying to $K^0_S\pi^-$. A subsequent analysis using $210\,\text{fb}^{-1}$ of data has measured both the branching ratio [14] and the CP asymmetry [15] using D^0 decays to CP and non-CP final states, again reconstructing the decay $K^{*-} \to K^0_S\pi^-$.

Figures 2.5 and 2.6 show the current world averages for the measurement of $\mathcal{A}_\pm$ and $\mathcal{R}_\pm$ respectively for the D^0K^{*-}, D^0 K^- and D^{*0} K^- modes. The results for D^0K^{*-} are also presented in Table 2.1. These figures have been compiled by the HFAG collaboration [17].

Table 2.1: The world averages of $\mathcal{A}_\pm$ and $\mathcal{R}_\pm$. The values for *BABAR* 2005 and Belle 2003 are taken from [15] and [16] respectively. Both of these results use the K^{*-} decaying to K^0_S π^- in contrast to this analysis which reconstructs the K^{*-} decaying to K^- π^0.

Result	$\mathcal{A}_+$	$\mathcal{A}_-$
BABAR 2005	-0.08 ± 0.19± 0.08	-0.26 ± 0.40 ± 0.12
Belle 2003	-0.02 ± 0.33 ± 0.07	0.19 ± 0.50 ± 0.04
Average	-0.06 ± 0.18	-0.08 ± 0.32
Result	$\mathcal{R}_+$	$\mathcal{R}_-$
BABAR 2005	1.96 ± 0.40 ± 0.11	0.65 ± 0.26 ± 0.08
Belle 2003	Unmeasured	Unmeasured
Average	1.96 ± 0.41	0.65 ± 0.27

The UTFit collaboration have calculated γ to be in the range $36^\circ < \gamma < 97^\circ$ (at 95% C.L) [18]. This result is based upon indirect measurements only, these are measurements of quantities other than γ that theoretically constrain the position of the apex of the unitarity triangle and hence the size of γ. The various constraints are shown in Fig. 2.7.

When only the results of direct measurements published to date are used, the resulting constraint is less stringent, but is consistent with the indirect measure, as γ is found to be in the range $36^\circ < \gamma < 103^\circ$ at 95% confidence level. This is shown in Fig. 2.8.

It can be seen from these previous measurements that the statistical error is dominant in all cases. The motivation for this analysis is to exploit additional decay modes in order to further constrain the direct measurement of γ.

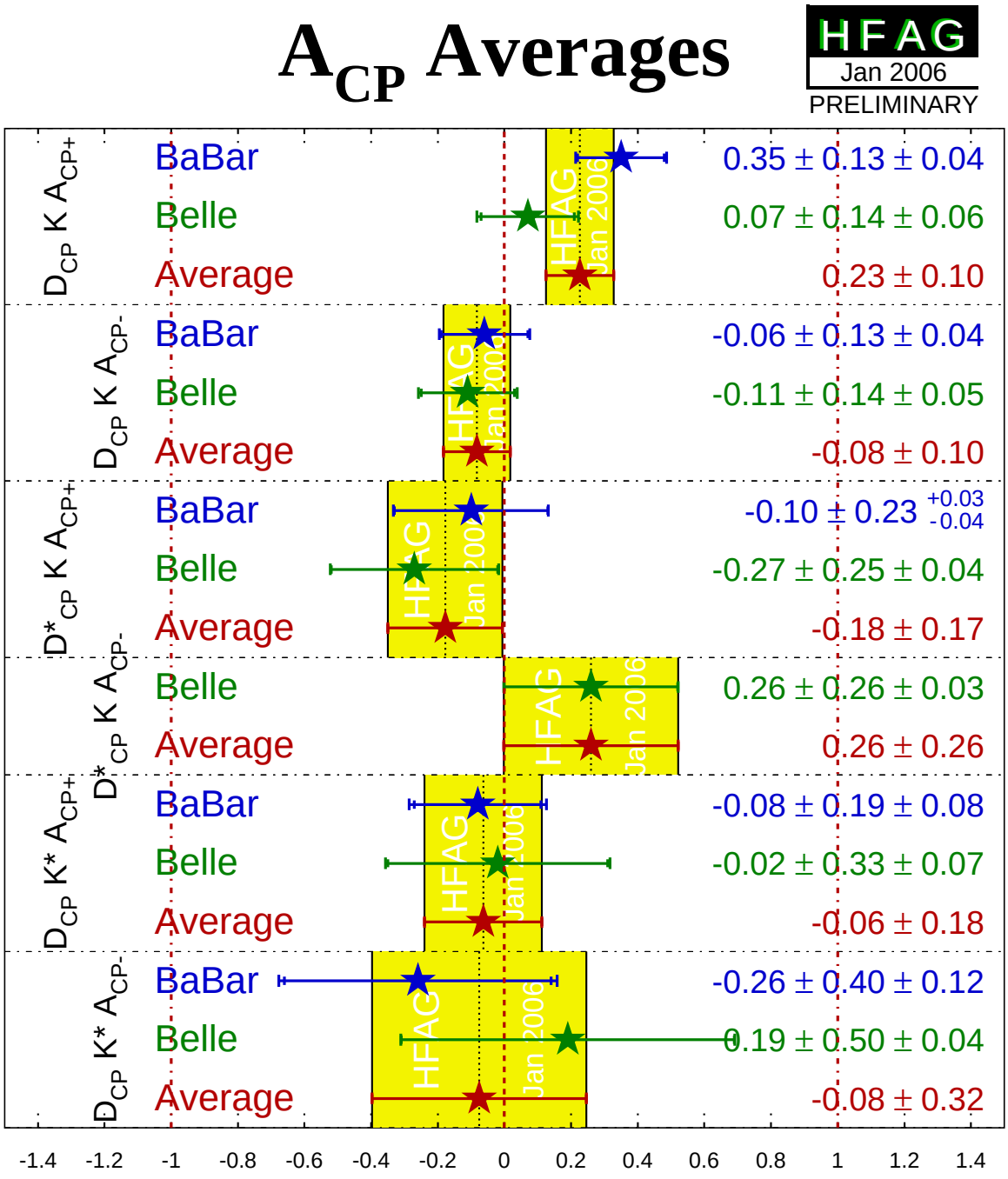

Figure 2.5: Measurements of $\mathcal{A}_{\pm}$ collated by the HFAG collaboration [17].

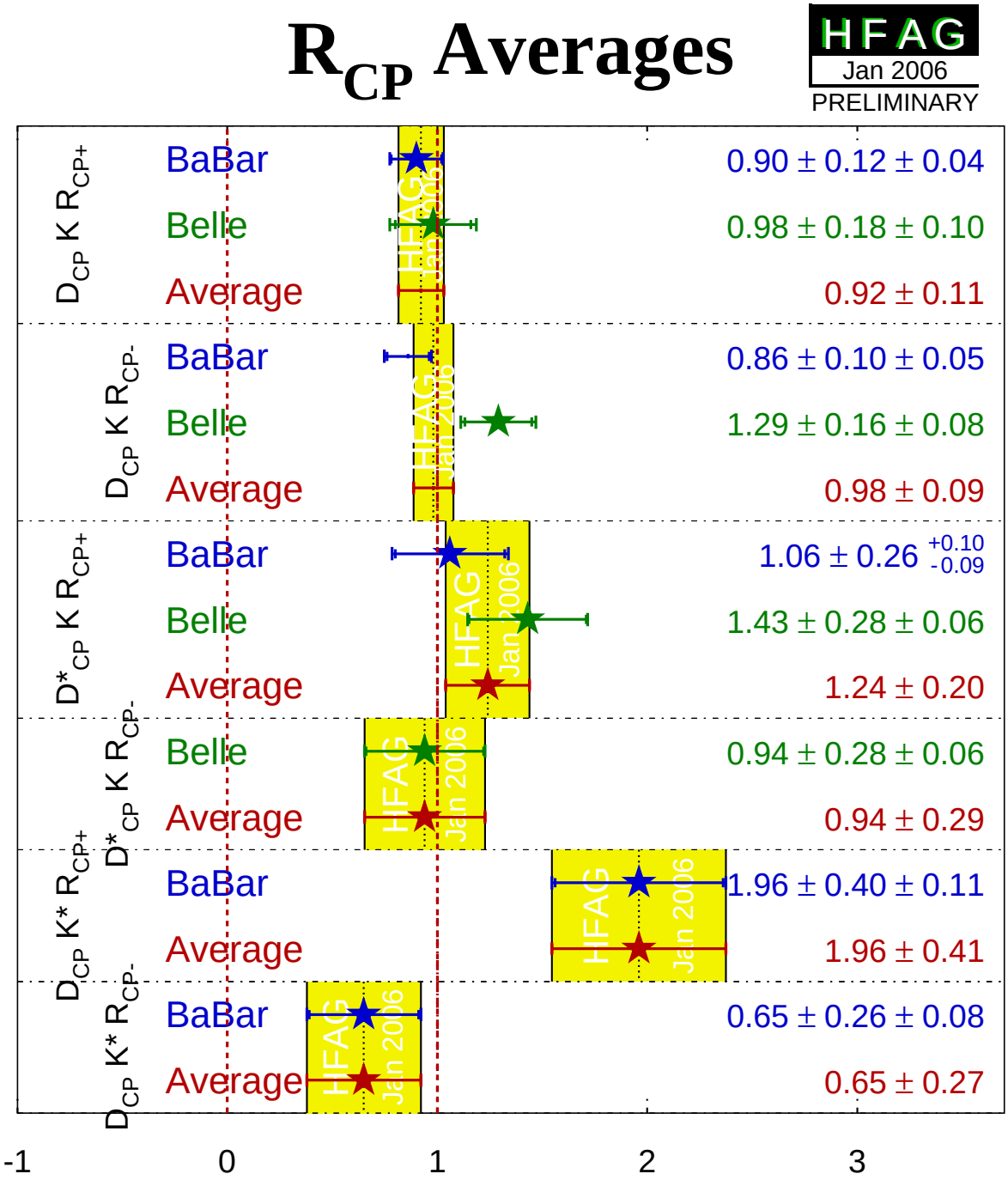

Figure 2.6: Measurements of $\mathcal{R}_{\pm}$ collated by the HFAG collaboration [17].

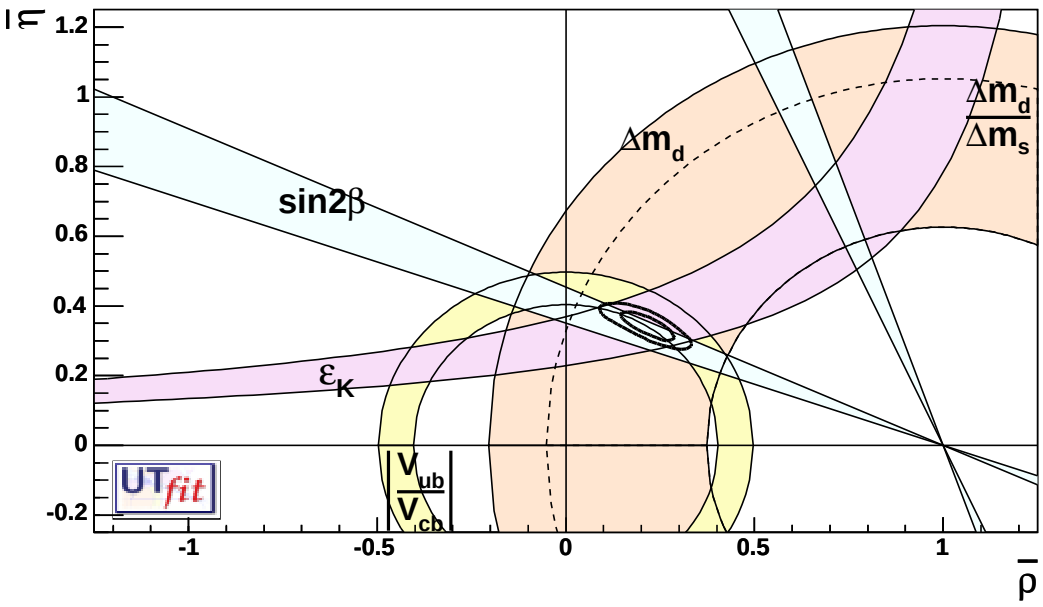

Figure 2.7: An estimate of the position of the vertex of the unitarity triangle. This plot is based solely on indirect constraints and is taken from the UTFit collaboration [19]. An indirect constraint is one which uses theoretical relations and measurements of quantities other than γ in order to estimate the size of γ. The inner line at the apex of the triangle represents 68%C.L. while the outer line represents 95%C.L.

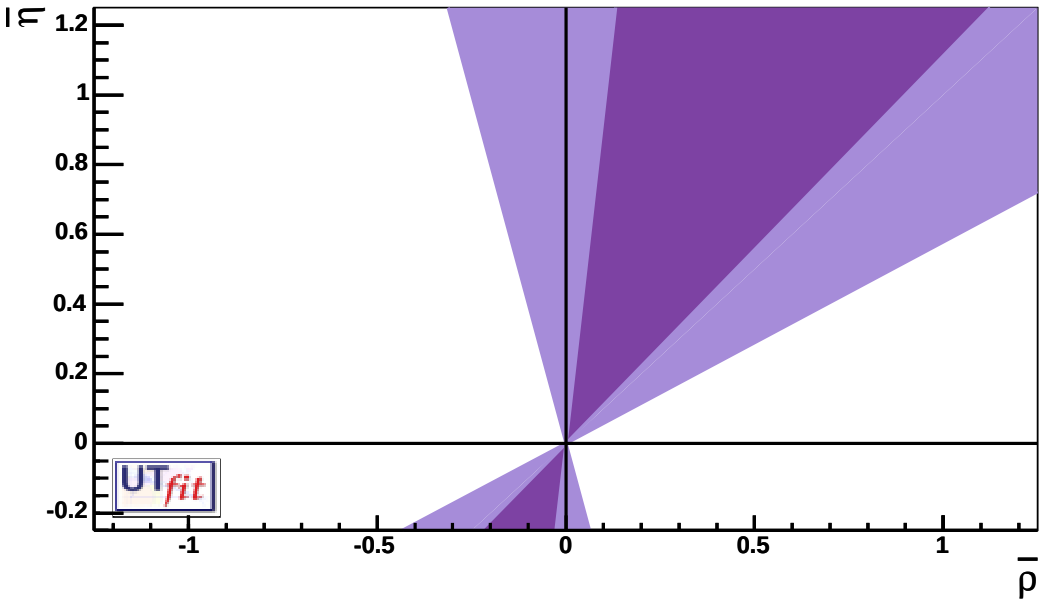

Figure 2.8: An estimate of the position of the vertex of the unitarity triangle. The lightly shaded region is the bound of the 90% confidence level and the darker region is the bound of the 95% confidence level. This plot is based solely on direct constraints and is taken from the UTFit collaboration [18].

Chapter 3

The *BABAR* detector at PEP-II

The PEP-II accelerator [20] is a B-factory, located at the Stanford Linear Accelerator Center in California, which collides bunches of electrons and positrons at the $\Upsilon(4S)$ resonance. The B mesons produced by the decay of the $\Upsilon(4S)$ are detected by the *BABAR* detector [21] which sits at the interaction point (IP) of PEP-II. The primary aim of the *BABAR* programme is to measure CP-violation in the decay of these B mesons.

This chapter describes the basics of the PEP-II accelerator and gives an overview of the sub-detectors that form the *BABAR* detector.

3.1 The PEP-II collider

PEP-II is an electron-positron storage ring supplied by a two-mile long linear accelerator. It collides a beam of 9 GeV electrons and 3.1 GeV positrons in the centre of the *BABAR* detector. The asymmetry in the energy of the beams leads to a boost of the centre-of-mass frame relative to the laboratory frame with $\beta\gamma = 0.56$. This boost increases the average separation between B meson decay vertices, which makes a measurement of this separation and hence the difference in decay time possible. This enables time dependent CP violation to be measured. The analysis presented here, however, does not make a direct use of this boost as the asymmetry measured is not time dependent.

The centre-of-mass energy when running on-peak is 10.58 GeV, the mass of the $\Upsilon(4S)$ resonance, which leads to a high cross-section for the production of $\Upsilon(4S)$ mesons. As the $\Upsilon(4S)$ decays almost exclusively to $b\overline{b}$ quark pairs, copious numbers

of B^+B^- and $B^0\overline{B}^0$ mesons are produced. As well as the high cross section seen for the production of the $\Upsilon(4S)$ at this energy there is also a significant cross-section for $e^+e^- \to q\overline{q}$ decays where q is an up, down, charm or strange type quark. The decays of this type form a source of background that must be studied. The cross-section figures are summarised in Table 4.1.

The design luminosity of PEP-II was $3 \times 10^{33}\,\mathrm{cm}^{-2}\mathrm{s}^{-1}$. However at the time of writing the record peak luminosity is $12.07 \times 10^{33}\,\mathrm{cm}^{-2}\mathrm{s}^{-1}$, achieved on the 16th of August 2006, exceeding the original design by a factor of four. This performance has allowed *BABAR* to record an integrated luminosity of $390.8\,\mathrm{fb}^{-1}$.

3.2 The *BABAR* detector

The *BABAR* detector has been designed with the goal of making accurate study of CP-violating effects in B-mesons possible. To do this the detector requires good tracking of charged particles and measurement of the position of decay vertices. It also requires the ability to measure the energy of photons and to accurately distinguish charged kaons from charged pions. These basic requirements are fulfilled by specialised subsystems.

The *BABAR* detector is shown in cross-section in Fig. 3.1. Charged particle tracks are measured with a multi-layer Silicon Vertex Tracker (SVT) and a surrounding cylindrical wire Drift Chamber (DCH). CsI crystals are used in the Electromagnetic Calorimeter (EMC) to detect electromagnetic showers from electrons and photons. A solenoid provides a magnetic field of 1.5 T, the steel flux return of this magnet is instrumented with resistive plate chambers in order to detect muons and hadronic showers. Charged hadrons are identified by using $\mathrm{d}E/\mathrm{d}x$ measurements from the tracking detectors and by the detector of internally reflected Čerenkov radiation (DIRC). A trigger system consisting of a level-one hardware stage and a level-three software stage is used to select the events of most interest. These subsystems are further described in following subsections.

The centre of the detector is offset from the Interaction Point (IP) by 370 mm in order to optimise the detector acceptance due to the asymmetric beam energies. The beam-line is defined as the $z-$axis, the $y-$axis points upwards and the $x-$axis points horizontally away from the centre of the PEP-II ring.

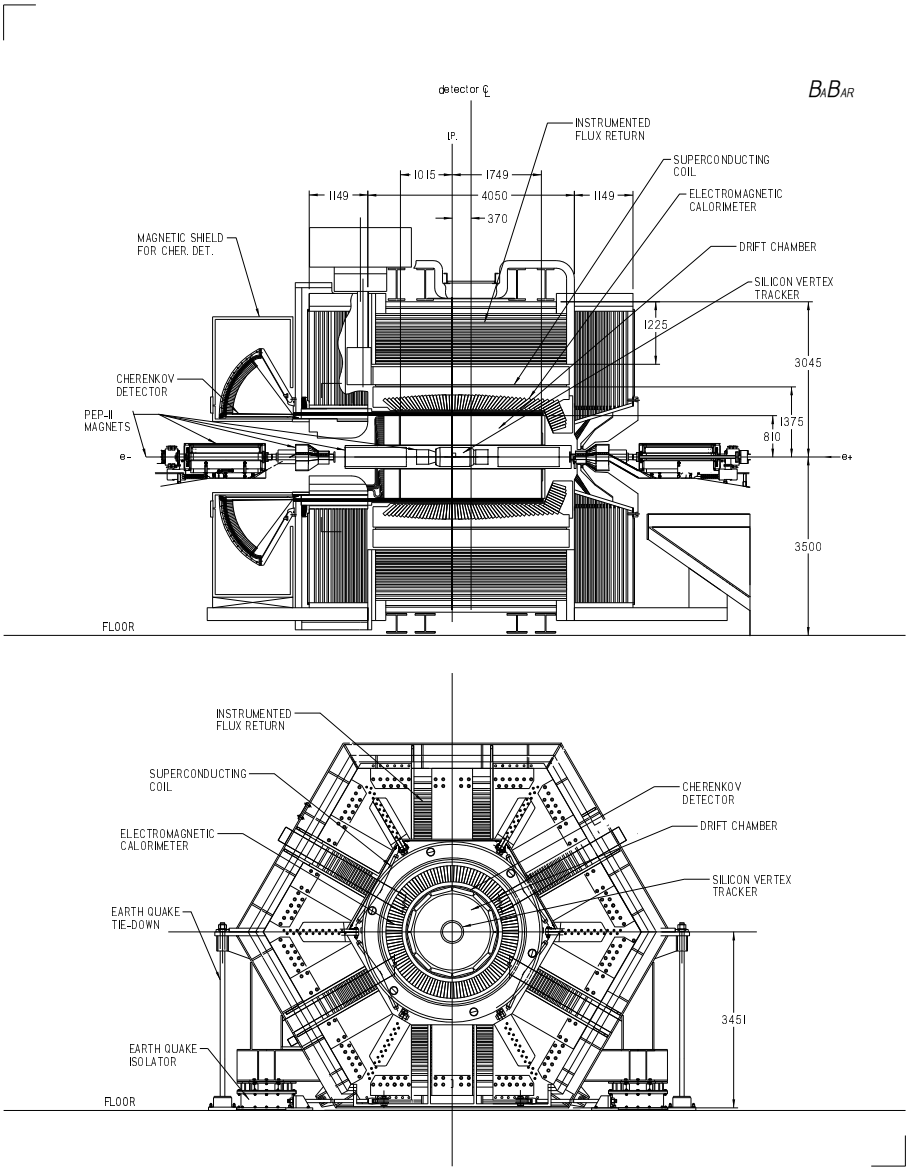

Figure 3.1: Cross-sections of the *BABAR* detector [21].

3.2.1 The silicon vertex tracker (SVT)

Together with the drift chamber, the silicon vertex tracker (SVT) provides the charged particle tracking capabilities of the detector. For particles with transverse momentum (p_t) less than 120 MeV/c it is the only source of tracking information. It also provides energy loss ($\mathrm{d}E/\mathrm{d}x$) information for use in particle identification.

The SVT consists of five layers of double-sided silicon strip detectors. The ar-

rangement of these layers is shown in Fig. 3.2 while Fig. 3.3 is a side view cross-section. The range of polar angle covered is $20° < \theta < 150°$.

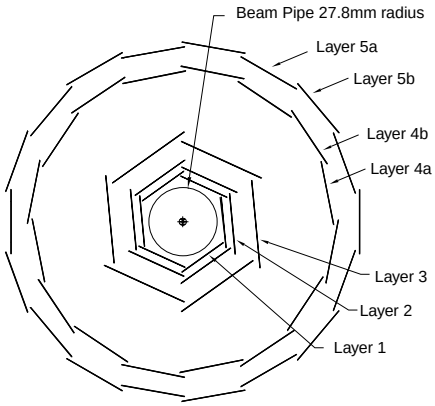

Figure 3.2: The end-on view of the Silicon Vertex Tracker (SVT) [21].

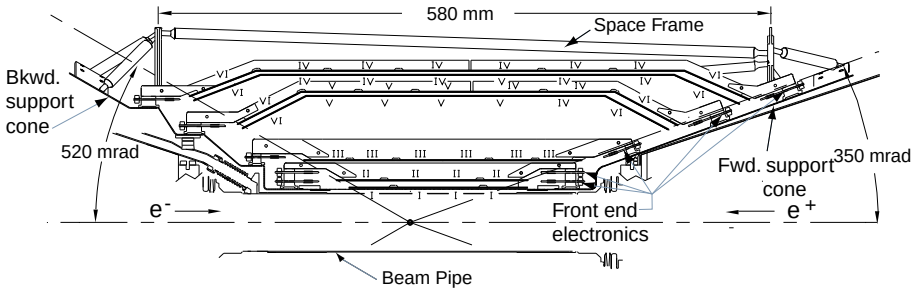

Figure 3.3: A side cross-section of the Silicon Vertex Tracker (SVT) [21].

The primary purpose of the inner three layers is to gain position and angle information for the measurement of vertex positions. The inner layer is therefore mounted 30 mm from the interaction point, just outside of the beampipe's 27.8 mm radius. The primary purpose of the outer two layers is to provide tracking information to allow SVT tracks to be matched with tracks in the drift chamber.

The inner three layers consist of six modules each while the outer two layers contain 16 and 18 modules respectively. The strips on opposite sides of each sensor are aligned orthogonally to each other with ϕ measuring strips parallel to the beam

and z measuring strips transverse to the beam. In the $z-$axis, the SVT has a resolution of 80 μm, while in the $x-y$ plane a resolution of 100 μm is achieved.

The double-sided strips are capable of providing as many as ten dE/dx measurements per track. Figure 3.4 shows the distribution of dE/dx along with expected behaviour for several particle types. The algorithm used (on a minimum of four sensors registering a track) can give a 2σ separation between kaons and pions up to a momentum of 500 MeV/c. This is of particular relevance in this analysis due to the large number of pions and kaons in the final states considered.

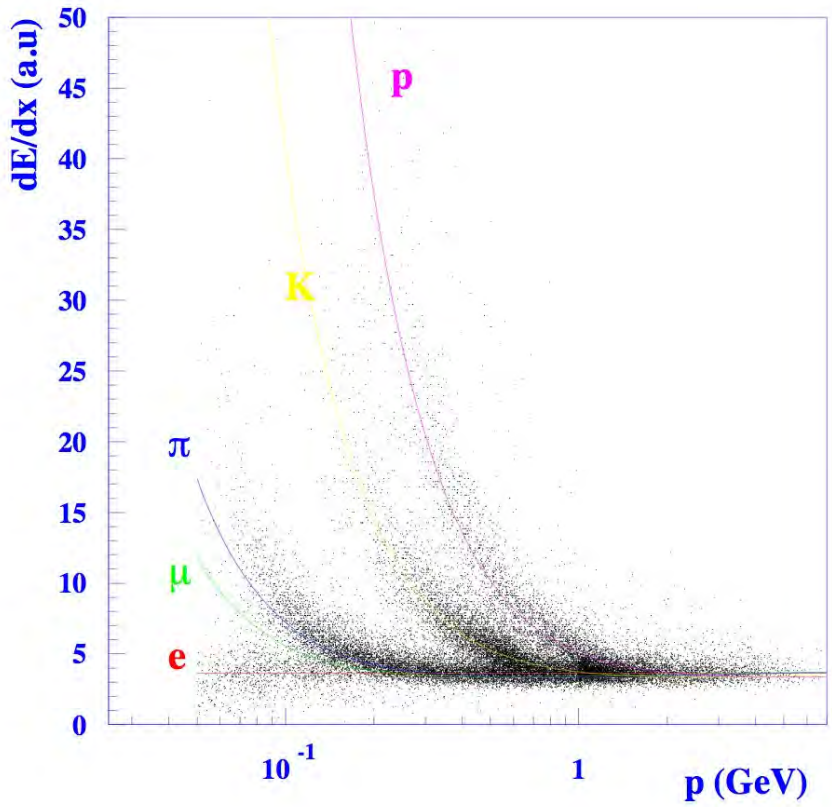

Figure 3.4: A plot of dE/dx versus momentum from the Silicon Vertex Tracker [21].

3.2.2 The drift chamber (DCH)

The drift chamber (DCH) has a similar design goal to the SVT, to measure with high precision the momenta and angles of charged particles. Where the SVT is more precise for vertex measurements, the DCH is more precise for momentum measure-

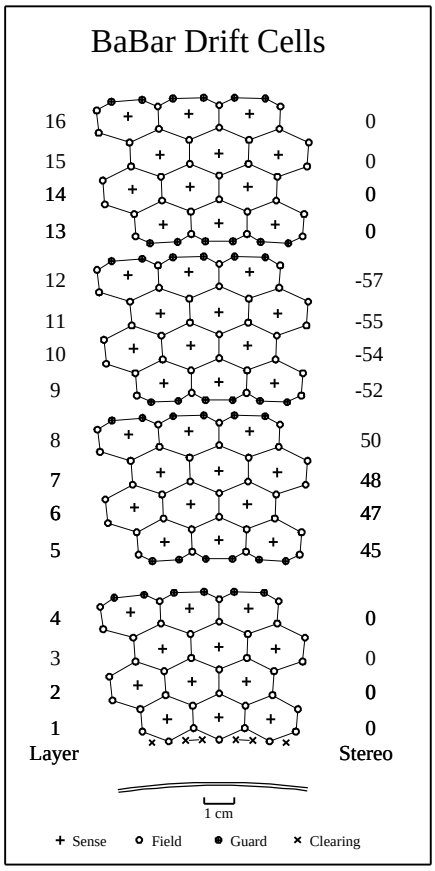

Figure 3.5: The layout of cells within the drift chamber (DCH) [21].

ment. The DCH is three metres long and, as illustrated in Figure 3.5, is composed of 40 layers of approximately hexagonal cells. Each sense wire is surrounded by six field wires giving a total of 28,768 wires. In order to gain longitudinal position information, 24 of the 40 layers have their wires in a stereo arrangement, which means that they are at small angles relative to the $z-$axis. Groups of four layers are arranged into ten super layers that contain equal numbers of cells. To minimise the amount of multiple scattering, low mass wires and a helium based gas are used. The cross-section of the DCH is shown in Figure 3.6.

The DCH also provides another source of $\mathrm{d}E/\mathrm{d}x$ measurements which are used for the separation of kaons from pions. At momenta lower than 700 MeV a separation of 2σ is achieved.

By combining the information from both the silicon vertex tracker and the drift

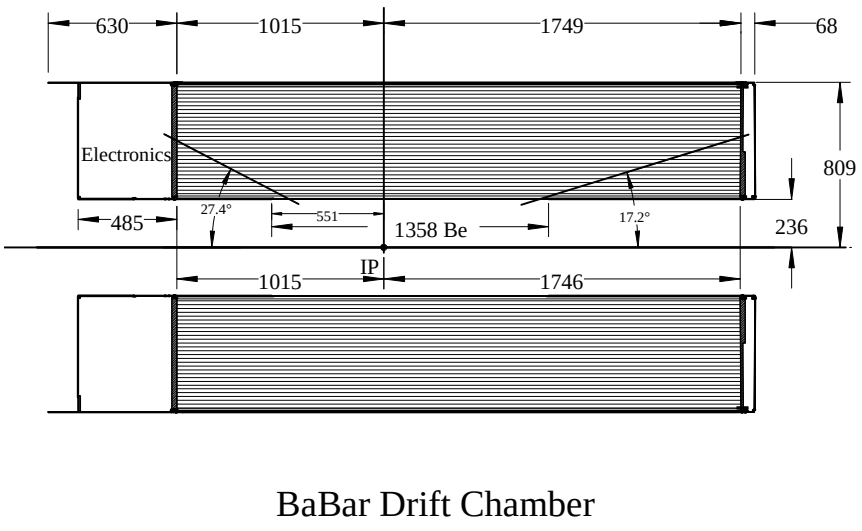

Figure 3.6: Cross-section of the drift chamber [21].

chamber, it is found that the resolution of the transverse momentum is

$$\sigma_{p_t}/p_t \;=\; (0.13)\% p_t + (0.45)\%\ (\,\mathrm{GeV}/c)$$

The first term in this equation arises from measurement errors which are proportional to the momentum of the charged particle. The second term arises from multiple Coulomb scattering effects. The error from this source is essentially constant as around any single sensing wire the track appears straight.

3.2.3 The detector of internally reflected Čerenkov light (DIRC)

The detector of internally reflected Čerenkov radiation (DIRC) is optimised to provide information for the separation of pions and kaons with a momentum from around 500 MeV/c to the kinematic limit of 4.5 GeV/c.

The DIRC (Figure 3.7) consists of 4.9 m bars of fused silica that lead to a standoff box in the backward end of the detector, filled with purified water. A Čerenkov photon produced when a charged particle traverses the bar is internally reflected within the bar until it reaches the instrumented end. It emerges into the standoff box and propagates through water until being detected by a photomultiplier tube

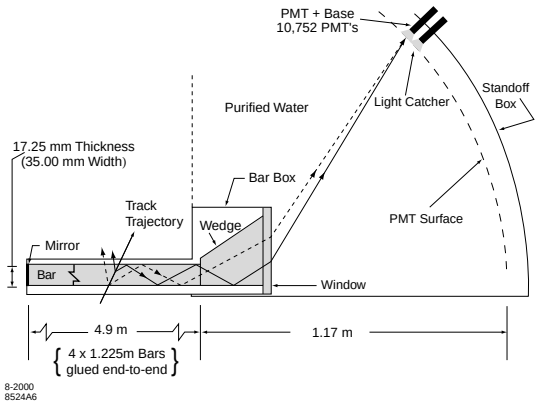

Figure 3.7: Cross-section of the Detector of Internally Reflected Čerenkov light (DIRC) [21].

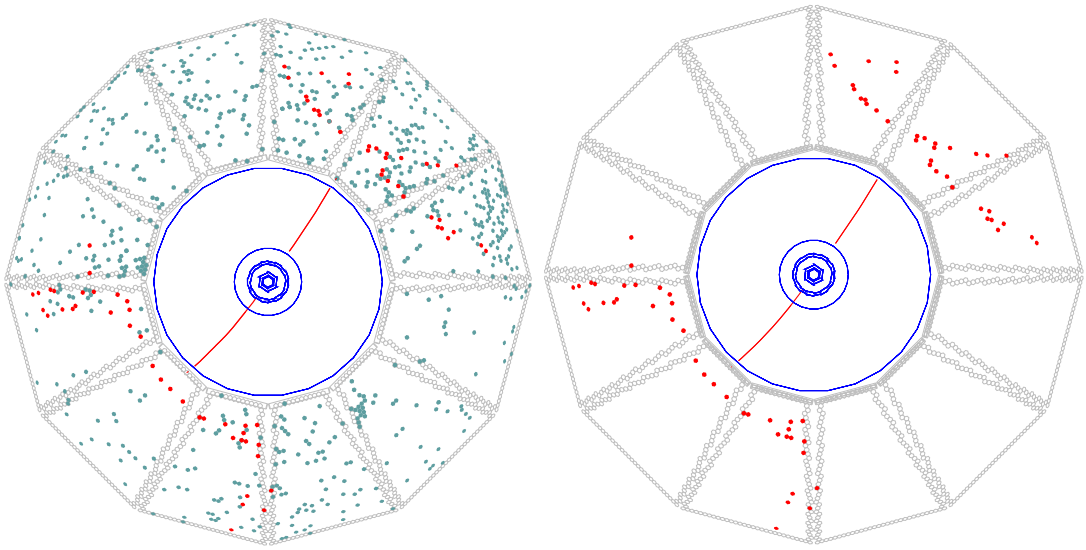

Figure 3.8: An example event in the Detector of Internally Reflected Čerenkov light (DIRC) [21]. The left-hand image shows the distribution of photons from signal (red) and background (green). The image on the right-hand side shows just those photons identified as signal events. This makes it easier to see that a signal event will form two semi-circles, one of which is mirrored because the photons will have been reflected off of the mirror at the front end of the detector.

(PMT). Purified water is used because it has a refractive index close to that of the silica bars, this reduces any internal reflection at the interface of the bars and the water. The cone of Čerenkov light expands while preserving the Čerenkov angle as it passes through the water and strikes the array of photomultipliers. Around 80% of the light successfully traverses the bars and the purified water to make it to the PMTs. Figure 3.8 illustrates the distribution of photons within the DIRC for an

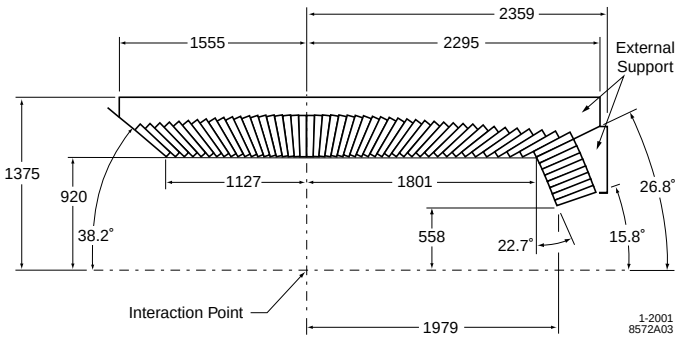

Figure 3.9: Cross-section of the Electromagnetic Calorimeter (EMC) [21].

example event.

Only the backward end of the detector is instrumented. A mirror is used to reflect photons that travel towards the forward end of the bars back to the instrumented end. Due to the lack of a backward calorimeter, this end was instrumented to minimise interference with other subsystems.

3.2.4 Particle Identification (PID)

Together the SVT, DCH and DIRC are the inputs to the *BABAR* particle identification (PID) algorithms. This analysis uses likelihood based selectors to select both charged kaons and charged pions. For each of these subdetectors the probability that a charged track is a kaon is calculated. Each probability is then multiplied together to form an overall probability. For track momenta below 700 MeV, $\mathrm{d}E/\mathrm{d}x$ information from the SVT and DCH is used with the DCH providing the more accurate measure. For momenta above 600 MeV the DIRC is used. This means that for high energy tracks the DIRC is the only source of PID.

PID algorithms are also used to identify electrons and muons, however this analysis does not make use of these tools. Any track which is not identified as a kaon (or an electron or muon) is assumed to be a pion.

This analysis relies on PID to separate kaons from pions. PID is used to select the kaon that is produced by the decay of the K^{*-}. PID is also used in the selection of the daughter products of the decay of the ω, ϕ and the D^0.

3.2.5 The electromagnetic calorimeter (EMC)

The electromagnetic calorimeter (EMC), which is shown in cross-section in Figure 3.9, consists of a barrel and a forward end-cap containing a total of 6580 Thallium (0.1%) doped Caesium Iodide (CsI) crystals. It is capable of detecting electromagnetic showers that range in energy from 20 MeV to 4 GeV. The 20 MeV limit is determined by beam and event backgrounds and the amount of material in front of the calorimeter.

The energy resolution of the EMC is

$$\frac{\sigma_E}{E} = \frac{(2.3 \pm 0.3)\%}{\sqrt[4]{E(\,\mathrm{GeV})}} + (1.9 \pm 0.1)\%$$

while the angular resolution is found to be

$$\sigma_\theta = \sigma_\phi = \frac{(3.9 \pm 0.1)\,\mathrm{mrad}}{\sqrt{\mathrm{E}(\,\mathrm{GeV})}} + (0.0 \pm 0.04)\,\mathrm{mrad}. \tag{3.1}$$

As the single most expensive piece of the *BABAR* detector, every effort was made to limit its cost. This led to the decision not to have a backward end-cap calorimeter. Due to the boost provided by the asymmetric beam energies, this has little effect on the physics sensitivity of the experiment.

In this analysis the EMC plays an important role as each decay mode under study contains a neutral pion from the K^{*-}. The better the energy resolution of the detector the fewer fake pions or unreconstructed pions there will be. The angular resolution is important for matching two photon candidates back to a common vertex to form a π^0 candidate.

3.2.6 The instrumented flux return (IFR)

Designed to detect muons and neutral hadrons (particularly K_L^0), the instrumented flux return (IFR) consists of the layers of steel of the magnet's flux return, instrumented with resistive plate chambers (RPCs) between the gaps in these layers. Figure 3.10 shows that there are 19 RPC layers in the barrel, and 18 in the forward end-cap.

The basic principles of the operation of the RPCs are that they detect streamers from ionising particles using capacitive readout strips. The advantages of using

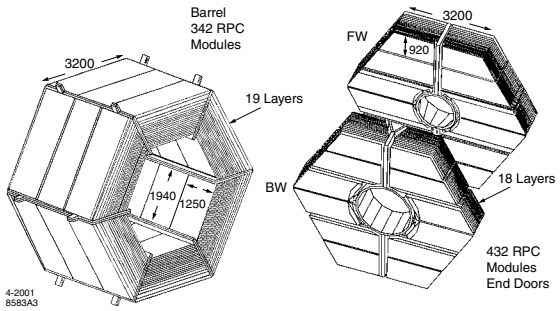

Figure 3.10: Cross-section of the Instrumented Flux Return (IFR) [21].

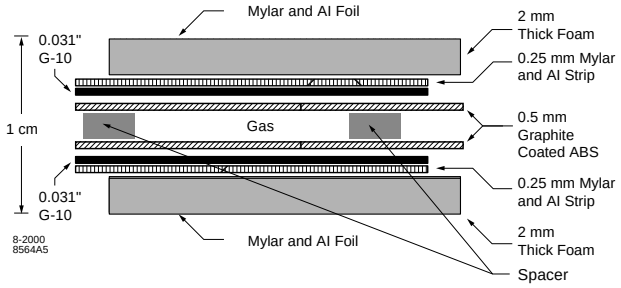

Figure 3.11: Cross-section of a Resistive Plate Chamber (RPC). These RPCs Instrument the Solenoid of the detector, allowing it to be used for muon detection [21].

the RPCs is that they are cheap, simple to produce and can cover various shapes allowing for a minimal amount of dead-space within the detector. An additional benefit is that large signals and a fast response time allow for simple electronics to be used to read out the signals. The RPCs give a time resolution of a few ns and a spatial resolution of a few mm dependent upon the segmentation of the read out for a particular area of the detector. The cross-section of an RPC is illustrated in Figure 3.11.

The IFR does not play a crucial role in this analysis.

3.2.7 The trigger system

The trigger system is required to reject as many background events as possible while efficiently preserving the events of interest. This has been achieved with a two-level design. Each level is required to decide on the acceptance or rejection of an event within the limited time available in order to prevent significant loss of data due to dead-time.

The design requirement was that $b\overline{b}$ events should have a trigger efficiency, after angular cuts to account for events lost down the beam-pipe, of 99%, continuum events 95% and tau events 90-95%. The trigger should also contribute less than 1% to the dead-time.

The level-one trigger uses information from the DCH, EMC and IFR to reduce the trigger output to less than 2 kHz. This trigger is hardware based and has just 12.8 μs to process the information passed from the subsystems and trigger if the event has a signature of interest.

BABAR does not currently have a level-two trigger, but it has been designed with the necessary flexibility in the software to allow one to be included if the luminosity increases to an extent that the level-one trigger cannot stay within the design constraints required by level-three.

The software based level-three trigger takes the output from level-one and further reduces it to a maximum of 120 Hz. The software runs on a farm of dedicated machines. This part of the trigger has an average processing time of 8.5 ms per event for an input of 2.7 kHz. This is well above the design requirement of 2 kHz.

The good performance of the trigger means that the impact upon this analysis is small.

Chapter 4

Preselection of $B^{\pm}$ events

This chapter discusses the preselection of events used in the analysis. The preselection is applied to both the on-peak data and simulated events. It is designed to remove as much background as possible while efficiently leaving signal events. A preselection is a common element within a *BABAR* analysis, it is designed to reduce the amount of processing time required to run the full analysis code on the data samples used. Without a preselection, the optimisation of the cuts in the selection chapter would take a lot longer without achieving an improvement in the final result.

Very few selection criteria (cuts) are applied at this stage and those which are applied are very loose to ensure a high signal efficiency.

4.1 Data and simulated event samples

The data sets used in this analysis are summarised in table 4.1. The analysis is based upon a $185.8\,\mathrm{fb}^{-1}$ sample of data taken at the $\Upsilon(4S)$ resonance at $10.58\,\mathrm{GeV}$. This equates to roughly 204 million $B\overline{B}$ pairs and was recorded from 1999-2004. The data is referred to as on-peak because the centre-of-mass energy is on the peak of the mass resonance giving the largest $\Upsilon(4S)$ production cross-section possible. The analysis has also used an off-peak sample of $21\,\mathrm{fb}^{-1}$ recorded at a centre-of-mass energy $40\,\mathrm{MeV}$ below the mass of the $\Upsilon(4S)$. This latter data set consists of $e^+e^- \to q\overline{q}$ continuum events where the intermediate state $(q\bar{q})$ is composed of up, down, charm or strange type quarks. Due to kinematic constraints, no bottom type quarks can be produced. This sample is used to verify the shapes of distributions within this continuum background.

Table 4.1: Monte Carlo samples used in this analysis, with their equivalent luminosities. A branching ratio of 6.3 $\times 10^{-4}$ was used for the decay $B^- \to D^0 K^{*-}$. This is taken from the previous *BABAR* paper [13] which made a more accurate measurement than the current PDG [12] value. The top section of the table details signal Monte Carlo while the bottom section describes generic Monte Carlo.

Sample	Branching ratio / Cross-section	Events generated	Luminosity (fb^{-1})
$B^- \to D^0 K^{*-}$	6.3×10^{-6}		
$D^0 \to K^- \pi^+$	8.0×10^{-6}	42000	5.2×10^3
$D^0 \to K^- \pi^+ \pi^0$	2.7×10^{-5}	36000	1.3×10^3
$D^0 \to K^- \pi^+ \pi^- \pi^+$	1.6×10^{-5}	31000	2.0×10^3
$D^0 \to K^+ K^-$	8.2×10^{-7}	41000	4.2×10^4
$D^0 \to \pi^+ \pi^-$	2.9×10^{-7}	45000	1.3×10^5
$D^0 \to K^0_S \pi^0$	5.5×10^{-6}	40000	7.4×10^3
$D^0 \to K^0_S \phi$	4.5×10^{-7}	30500	6.9×10^4
$D^0 \to K^0_S \omega$	1.8×10^{-6}	21000	1.8×10^4
uds	2.09 nb	4.39×10^8	210
$c\overline{c}$	1.30 nb	2.73×10^8	210
Generic $B^0\overline{B}^0$	0.55 nb	2.52×10^8	415
Generic B^+B^-	0.55 nb	2.28×10^8	458

Several samples of simulated (Monte Carlo) events have been used. These consist of generic and signal Monte Carlo. The generic Monte Carlo includes B^+B^- and $B^0\overline{B}^0$ samples as well as $u\overline{u}$, $d\overline{d}$, $s\overline{s}$ (called uds) and $c\overline{c}$ samples. The branching ratios used are those compiled by the Particle Data Group (PDG), who publish the Review of Particle Physics [12], or from the most accurate measurements to date where the error on the measurement is less than that given by the PDG. The PDG is also used when an invariant mass of a particle is needed, including where a mass constraint has been applied. The Monte Carlo for signal is generated with one of the produced Bs forced to decay to a selected mode (i.e. one of the eight modes studied by this analysis) while the other B decays with the same composition as generic Monte Carlo.

4.2 Preselection criteria

The reconstruction of B candidates is done by taking the detected final state particles and working backwards chronologically through the time-line of the decay, reconstructing intermediate resonances, until the initial state is found. The selec-

tion and reconstruction of the composite particles is discussed in the same order below by starting with the description of the selection criteria applied to the final state particles and working up the decay chain.

This section describes the preselection only. All cuts are subsequently tightened following the study and optimisation detailed in Section 5.2. From Table 4.1 it is clear that the following particles must be reconstructed in this analysis B^-, D^0, ϕ, ω, kaons and pions. This chapter shows data versus Monte Carlo comparison of the reconstructed masses of the particles below.

The preselection results in eight sets of data, one for each mode, which is of a manageable size to continue the analysis. Some events may fall into two or more of these data sets, this is looked at in Section 5.5 which covers the issue of cross-feed.

4.2.1 Charged particle tracks

BABAR uses several criteria based upon the two tracking subsystems, the silicon vertex tracker and the drift chamber, to select tracks in the data. This analysis makes use of two sets of criteria which yield different quality tracks. The cuts imposed are designed to reduce the amount of background coming from beam-gas interactions and cosmic rays. The following sets of criteria are standard *BABAR* definitions [22].

Loose tracks

Loose tracks are those tracks that have passed the following cuts:

- Momentum less than $10\,\mathrm{GeV}/c$ (removing tracks incompatible with beam energies);
- A maximum distance of closest approach to the interaction point (DOCA) of $\pm 1.5\,\mathrm{cm}$ in the $x-y$ plane and $\pm 10\,\mathrm{cm}$ in the $z-$axis parallel to the beampipe (removing tracks that are likely to have come from a background event).

Tight tracks

A set of higher quality candidate tracks consist of tracks that have passed the same cuts as the loose tracks with further cuts applied:

- Transverse momentum $\geq 0.1\,\mathrm{GeV}/c$ (removes tracks that fail to exit the silicon vertex tracker);
- Number of hits within the drift chamber must be ≥ 12.

4.2.2 Photon candidates

Photon candidates are defined as clusters within the electromagnetic calorimeter that are not matched with a track. The energy of the cluster must be greater than 30 MeV to remove photons from beam backgrounds. To reduce the number of clusters due to hadronic showers a standard *BABAR* cut of 0.8 is applied to the lateral moment [21]. The lateral moment makes use of the fact that a hadronic shower is likely to deposit its energy in a larger number of crystals than an electromagnetic shower however. The lateral moment uses the energy information associated with each crystal in a cluster to decide the likely origin of the shower.

4.2.3 K_S^0 reconstruction

K_S^0 candidates are reconstructed through the decay $K_S^0 \to \pi^+\pi^-$. The decay $K_S^0 \to \pi^0\pi^0$ is not used due to the low reconstruction efficiency of neutral pions combined with a 50% smaller branching ratio. Oppositely charged loose tracks (Section 4.2.1) are used as pion candidates. A mass cut of $\pm 0.025\,\mathrm{GeV}/c^2$ around a central value of $0.498\,\mathrm{GeV}/c^2$ is also applied to the resulting candidate. This cut is very loose as can be seen in the plot of the mass distribution of the K_S^0 candidates presented in Fig. 4.1(a). The tracks are then fitted to a common vertex with the K_S^0 mass constrained to its nominal value. A fit to a common vertex is used when we want to assume that tracks will have originated from the same point in space. A mass constraint can be applied since the intrinsic width of the reconstructed particle is smaller than the mass resolution. Reasonable agreement is seen between the data and the simulated events.

4.2.4 π^0 reconstruction

The π^0 candidates are constructed from simple four-vector addition of a pair of photon candidates (Section 4.2.2). The π^0 candidate formed is required to have an invariant mass in the range $115 < m_{\gamma\gamma} < 150\,\mathrm{MeV}/c^2$ and an energy greater than

200 MeV. Figure 4.1(b) shows reasonable agreement between the on-peak data and simulated events for the two-photon invariant mass. This figure also shows how loose the applied mass cut is.

4.2.5 ϕ reconstruction

The ϕ candidates are reconstructed through their decay to K^+K^-. All combinations of oppositely charged particle tracks are combined with the condition that at least one of the tracks has passed the tight track (Section 4.2.1) cuts. Four-vector addition is used to combine the tracks, with the assumption that the mass of each daughter particle is that of a kaon. A cut of $\pm 30\,\mathrm{MeV}/c^2$ around a central value of $1.019\,\mathrm{GeV}/c^2$ is applied to the invariant mass of the ϕ candidate. Figure 4.1(c) shows the K^+ K^- mass distribution. As well as the reasonable agreement between data and simulated events it can be seen that there is a small peak sitting on top of a large background.

4.2.6 ω reconstruction

The ω is reconstructed using the $\pi^+\pi^-\pi^0$ mode. Two oppositely charged particle tracks from the loose tracks list (Section 4.2.1) are combined with a π^0 candidate (Section 4.2.4). The kinematics of the ω allow a mass constraint to be applied. Figure 4.1(d) shows the mass distribution of the ω candidates. Again good agreement but large background levels are seen.

4.2.7 D^0 reconstruction

The D^0 candidates for the non-CP, CP-even and the CP-odd modes share a very similar set of cuts. In all modes (except the $K^0_S\pi^0$) the D^0 candidates are selected with an invariant mass within 70(90) MeV/c^2 of their nominal values. The tracks are fitted to a common vertex applying a mass constraint. The centre-of-mass momentum of the D^0 is required to be greater than 1.3 GeV/c.

As discussed in Section 2.4.1 the D^0 is reconstructed decaying to three possible CP eigenstates. The non-CP D^0 candidates are reconstructed through their decays to $K^-\pi^+$, $K^-\pi^+\pi^0$ and $K^-\pi^+\pi^-\pi^+$. CP-even D^0 decays are reconstructed using the K^+K^- and $\pi^+\pi^-$ final states. CP-odd D^0 decays are reconstructed using the final states $K^0_S\omega$, $K^0_S\pi^0$ and $K^0_S\phi$.

In all cases loose tracks (Section 4.2.1) are used as both charged pion and charged kaon candidates. The π^0 candidates are reconstructed as defined in Section 4.2.4 for both the $K^-\pi^+\pi^0$ and $K^0_S\pi^0$ modes. K^0_S candidates are created as described in Section 4.2.3, while ϕ and ω candidates are selected as described in Sections 4.2.5 and 4.2.6 respectively. Figure 4.1(e) shows the mass of the D^0 candidates.

4.2.8 K^{*-} reconstruction

K^{*-} candidates are reconstructed through the decay $K^{*-} \to K^-\pi^0$. Loose tracks (Section 4.2.1) are used as charged kaon candidates and π^0 candidates are reconstructed as defined in Section 4.2.4.

The K^{*-} candidates are reconstructed by fitting the origin of the π^0 and the track to a common vertex. The invariant mass of the K^{*-} is required to be within $125\,\mathrm{MeV}/c^2$ of the PDG review [12] value of $0.892\,\mathrm{GeV}/c^2$. Figure 4.1(f) shows the K^{*-} candidates' mass distribution.

4.2.9 B^- reconstruction

Before selecting B^- candidates two variables are defined that are used to create a signal region. These variables are ΔE and m_{ES} where

$$\Delta E = E^* - E^*_{\mathrm{beam}}, \tag{4.1}$$

and

$$m_{\mathrm{ES}} = \sqrt{E^{*2}_{\mathrm{beam}} - p^{*2}}. \tag{4.2}$$

E^*_{beam} is the energy of the beam and p^* is the momentum of the B^- candidate in the centre-of-mass frame of the $\Upsilon(4S)$. For a signal event ΔE will be close to zero and m_{ES} will be close to the mass of the B^-. Plots of these quantities are shown in Figure 4.1(h) and (i).

B^- candidates are reconstructed from four-vector addition of the D^0 and K^{*-} candidates described in Sections 4.2.7 and 4.2.8. The B^- candidates are required to satisfy $\mid \Delta E \mid < 200\,\mathrm{MeV}$ and $5.20 < m_{\mathrm{ES}} < 5.30\,\mathrm{GeV}/c^2$. Finally a cut on the reconstructed mass of the B is applied to select event in the region $4.5 < m_{D^0K^{*-}} < 5.5\,\mathrm{GeV}/c^2$. Figure 4.1(g) shows the B^- mass distribution.

4.2.10 Data, Monte Carlo event comparison

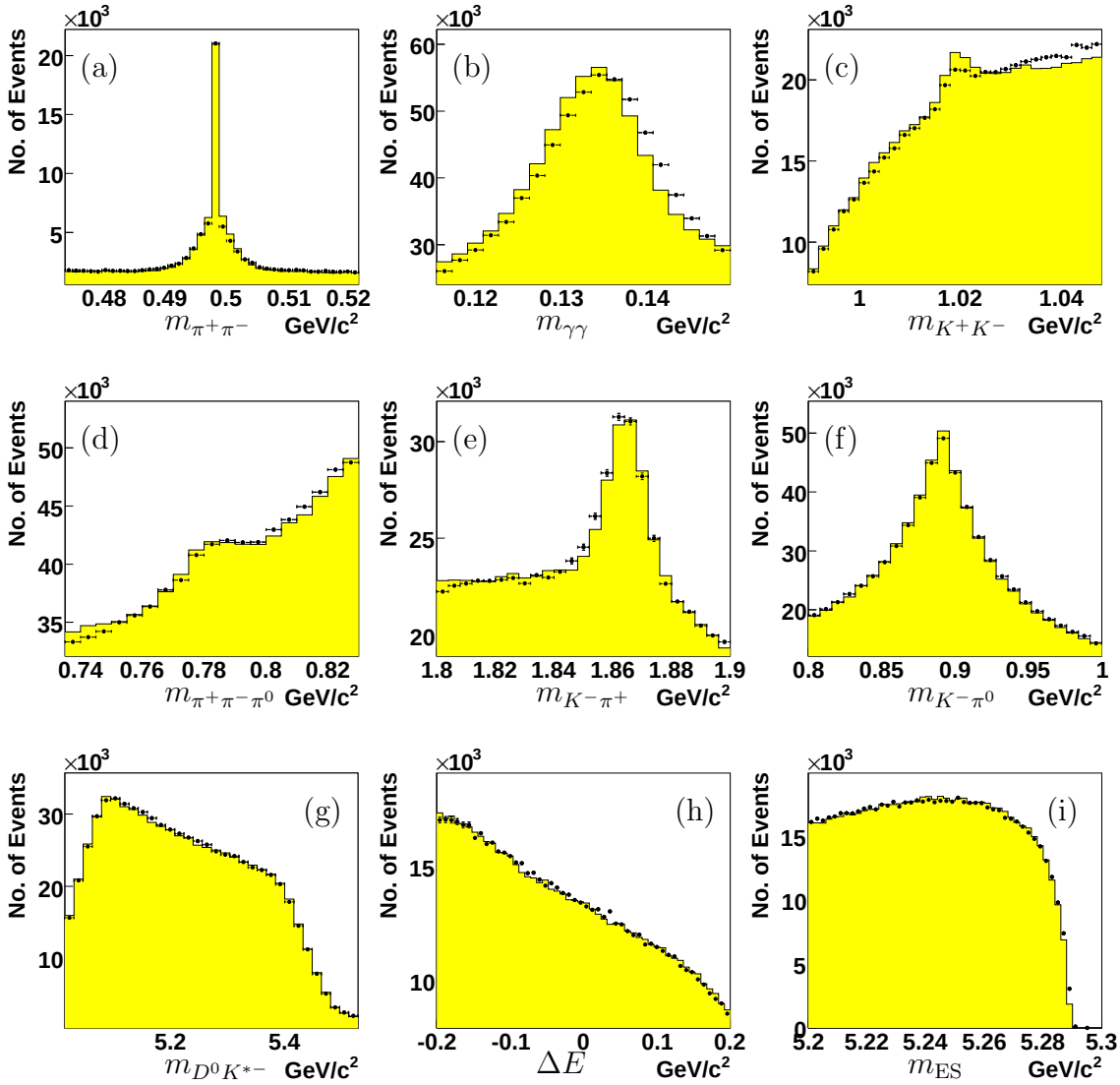

Figure 4.1: Comparison between data and Monte Carlo for variables of $B^- \to D^0 K^{*-}$. The plots are displayed normalised to unit area because at this stage the standard efficiency corrections have not been applied to the simulated events, and it allows easier comparison of the shapes. All preselection cuts are applied with the exception of the cut applied to the distribution displayed. Where multiple candidates exist within the event, a selection criterion detailed in section 5.3 is used. The distributions presented are the reconstructed masses of (a) K^0_S, (b) π^0, (c) ϕ, (d) ω, (e) D^0, (f) K^{*-} and (g) B^-. (h) ΔE and (i) $m_{\rm ES}$ are also shown, although at this stage they show no evidence of a signal. The histogrammes are simulated events, while the dots are data.

Figure 4.1 shows invariant mass distributions for the reconstructed candidates

detailed in the proceeding Sections. The Monte Carlo samples are created from the data sets given in Table 4.1, weighted to give the correct composition. It is important to realise that other than the very loose preselection cuts, no other cuts are applied at this stage. This means that there are still large numbers of background events present which explains the large backgrounds seen in the mass distributions.

The plots show that the reconstruction chain has been successful and that the shapes of the data and simulated event distributions are comparable.

4.3 Effect of the preselection

After applying the preselection which is summarised in Table 4.2 eight sets of data, one for each mode, are created. From the several petabytes of the *BABAR* event database the sample is reduced to a total size of 500 Gb. The selection efficiencies (ϵ) achieved by this preselection are summarised in Table 4.3 and differ by mode with a range of $4\% < \epsilon < 22\%$ on signal events, $1 \times 10^{-2}\% < \epsilon < 8 \times 10^{-5}\%$ on $B\overline{B}$ events and $1 \times 10^{-2}\% < \epsilon < 1 \times 10^{-3}\%$ on continuum background events.

Table 4.2: A summary of the preselection cuts used.

Cut	Value
Charged track "Loose"	
Momentum (GeV/c)	< 10
DOCA $x - y$ (cm)	± 1.5
DOCA z (cm)	± 10
Charged track "Tight"	
DCH hits	≥ 12
Transverse Momentum (GeV/c)	> 0.1
Photon cluster energy (MeV)	> 30
Lateral Moment	< 0.8
K^0_S $m_{\pi\pi}$ (GeV/c^2)	[0.473, 0.523]
π^0 $m_{\gamma\gamma}$ (GeV/c^2)	[115, 150]
ϕm_{KK} (GeV/c^2)	[0.989, 1.049]
D^0 $m_{K^0_S\pi^0}$ (GeV/c^2)	[1.774, 1.954]
D^0 All other modes (GeV/c^2)	[1.794, 1.934]
D^0 centre-of-mass momentum (GeV/c)	> 1.3
K^{*-} $m_{K^-\pi^0}$ (GeV/c^2)	[0.767, 1.017]
B^- $m_{D^0K^{*-}}$ (GeV/c^2)	[4.5, 5.5]
ΔE (GeV/c^2)	[-0.200, 0.200]
m_{ES} (GeV/c^2)	[5.20, 5.30]

Table 4.3: A summary of the efficiencies achieved by the preselection cuts on signal, B meson background and continuum background Monte Carlo events.

Mode	Signal	B background	Continuum background
$D^0 \to K^-\pi^+$	0.219	1.5×10^{-5}	9.7×10^{-6}
$D^0 \to K^-\pi^+\pi^0$	0.133	1.0×10^{-4}	1.2×10^{-4}
$D^0 \to K^-\pi^+\pi^-\pi^+$	0.141	1.0×10^{-4}	8.0×10^{-5}
$D^0 \to K^+K^-$	0.184	3.1×10^{-6}	3.4×10^{-6}
$D^0 \to \pi^+\pi^-$	0.178	4.7×10^{-6}	4.4×10^{-6}
$D^0 \to K^0_S\pi^0$	0.038	7.9×10^{-7}	1.1×10^{-6}
$D^0 \to K^0_S\phi$	0.138	8.2×10^{-7}	1.1×10^{-6}
$D^0 \to K^0_S\omega$	0.066	1.5×10^{-5}	1.5×10^{-5}

Chapter 5

Selection

The previous chapter described an initial preselection of events which reduced the background by a factor of between 10^4 and 10^7, depending on mode and background component, while only rejecting between 96% and 78% of the signal events of any given mode under study. This chapter describes the further refinement of the selection criteria, it is designed to achieve the largest signal significance possible by rejecting as much background as possible. This allows us to make an accurate measurement of the signal yields required to measure the GLW quantities. The variables used to discriminate signal events from background events are documented and an overview of the cut optimisation procedure is presented. The method for choosing between candidates when an event has more than one valid candidate is also discussed. Finally the optimised selection efficiency is given and the challenges posed by background processes are identified.

5.1 Discriminating variables

The following variables were used in the event selection:

- Fisher discriminant: A linear combination of discriminating variables which may be correlated [23]. The Fisher discriminant used in this analysis is defined as,

$$\mathcal{F} = -0.60 - 0.30L^0 + 1.16L^2 + 0.75 \mid \cos\theta_{\rm Thr} \mid, \tag{5.1}$$

where $\cos\theta_{\rm Thr}$ is the cosine of the angle between the B meson's momentum vector and the momentum vector of the rest of the event. The zeroth (L^0) and second order (L^2) Legendre polynomials are given by,

$$L^j \;=\; \sum_i p_i^* \mid \cos\theta_i^* \mid^j . \tag{5.2}$$

This is a momentum (p_i^*) weighted summation of the magnitude of the angle the ith track makes with the momentum vector of the reconstructed B meson.

All of these event shape variables work on the principle that when the B meson decays it will be almost at rest in the laboratory frame and so its decay products will be more spherically distributed than the background processes which will not decay while at rest, leading to a two-jet pattern. This Fisher discriminant has been used previously in *BABAR* [15].

- $\cos\theta_H$ (K^{*-}): The cosine of the angle between the K^- in the rest frame of the K^{*-} and the K^{*-} in the rest frame of the B^-. This has a $\cos^2\theta$ distribution for signal events and is peaked towards +1 for background events. There is a strong correlation between this variable and the momentum of the π^0 from the K^{*-}. For this reason this variable is good at rejecting K^{*-} candidates that include a fake low momentum π^0. This angle is sometimes referred to as the K^{*-} decay angle in the literature.

- Helicity angle: The absolute value of the cosine of the helicity of the D^0. The kinematics of the D^0 decay lead to a flat distribution for signal events but a $\cos^2\theta$ distribution for background events.

- $\cos\theta_{BMom}$: The cosine of the angle between the momentum vector of the B^- and the beam axis. Signal events will give a $\sin^2\theta$ distribution while background events will give a flat distribution.

- The invariant masses of the reconstructed particles including the D^0, K^{*-}, K_S^0 and the neutral pions from the D^0, ω and the ϕ.

- The invariant mass of the $B^- \to D^0(K^-\pi^0\pi^+)\pi^-$ system. A veto is applied to the mass of this system to remove this background in the $\pi^+\pi^-$ mode. This removes events where K^- π^0 is mistakenly reconstructed as a K^{*-} leaving two charged pions to be reconstructed as coming from the D^0.

- Kaon and pion particle identification variables (PID) as discussed in Section 3.2.4.

Finally a signal region is defined in the two variables ΔE and $m_{\rm ES}$. In ΔE the signal region is chosen as $\pm 75\,\mathrm{MeV}$ ($\pm 3\sigma$) around zero, while the $m_{\rm ES}$ signal region is defined as $5.27 < m_{\rm ES} < 5.3\,\mathrm{GeV}/c^2$. The definitions of ΔE and $m_{\rm ES}$ are given in Section 4.2.9. The choice of the $m_{\rm ES}$ signal region is standard to *BABAR*.

5.1.1 Data, Monte Carlo event comparison

Before the optimisation procedure several checks were performed on the data. The first check was to ensure that the shapes of the discriminating variables agree for simulated events (Monte Carlo) and on-peak data. Section 4.1 gives an overview of the size of the simulated event samples used in these comparisons.

Figure 5.1 shows a comparison between data and Monte Carlo for all of the variables used in the event selection of $D^0 \to K^-\pi^+$. In each case the distribution is shown after preselection cuts have been applied. The plots have been normalised to unit area because at this stage there are none of the corrections required to account for the reconstruction efficiency differences between data and Monte Carlo for the tracking, π^0 and particle identification selection criteria. The calculation of the corrections is discussed in Section 7.2. There is good agreement between the shape of data and Monte Carlo for all variables shown.

Figure 5.2 shows a similar comparison between off-peak data and continuum Monte Carlo for the decay mode $D^0 \to K^-\pi^+\pi^0$ which has the largest continuum background contribution. Again it is seen that the Monte Carlo gives a good description of the shapes of the distributions.

5.2 Cut optimisation procedure

The cut optimisation procedure has been designed to give the greatest signal significance, by choosing cut values which maximise $\frac{S}{\sqrt{(S+B)}}$, where S is the expected number of signal events and B is the expected number of background events. The values of S and B are the number of signal and background events left after all selection criteria have been applied. The final set of cut values obtained from the optimisation is summarised in Table 5.1.

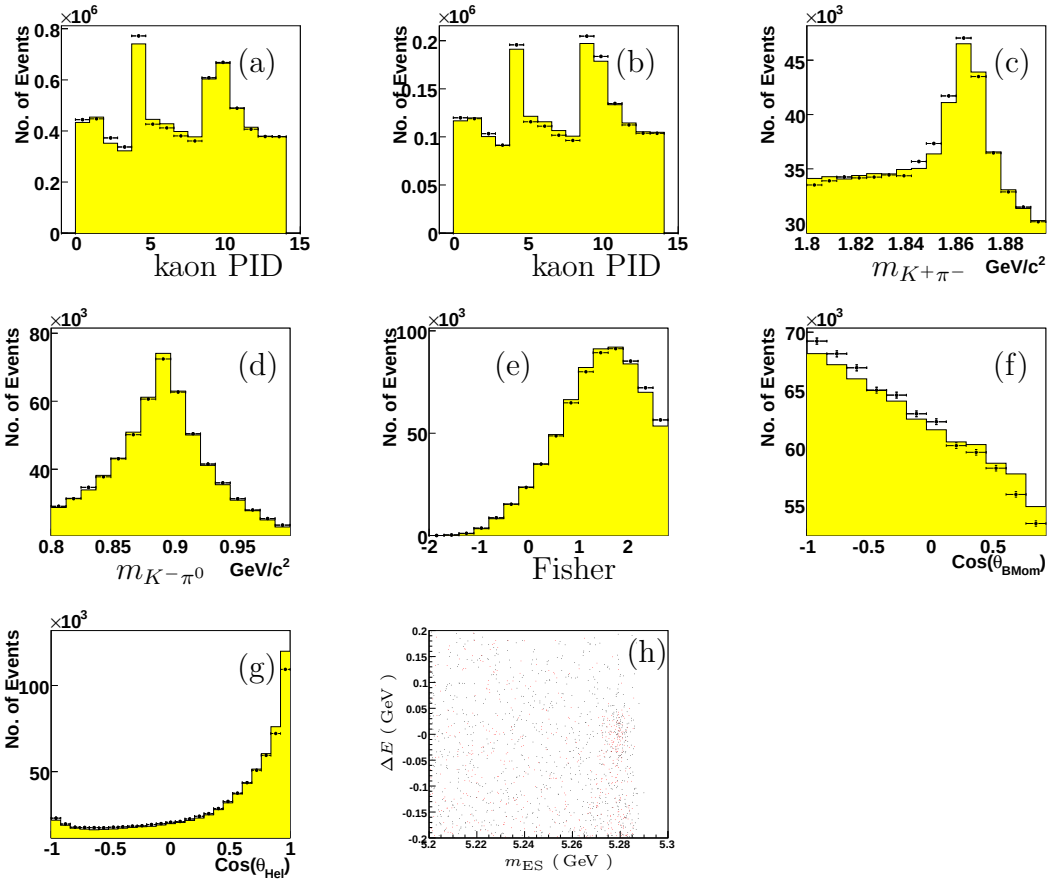

Figure 5.1: Comparison between data and Monte Carlo for variables used in the selection of $B^- \to D^0 K^{*-}$ events with $D^0 \to K^-\pi^+$. The data is marked by the points and the Monte Carlo is the yellow histogram. The distributions are normalised to unit area. All preselection cuts, except for that that applied to the plotted variable, are applied. Plots shown are (a) kaon PID (from K^*), (b) kaon PID (from D^0), (c) D^0 mass, (d) K^* mass, (e) the Fisher discriminant, (f) $\cos\theta_{BMom}$ and (g) $\cos\theta_H$ (K^*). Also shown is a scatter plot (h) of the $m_{\rm ES}$-ΔE plane. Here the red markers indicate Monte Carlo events while the black markers indicate on-peak data.

The variables used have been chosen for their ability to discriminate between signal and background events. The power of each variable is illustrated in Fig. 5.3 which shows the difference in shape between signal and background events for several distributions in the $D^0 \to K^-\pi^+$ mode. The final cut values applied to each variable are also shown. The sample of signal events used has been filtered to include only events where the B meson reconstructed is the B meson generated by the simulation, and not a misreconstruction of the other B meson generated in the event.

The signal branching fraction for $B^- \to D^0 K^{*-}$ obtained by a previous *BABAR*

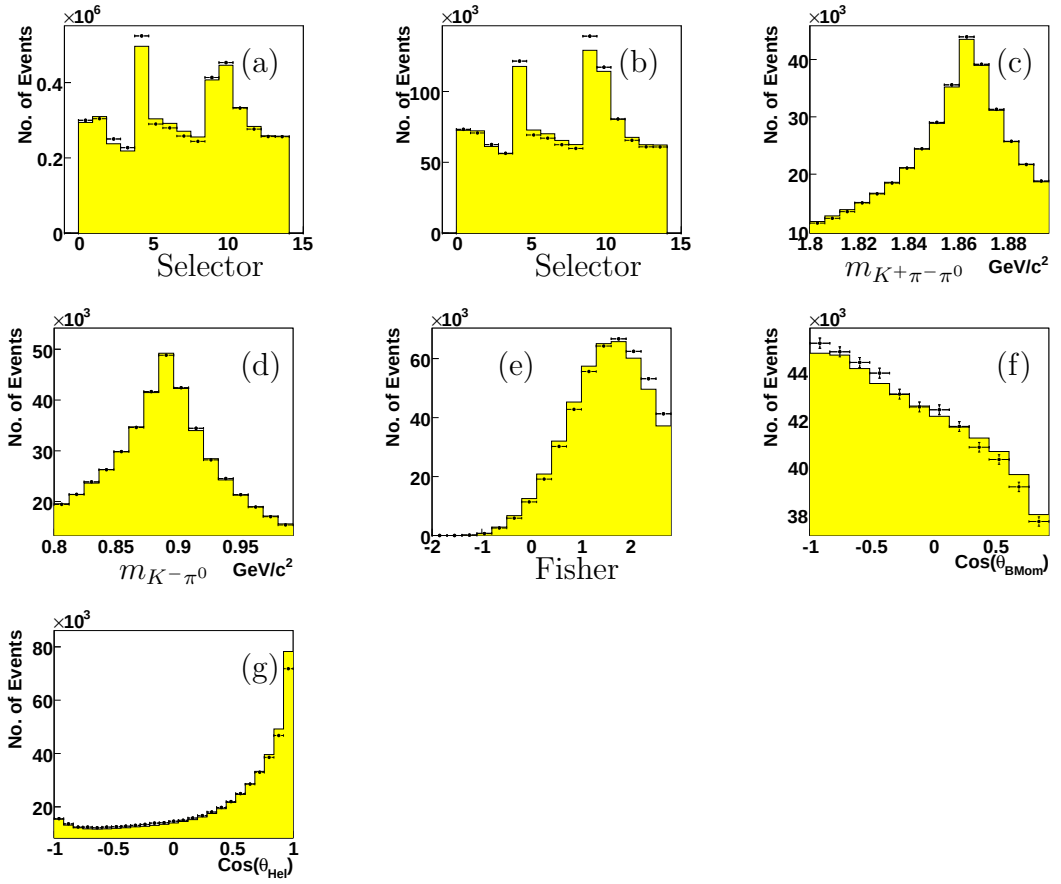

Figure 5.2: Comparison between off-peak data and continuum Monte Carlo for variables used in the selection of $B^- \to D^0 K^{*-}$ events with $D^0 \to K^-\pi^+\pi^0$. The data are shown as points, the Monte Carlo as the yellow histogram. The distributions are normalised to unit area. At this stage no cuts are applied beyond those in the preselection. Plots shown are (a) kaon PID (from K^*), (b) kaon PID (from D^0), (c) D^0 mass, (d) K^* mass, (e) the Fisher discriminant, (f) $\cos\theta_{BMom}$ and (g) $\cos\theta_H$ (K^*).

analysis of 6.3×10^{-4} has been assumed [13]. This measurement is more precise than the current Particle Data Group average [12].

The cut variables were optimised individually after all other cuts except ΔE and $m_{\rm ES}$ had been applied. It is clear that the final ΔE and $m_{\rm ES}$ cuts will have a significant impact on the size of the remaining background, however, they could not be applied because too few events were left to allow an accurate choice of selection criteria. To achieve the correct normalisation the effect of these cuts was mimicked by scaling down the measured size of each of the component Monte Carlo samples. The scaling factor was found by taking the ratio, after the set of cuts being optimised

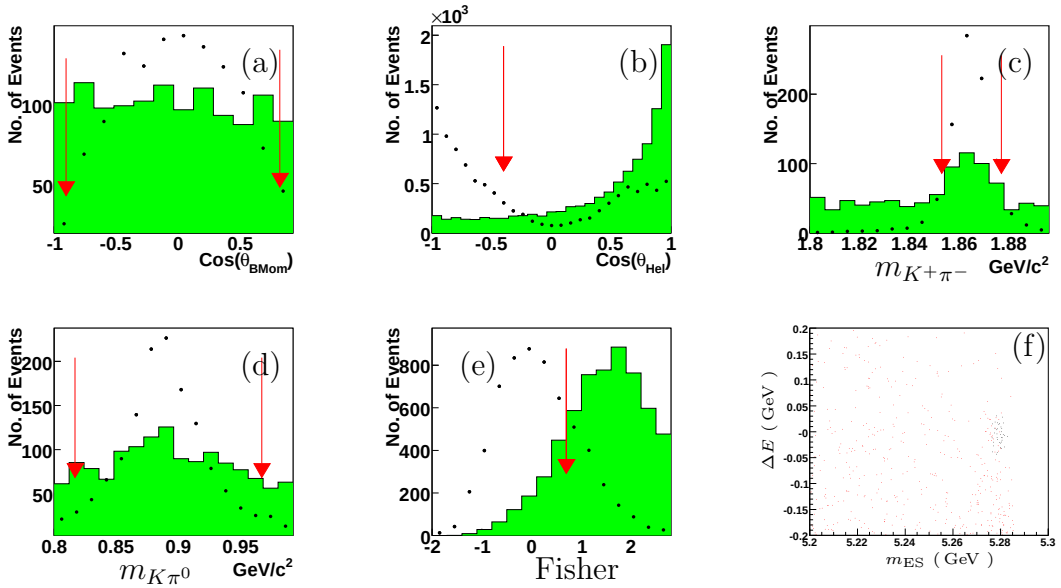

Figure 5.3: Comparison between signal and background in Monte Carlo for variables used in the selection of $B^- \to D^0 K^{*-}$ events with $D^0 \to K^-\pi^+$. The signal is shown as black dots and the background as the green histogram. The distributions are normalised to unit area to illustrate the rejection power of each cut. All cuts are applied with the exception of the cut on the variable shown. The optimised cut values are indicated by the red arrows. Plots shown are (a) $\cos\theta_{BMom}$, (b) $\cos\theta_H$ (K^*), (c) D^0 mass, (d) K^* mass and (e) the Fisher discriminant. Also shown is a scatter plot (f) of the $m_{\rm ES}$-ΔE plane with no cuts applied. Here the red dots indicate background Monte Carlo events while the black dots indicate signal Monte Carlo events.

has been applied, of the number of events in the signal box ($N_{\rm A}$) of the sample to the total number of events of that sample ($N_{\rm B}$). Regions A and B are illustrated in Fig. 5.4. This leads to a modified calculation of the significance of a particular set of cuts with $\frac{S}{\sqrt{S+B}}$ being replaced by $\frac{S}{\sqrt{S+\sum R_i \times B_i}}$. Where the ith sample of background events have a scaling factor, $R_i = \frac{N^i_{\rm A}}{N^i_{\rm B}}$, applied to the number of background events found B_i.

The optimisation procedure was iterated with the cut values set to the values suggested by the previous iteration until the optimal cut value for each variable was insensitive to the cuts placed on the other variables. No change to the optimal cut values was found after the last iteration.

In order to reduce potential systematic errors when calculating the ratios that form $\mathcal{A}_\pm$ and $\mathcal{R}_\pm$, wherever possible the cuts applied in this analysis were chosen to be consistent across all modes. Figure 5.5 shows that the effect of these modifications to the selection criteria have an insignificant effect on the significance of the selection.

Table 5.1: Cut values are determined from the optimisation procedure and are in addition to those applied in the preselection.

Cut	Cuts common to all modes		
$\mid \Delta E \mid$ (MeV)	< 75		
$\mid m_{\rm ES} - 5279 \mid$ (MeV/c^2)	< 9		
$\mid m_{K^{*-}} - m^{PDG}_{K^{*-}} \mid$ (MeV/c^2)	< 75		
$\cos\theta_H$ (K^{*-})	< -0.4		
Kaon Id (K^{*-})	Applied		
Cut	$D^0 \to K^-\pi^+$	$D^0 \to K^-\pi^+\pi^0$	$D^0 \to K^-\pi^+\pi^-\pi^+$
Fisher discriminant	< 0.7		
$\mid cos\theta_{BMom} \mid$	< 0.9		
$m_{D^0} - m^{PDG}_{D^0}$ (MeV/c^2)	± 12	$-29; +24$	± 12
m_{π^0} (MeV/c^2) (D^0)	-	$125 \to 145$	-
Kaon Id (D^0)	Applied		
Cut	$D^0 \to K^0_S\pi^0$	$D^0 \to K^0_S\omega$	$D^0 \to K^0_S\phi$
Fisher discriminant	< 0.7		< 1.0
$\mid cos\theta_{BMom} \mid$	< 0.9		—
$m_{D^0} - m^{PDG}_{D^0}$ (MeV/c^2)	± 30	± 20	± 12
$\mid m_{K^0_S} - m^{PDG}_{K^0_S} \mid$ (MeV/c^2)	< 6		< 12
$\mid \cos\theta_H \mid$ (D^0)	< 0.7	< 0.9	—
$\mid m_\omega - m^{PDG}_\omega \mid$ (MeV/c^2)	—	< 20	—
Pion Id (ω)	—	Applied	—
$\mid m_\phi - m^{PDG}_\phi \mid$ (MeV/c^2)	—	—	< 12
Kaon Id (ϕ)	—	—	Applied
Cut	$D^0 \to \pi^+\pi^-$	$D^0 \to K^+K^-$	
Fisher discriminant	< 0.7		
$\mid cos\theta_{BMom} \mid$	< 0.9		
$m_{D^0} - m^{PDG}_{D^0}$ (MeV/c^2)	± 12		
$\mid \cos\theta_H(D^0) \mid$	< 0.9		
Kaon Id (D^0)	Applied	—	
Pion Id (D^0)	—	Applied	
Veto (MeV/c^2)	> 25	—	

This can be seen by comparing the position of the arrow or cross with the position of the maxima within the plot.

Figure 5.5 shows $\frac{S}{\sqrt{(S+B)}}$ as a function of the cut variable for the $D^0 \to K^-\pi^+$ mode. Where a single cut is applied a one-dimensional histogram is shown. A two-dimensional histogram is shown where the variable has lower and upper cuts applied, typically specifying a central region to select events from like a mass peak. The colour of each bin in the two-dimensional histograms indicates the significance a cut at that point would achieve ranging from a low significance (blue) to a large significance (red).

The selection criteria resulting from this optimisation procedure are summarised in Table 5.1.

5.3 Multiple candidate arbitration

The number of candidates per event in signal Monte Carlo after applying all selection cuts is shown on a logarithmic scale in Fig. 5.6. Typically less than 10% of events have more than one candidate.

If an event has a single candidate it is selected, however, in the case that an event has multiple candidates a decision must be made. Two algorithms have been investigated to arbitrate this decision:

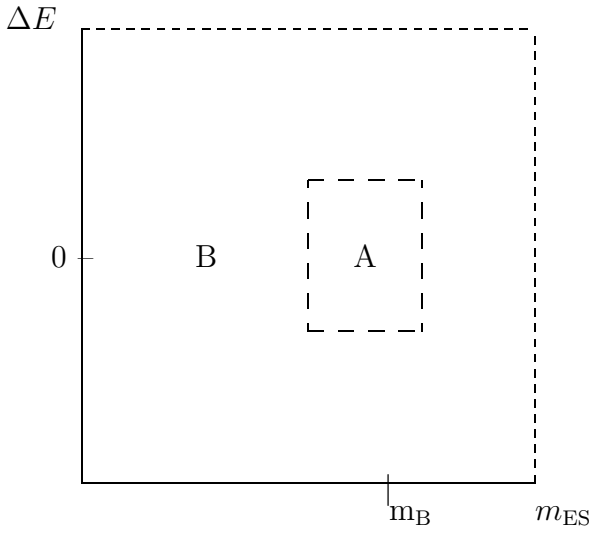

Figure 5.4: Box A is the signal region while box B encompasses the entire $m_{\rm ES}$, ΔE plane.

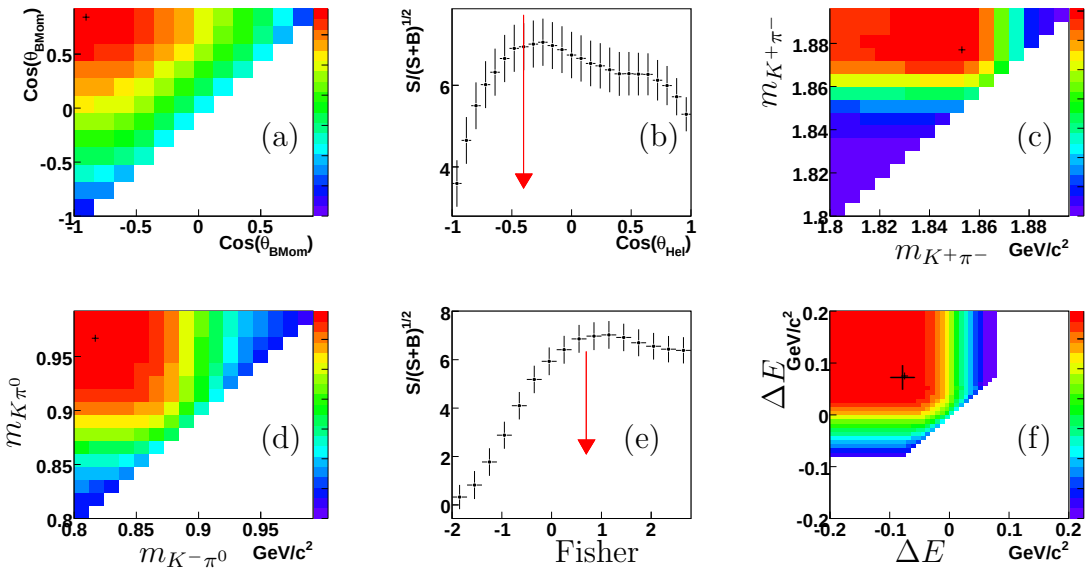

Figure 5.5: $\frac{S}{\sqrt{(S+B)}}$as a function of the cut variable for the event selection cuts used to select $B^- \to D^0 K^{*-}$ events with $D^0 \to K^-\pi^+$. In each case, all other cuts have been applied. The chosen cut value is indicated by an arrow(cross) for a 1(2) dimensional optimisation. Plots of significance are shown for the variables (a) $\cos\theta_{BMom}$, (b) $\cos\theta_H$ (K^*), (c) D^0 mass, (d) K^* mass, (e) the Fisher discriminant and (f) ΔE.

- choosing the candidate with the smallest $\mid \Delta E \mid$;
- choosing the candidate with the smallest χ^2, defined as:

$$\chi^2 = \frac{(m(D^0) - m(D^0)_{PDG})^2}{\sigma^2(m(D^0))} + \frac{(m(K^{*-}) - m(K^{*-})_{PDG})^2}{\sigma^2(m(K^{*-})) + \Gamma^2(K^{*-})}. \tag{5.3}$$

Note that the natural width of the K^{*-} is included in the χ^2 definition because it is much larger than the uncertainty on the fitted mass value.

To evaluate the effectiveness of the algorithms the signal Monte Carlo has been used to find how often, in the case of multiple reconstructed candidates passing all of the cuts, the correct B^- is chosen. The results are presented in table 5.2.

Given that the χ^2 algorithm is the better performing in almost all cases, it has been used as the selection criterion when a choice between several candidates is required. It also has the benefit of avoiding any potential bias in the ΔE distribution.

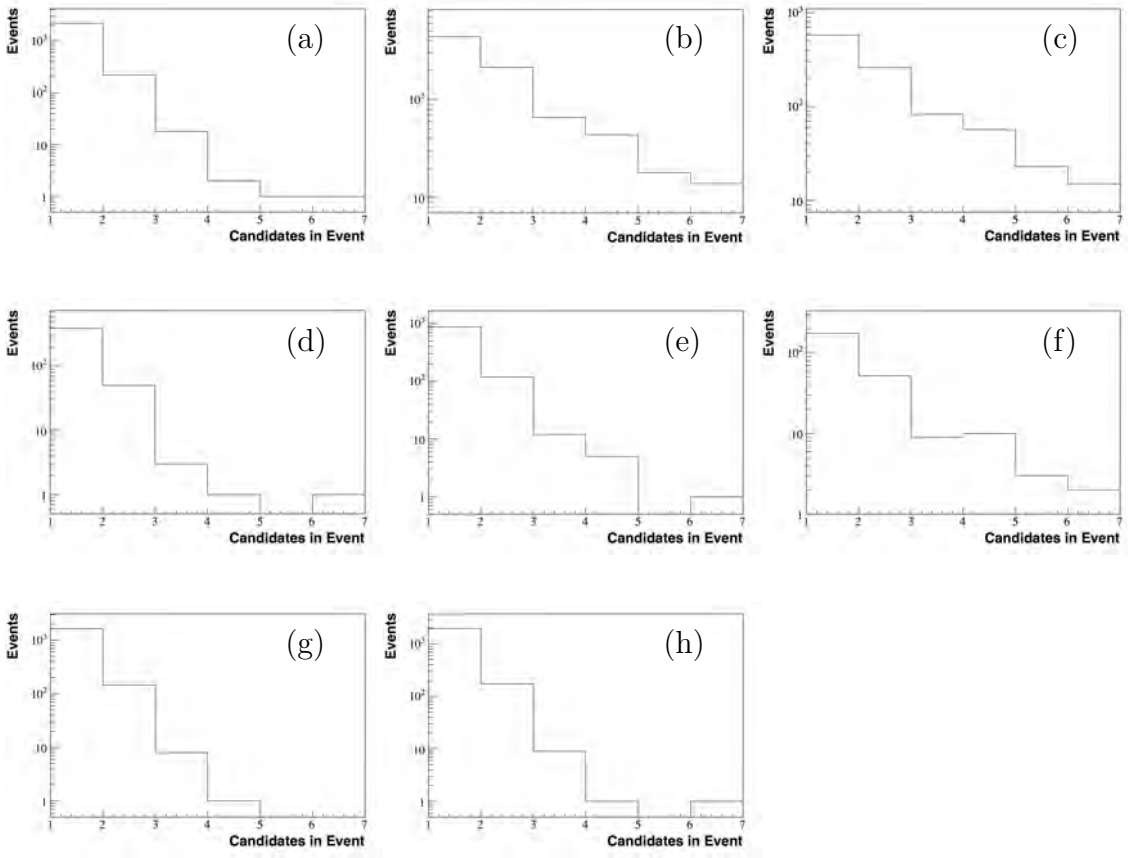

Figure 5.6: The number of B^- candidates per event after all selection cuts have been applied for: (a) $D^0 \to K^-\pi^+$, (b) $D^0 \to K^-\pi^+\pi^0$, (c) $D^0 \to K^-\pi^+\pi^-\pi^+$, (d) $D^0 \to K^0_S\pi^0$, (e) $D^0 \to K^0_S\phi$, (f) $D^0 \to K^0_S\omega$, (g) $D^0 \to K^+K^-$ and (h) $D^0 \to \pi^+\pi^-$. A logarithmic scale has been used.

Table 5.2: Fraction of true B^- candidates selected in signal Monte Carlo, when there are two or more candidates passing the selection cuts. Results are shown after all analysis cuts have been applied.

Mode	>0 candidates	>1 candidate	$\mid \Delta E \mid$	χ^2
$D^0 \to K^-\pi^+$	2534	164	71 ± 6%	78 ± 6%
$D^0 \to K^-\pi^+\pi^0$	1068	191	66 ± 5%	79 ± 5%
$D^0 \to K^-\pi^+\pi^-\pi^+$	1059	181	65 ± 5%	74 ± 5%
$D^0 \to \pi^+\pi^-$	2139	135	78 ± 8%	73 ± 8%
$D^0 \to K^+K^-$	2067	148	72 ± 7%	73 ± 7%
$D^0 \to K^0_S\pi^0$	384	35	76 ± 13%	80 ± 13%
$D^0 \to K^0_S\phi$	1137	108	67 ± 9%	77 ± 9%
$D^0 \to K^0_S\omega$	262	44	63 ± 11%	63 ± 11%

5.4 Preliminary yields

The efficiency for selecting signal events, as determined from simulated events, is presented in Table 5.4. The expected yield of events in the data sample is also presented. The following method was used to extract these yields. All analysis cuts except $m_{\rm ES}$ were applied including a $\pm 3\sigma$ slice in ΔE. The $m_{\rm ES}$ distribution was then fitted with a Gaussian (Signal), an Argus[1] function (uds, $c\overline{c}$, $B^0\overline{B}^0$) or a Gaussian + Argus (B^+B^-). Note that at this stage no efficiency corrections are applied to the Monte Carlo but are considered later for the $\mathcal{R}_\pm$ measurement (see section 7.2). The efficiency measured in the $K^0_S\pi^0$ mode was found to be lower than the efficiency of the $K^0_S\omega$ mode. This was found to be because the D^0 mass resolution is worse in the $K^0_S\pi^0$ mode for two reasons. The first is that the kinematics of the omega decay allows for a mass constraint to be applied to its reconstruction. The second contributing factor is that any errors in the measurement of the π^0 mass from the calorimeter have a smaller impact on the measured D^0 mass in the $K^0_S\omega$ mode because the π^0 makes up a smaller component. This means that it is easier to mis-reconstruct the D^0 candidate in the $K^0_S\pi^0$ decay channel.

Table 5.3 presents the number of background events expected in $185.8\,\mathrm{fb}^{-1}$ (based on Monte Carlo) split into the sources of the background. Any signal events in the B^+B^- sample are excluded based on truth information created by the simulation. The peaking background is background which behaves like signal in ΔE and $m_{\rm ES}$. The number of excluded signal events is consistent with the results in Table 5.4 which shows the expected yield on this size data sample.

The cut by cut effect on efficiency of the signal, $B\overline{B}$ background and continuum background samples is detailed in tables 5.5 to 5.7 for the non-CP, CP-odd and CP-even modes respectively. The efficiencies shown in Table 5.4 are calculated with a fit to $m_{\rm ES}$, however, the efficiencies found in tables 5.5 to 5.7 are based on a simple cut and count method which results in small differences.

5.5 Cross-feed

Cross-feed occurs when a track from the second B in the event is misreconstructed as coming from the signal B, or when a track from the signal B is misreconstructed

[1]The Argus function is described in more detail in Section 5.6

Table 5.3: The number of background events obtained from various simulated event samples. The number of events expected is scaled to $185.8\,\mathrm{fb}^{-1}$ and is found after applying all analysis cuts with the exception of m_{ES}, which is fitted.

Mode ($D^0 \to$)	uds	$c\overline{c}$	$B^0\overline{B}^0$	B^+B^- (Argus)	B^+B^- (Peaking)
$K^-\pi^+$	3.6 ±1.2	7.6 ±1.7	0.8±0.4	4.9±1.5	16.6±3.1
$K^-\pi^+\pi^0$	49.2±4.6	76.7±5.7	16.1±1.9	26.9±3.7	34.0±6.4
$K^-\pi^+\pi^-\pi^+$	17.1±2.6	76.8±50.9	18.3±0.6	27.8±2.7	8.0±2.6
$\pi^+\pi^-$	1.4 ±0.8	1.9 ±0.9	0.6±0.4	1.5±0.8	3.5±1.5
K^+K^-	4.6 ±11.9	1.9 ±0.8	0.4±0.2	1.8±0.7	0.0±0.0
$K^0_S\pi^0$	0.6 ±0.9	0.7 ±0.5	0.1±0.1	1.0±0.6	0.0±0.0
$K^0_S\phi$	0.0 ±0.0	1.2 ±0.7	0.1±0.4	0.7±0.5	0.0±0.1
$K^0_S\omega$	5.4 ±1.6	11.6±2.2	2.0±0.6	3.4±1.0	0.4±0.7

Table 5.4: Efficiency determined from signal Monte Carlo. The expected yield from $185.8\,\mathrm{fb}^{-1}$ is also given. For comparison the number of background events is given. The efficiency is found after applying all analysis cuts with the exception of m_{ES}, which is fitted.

Mode	Efficiency	Expected no. of events	Expected background
$D^0 \to K^-\pi^+$	5.4 ± 0.11 %	79.7 ± 1.7	33.5 ± 4.1
$D^0 \to K^-\pi^+\pi^0$	2.6 ± 0.08 %	132.7 ± 4.3	202.8 ± 10.5
$D^0 \to K^-\pi^+\pi^-\pi^+$	3.0 ± 0.10 %	88.2 ± 2.9	147.9 ± 51.1
$D^0 \to K^+K^-$	4.4 ± 0.09 %	6.7 ± 0.2	9.0 ± 2.1
$D^0 \to \pi^+\pi^-$	4.2 ± 0.10 %	2.3 ± 0.1	8.7 ± 12.0
$D^0 \to K^0_S\pi^0$	0.7 ± 0.04 %	7.3 ± 0.4	2.4 ± 8.9
$D^0 \to K^0_S\phi$	3.3 ± 0.10 %	2.8 ± 0.1	2.0 ± 0.9
$D^0 \to K^0_S\omega$	1.1 ± 0.07 %	3.5 ± 0.2	22.9 ± 3.1

in the wrong part of the decay chain. These events cause problems because they add a background. This effect could be a particular problem if it was discovered that non-CP modes were being misreconstructed in the low branching ratio CP modes.

The full analysis chain for each mode was applied to each sample of signal Monte Carlo to look for cross-feed between modes. The majority of modes showed no events reconstructed incorrectly in another signal mode. Three modes show a small cross-feed (less than 0.3 ± 0.2 events expected per $185.8\,\mathrm{fb}^{-1}$). The largest cross-feed seen was in the mode $D^0 \to K^-\pi^+\pi^-\pi^+$ which shows 0.85 ± 0.4 events reconstructed as $D^0 \to K^-\pi^+\pi^0$. This is not significant given the expected yield is in the region of 90 events for this mode. Because the effect of the cross-feed is small in comparison to other sources of systematic uncertainty, its effect is neglected from the final result.

Table 5.5: Effect of cuts on signal and background. Each column shows the cumulative efficiency after applying that and all previous cuts.

Cut	Signal	$B\overline{B}$ Background	$uds + c\overline{c}$ Background
$D^0 \to K^-\pi^+$			
Preselection	0.219	1.5×10^{-5}	9.7×10^{-6}
PID K (K*)	0.208	1.4×10^{-5}	8.9×10^{-6}
PID K (D^0)	0.204	1.3×10^{-5}	7.7×10^{-6}
$m_{K*} - m_{K*}^{PDG}$	0.198	1.3×10^{-5}	7.4×10^{-6}
$m_{D^0} - m_{D^0}^{PDG}$	0.185	1.2×10^{-5}	6.4×10^{-6}
$\cos\theta_H$ (K*)	0.088	1.3×10^{-6}	3.3×10^{-6}
$\cos\theta_{BMom}$	0.082	1.2×10^{-6}	3.2×10^{-6}
Fisher	0.061	7.8×10^{-7}	4.4×10^{-7}
ΔE-$m_{\rm ES}$	0.053	1.1×10^{-7}	2.6×10^{-8}
$D^0 \to K^-\pi^+\pi^0$			
Preselection	0.133	1.1×10^{-4}	1.2×10^{-4}
mass π^0 (D^0)	0.119	9.8×10^{-5}	1.1×10^{-4}
PID K (K*)	0.112	9.3×10^{-5}	1.0×10^{-4}
PID K (D^0)	0.110	7.2×10^{-5}	8.1×10^{-5}
$m_{K*} - m_{K*}^{PDG}$	0.107	6.9×10^{-5}	7.8×10^{-5}
$m_{D^0} - m_{D^0}^{PDG}$	0.099	6.5×10^{-5}	7.3×10^{-5}
$\cos\theta_H$ (K*)	0.043	8.8×10^{-6}	3.8×10^{-5}
$\cos\theta_{BMom}$	0.042	8.4×10^{-6}	3.7×10^{-5}
Fisher	0.031	4.7×10^{-6}	4.4×10^{-6}
ΔE-$m_{\rm ES}$	0.023	3.0×10^{-7}	1.6×10^{-7}
$D^0 \to K^-\pi^+\pi^-\pi^+$			
Preselection	0.141	1.0×10^{-4}	8.0×10^{-5}
PID K (K*)	0.136	9.9×10^{-5}	7.6×10^{-5}
PID K (D^0)	0.126	7.6×10^{-5}	5.8×10^{-5}
$m_{K*} - m_{K*}^{PDG}$	0.123	7.3×10^{-5}	5.6×10^{-5}
$m_{D^0} - m_{D^0}^{PDG}$	0.111	6.3×10^{-5}	4.8×10^{-5}
$\cos\theta_H$ (K*)	0.051	9.4×10^{-6}	2.6×10^{-5}
$\cos\theta_{BMom}$	0.050	8.9×10^{-6}	2.6×10^{-5}
Fisher	0.036	4.8×10^{-6}	2.8×10^{-6}
ΔE-$m_{\rm ES}$	0.028	3.1×10^{-7}	7.5×10^{-8}

Table 5.6: Effect of cuts on signal and background. Each column shows the cumulative efficiency after applying that and all previous cuts.

Cut	Signal	$B\overline{B}$ Background	uds + c Background
$D^0 \to K^0_S\pi^0$			
Preselection	0.038	7.9×10^{-7}	1.1×10^{-6}
$m_{K^0_S} - m^{PDG}_{K^0_S}$	0.037	7.4×10^{-7}	1.0×10^{-6}
PID K (K*)	0.035	7.1×10^{-7}	9.8×10^{-7}
$m_{K*} - m^{PDG}_{K*}$	0.034	6.7×10^{-7}	9.6×10^{-7}
$m_{D^0} - m^{PDG}_{D^0}$	0.032	6.1×10^{-7}	8.9×10^{-7}
$\cos\theta_H$ (K*)	0.016	1.4×10^{-7}	5.1×10^{-7}
$\cos\theta_H$ (D^0)	0.013	9.6×10^{-8}	3.4×10^{-7}
$\cos\theta_{BMom}$	0.013	9.2×10^{-8}	3.2×10^{-7}
Fisher	0.010	3.9×10^{-8}	5.6×10^{-8}
ΔE-$m_{\rm ES}$	0.008	7.0×10^{-9}	1.5×10^{-8}
$D^0 \to K^0_S\phi$			
Preselection	0.138	8.2×10^{-7}	1.1×10^{-6}
$m_{K^0_S} - m^{PDG}_{K^0_S}$	0.137	8.1×10^{-7}	1.0×10^{-6}
$m_\phi - m^{PDG}_\phi$	0.134	8.0×10^{-7}	1.0×10^{-6}
PID K (K*)	0.126	7.7×10^{-7}	9.5×10^{-7}
PID Daughters of D^0	0.121	6.9×10^{-7}	8.5×10^{-7}
$m_{K*} - m^{PDG}_{K*}$	0.117	6.5×10^{-7}	8.2×10^{-7}
$m_{D^0} - m^{PDG}_{D^0}$	0.112	5.7×10^{-7}	7.1×10^{-7}
$\cos\theta_H$ (K*)	0.046	7.3×10^{-8}	2.9×10^{-7}
Fisher	0.038	4.8×10^{-8}	5.1×10^{-8}
ΔE-$m_{\rm ES}$	0.033	4.6×10^{-9}	2.8×10^{-9}
$D^0 \to K^0_S\omega$			
Preselection	0.066	1.5×10^{-5}	1.5×10^{-5}
$m_{K^0_S} - m^{PDG}_{K^0_S}$	0.063	1.4×10^{-5}	1.4×10^{-5}
$m_\omega - m^{PDG}_\omega$	0.058	1.3×10^{-5}	1.3×10^{-5}
PID K (K*)	0.055	1.2×10^{-5}	1.3×10^{-5}
PID Daughters of D^0	0.054	1.2×10^{-5}	1.2×10^{-5}
$m_{K*} - m^{PDG}_{K*}$	0.053	1.2×10^{-5}	1.2×10^{-5}
$m_{D^0} - m^{PDG}_{D^0}$	0.049	1.1×10^{-5}	1.1×10^{-5}
$\cos\theta_H$ (K*)	0.021	1.7×10^{-6}	5.4×10^{-6}
$\cos\theta_H$ (D^0)	0.020	1.5×10^{-6}	5.2×10^{-6}
$\cos\theta_{BMom}$	0.020	1.4×10^{-6}	5.1×10^{-6}
Fisher	0.013	6.4×10^{-7}	5.2×10^{-7}
ΔE-$m_{\rm ES}$	0.010	1.5×10^{-7}	1.5×10^{-8}

Table 5.7: Effect of cuts on signal and background. Each column shows the cumulative efficiency after applying that and all previous cuts.

Cut	Signal	$B\overline{B}$ Background	uds + c Background
$D^0 \to K^+K^-$			
Preselection	0.184	3.1×10^{-6}	3.4×10^{-6}
PID K (K*)	0.175	2.9×10^{-6}	3.2×10^{-6}
PID K (D^0)	0.168	2.3×10^{-6}	2.6×10^{-6}
$m_{K*} - m_{K*}^{PDG}$	0.164	2.2×10^{-6}	2.6×10^{-6}
$m_{D^0} - m_{D^0}^{PDG}$	0.156	1.8×10^{-6}	2.2×10^{-6}
$\cos\theta_H$ (K*)	0.073	3.4×10^{-7}	1.1×10^{-6}
$\cos\theta_H$ (D^0)	0.070	3.2×10^{-7}	1.1×10^{-6}
$\cos\theta_{BMom}$	0.069	3.1×10^{-7}	4.2×10^{-7}
Fisher	0.051	1.7×10^{-7}	4.9×10^{-8}
ΔE-$m_{\rm ES}$	0.044	2.9×10^{-8}	6.8×10^{-9}
$D^0 \to \pi^+\pi^-$			
Preselection	0.178	4.7×10^{-6}	4.4×10^{-6}
PID K (K*)	0.170	4.5×10^{-6}	4.1×10^{-6}
PID K (D^0)	0.166	4.4×10^{-6}	3.9×10^{-6}
$m_{K*} - m_{K*}^{PDG}$	0.161	4.3×10^{-6}	3.8×10^{-6}
$m_{D^0} - m_{D^0}^{PDG}$	0.151	3.3×10^{-6}	3.0×10^{-6}
Veto (D^0)	0.151	3.3×10^{-6}	3.0×10^{-6}
$\cos\theta_H$ (K*)	0.070	4.9×10^{-7}	1.5×10^{-6}
$\cos\theta_H$ (D^0)	0.066	4.3×10^{-7}	1.4×10^{-6}
$\cos\theta_{BMom}$	0.065	2.9×10^{-7}	8.3×10^{-7}
Fisher	0.048	9.2×10^{-7}	1.0×10^{-7}
ΔE-$m_{\rm ES}$	0.042	1.6×10^{-8}	2.7×10^{-9}

5.6 Background studies

The background present in the signal region after all cuts have been applied falls into two categories:

- **Continuum background.** This arises from continuum processes ($e^+e^- \to q\overline{q}$) and combinatoric background from other B meson decays.

- **Peaking background.** Peaking backgrounds are those that behave like signal in the signal region distributions ΔE and $m_{\rm ES}$. Their contribution cannot be extracted from the fit to $m_{\rm ES}$ in the signal region but must instead be determined from other sources.

By looking at the truth information (Tables 5.8 - 5.10) of simulated events it can be seen that three processes in particular contribute to the peaking background:

- The non-resonant decay $B^- \to D^0 K^- \pi^0$. The branching fraction for this decay is unknown. As these events contain both a correctly reconstructed D^0 and B^-, it will behave like signal in all distributions used in the yield estimation procedure. It must therefore be accounted for separately, and is studied in Section 7.4.4;

- B^- decays with a final state similar to that of the signal mode but which do not contain a D^0 in the decay. This is almost exclusively where the B^- decays to $D^{*0}X$. This background occurs when the extra π^0 or γ associated with the D^{*0} has been missed in the reconstruction. The size of this background can be estimated by looking at the $m_{\rm ES}$ distribution of events away from the signal region of the D^0 invariant mass distribution;

- Decays to D^0 X where the kaon has been misidentified due to a failure of the particle identification algorithm. X is most commonly a ρ^-, a_1^- or π^-, which means that these events contain a fake K^{*-}. Where available a high statistics simulated event sample is used to make an accurate prediction of the number of events due to each mode in this category. If no pure sample is available the number of events found in the generic sample is used with a conservative 100% error assigned.

The fit strategy described in the next chapter must take into account each of these background components in order to provide an accurate measurement of the yields in each mode.

Table 5.8: The composition of the peaking background events after all cuts have been applied is found by looking at truth information in the signal region of the $K^-\pi^+$ mode. The total number of background events found after scaling to $185.8\,\mathrm{fb}^{-1}$ was 19.5. Below, X indicates other particles, most commonly a single ρ^-, a_1^-, π^- or in the case of the D^{*0} also K^{*-}.

Mode	# events seen
$D^0 K\pi^0$	11.7 ± 0.1
D^{*0} X	1.4 ± 0.6
D^0 X	4.5 ± 0.5

Table 5.9: The composition of the peaking background events found by looking at truth information in the signal region of the $K^-\pi^+\pi^0$ mode. The total number of background events was 56.4. All cuts have been applied. Below X indicates other particles, most commonly a single ρ^-, a_1^-, π^-. Y is usually a K^{*-}.

Mode	# events seen
$D^0 K\pi^0$	20.6 ± 0.1
D^0 X	9.9 ± 0.3
D^{*0} Y	25.1 ± 0.3

Table 5.10: The composition of the peaking background events found by looking at truth information in the signal region of the $K^-\pi^+\pi^-\pi^+$ mode. The total number of background events was 26.9. All cuts have been applied. Below X indicates other particles, most commonly a single ρ^-, a_1^-, π^- and in the case of the D^{*0} also K^{*-}.

Mode	# events seen
$D^0 K\pi^0$	12.1 ± 0.1
D^{*0} X	4.5 ± 0.4
D^0 X	9.0 ± 0.3

5.7 Summary

The chapter has produced a set of selection criteria from which an estimate of the expected signal yields has been been. The likely backgrounds and their composition have also been investigated. In the next chapter a yield estimation strategy will be developed, this will take into account the effect of these backgrounds, in order to accurately estimate the signal yields required to measure $\mathcal{A}_\pm$ and $\mathcal{R}_\pm$.

Chapter 6

Measuring signal yields

So far, we have worked with samples of simulated events to establish selection criteria (cuts) optimised to achieve the largest signal significance possible. The next stage of the analysis is to estimate the number of signal events in the data accurately.

In Section 2.4.1 it was shown that the GLW quantities can be defined in terms of rates:

$$\mathcal{A}_{\pm} = \frac{\Gamma\left(B^- \to D^0_{\pm} K^{*-}\right) - \Gamma\left(B^+ \to D^0_{\pm} K^{*+}\right)}{\Gamma\left(B^- \to D^0_{\pm} K^{*-}\right) + \Gamma\left(B^+ \to D^0_{\pm} K^{*+}\right)} = \frac{\pm 2 r_B \sin\delta \sin\gamma}{1 \pm 2 r_B \cos\delta \cos\gamma + r_B^2}; \tag{6.1}$$

$$\mathcal{R}_{\pm} = \frac{\Gamma\left(B^- \to D^0_{\pm} K^{*-}\right) + \Gamma\left(B^+ \to D^0_{\pm} K^{*+}\right)}{\Gamma(B^- \to D^0 K^{*-})} = 1 \pm 2 r_B \cos\delta \cos\gamma + r_B^2. \tag{6.2}$$

The event yields which can be related to these rates are the number of non-CP ($\Gamma\left(B^- \to D^0 K^{*-}\right)$) signal events and the number of both positive and negative signal events in the CP-odd ($\Gamma\left(B^+ \to D^0_- K^{*+}\right)$ and $\Gamma\left(B^- \to D^0_- K^{*-}\right)$) and CP-even ($\Gamma\left(B^+ \to D^0_+ K^{*+}\right)$ and $\Gamma\left(B^- \to D^0_+ K^{*-}\right)$) samples.

Even after applying the selection criteria developed in the previous chapter, we do not have complete separation of signal and background events. In order to accurately estimate the signal yields we use three distributions: ΔE, $m_{\rm ES}$ (see Section 4.2.9) and the invariant mass of the D^0 candidate.

The determination of the signal yields must include probability distribution functions (PDFs) to model signal and background components. The total PDF will be a weighted sum of the PDFs of each of these components.

Once a yield estimation strategy is developed, toy Monte Carlo experiments are used to test the robustness of the results obtained. Finally the strategy is applied to the events recorded by the *BABAR* detector and the signal yields are measured.

6.1 Region definitions and data sets

All simulated event samples used to create the fit estimation strategy have been selected to give an equivalent integrated luminosity of $185.8\,\text{fb}^{-1}$. This is the same luminosity as the on-peak data sample used which means that the Monte Carlo event samples do not have to be weighted.

The selection criteria developed in Chapter 5 are applied to the on-peak data and to the Monte Carlo to create two distinct data sets. The yield estimation procedure requires that these data sets must be split into three phase-space regions based on m_{ES}, ΔE and the D^0 invariant mass. These regions of phase-space require the definition of signal, upper and lower sideband regions for each of these distributions. A sideband is simply a region of a distribution's phase-space that is away from the signal region. This is illustrated in Fig. 6.1. Sidebands are useful because they allow us to estimate the size of a background component and extrapolate this effect into the signal region to form an estimate of the background's effect on the signal yield. Lower and upper sideband regions must be defined for the invariant mass of the D^0 and ΔE. The signal regions will be centred around $5.27\,\text{GeV}/c^2$ for m_{ES}, $0\,\text{GeV}$ for ΔE and $1.87\,\text{GeV}/c^2$ for the invariant mass of the D^0 candidate.

Table 6.1 shows the definitions of the regions used for the invariant mass distribution of the reconstructed D^0. The signal region is decided upon by optimising a cut on this variable after all other cuts have been applied, as per the standard cut optimisation procedure detailed in Section 5.2. The sidebands were decided upon by fitting the mass distribution of the D^0 on the on-peak data set. A Gaussian PDF was fitted and a total average resolution of $10.58\,\text{MeV}$ was found, however the average resolution of the CP-even and CP-odd modes was closer to $12.5\,\text{MeV}$. This larger value was used for σ because a more conservative definition would only have the drawback of a slightly smaller event sample. The sideband definition used was $4\sigma < m_{D^0} < 8\sigma$.

Table 6.2 gives the region definitions used in ΔE. The variation in ΔE (σ) was found by fitting this distribution with a Gaussian for each mode under study. All

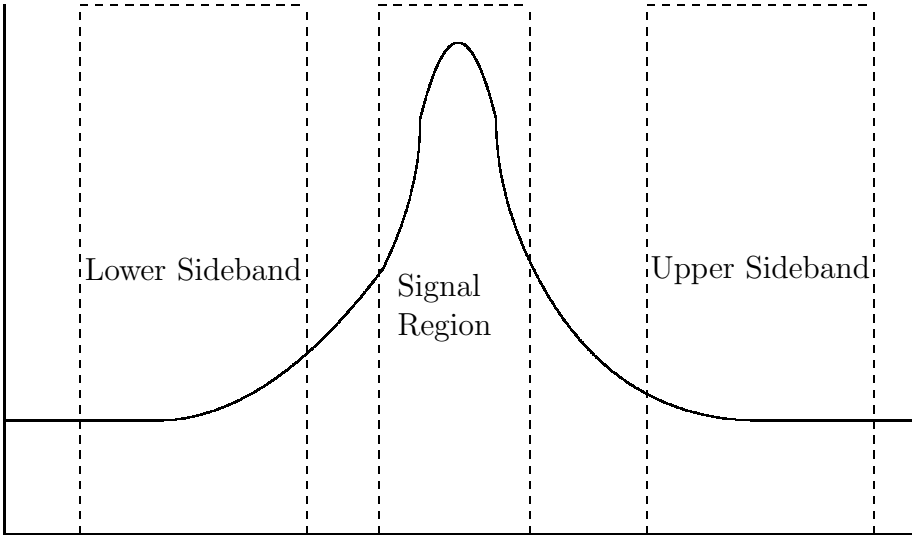

Figure 6.1: An illustration of the definition of a signal region and sideband regions.

Table 6.1: Definition of D^0 invariant mass regions. The signal region is found from the optimisation procedure 5.2.

Mode	Lower sideband region (MeV/c^2)	Signal region (MeV/c^2)	Upper sideband region (MeV/c^2)
$D^0 \to K^-\pi^+$	[1.770, 1.815]	[1.853, 1.877]	[1.915, 1.960]
$D^0 \to K^-\pi^+\pi^0$	[1.770, 1.815]	[1.836, 1.889]	[1.915, 1.960]
$D^0 \to K^-\pi^+\pi^-\pi^+$	[1.770, 1.815]	[1.853, 1.877]	[1.915, 1.960]
$D^0 \to \pi^+\pi^-$	[1.770, 1.815]	[1.853, 1.877]	[1.915, 1.960]
$D^0 \to K^+K^-$	[1.770, 1.815]	[1.853, 1.877]	[1.915, 1.960]
$D^0 \to K^0_S\pi^0$	[1.770, 1.815]	[1.835, 1.895]	[1.915, 1.960]
$D^0 \to K^0_S\phi$	[1.770, 1.815]	[1.853, 1.877]	[1.915, 1.960]
$D^0 \to K^0_S\omega$	[1.770, 1.815]	[1.845, 1.885]	[1.915, 1.960]

modes were found to have a statistically compatible variation (σ) which has been rounded to 25 MeV. The signal region (regions 4, 5 and 6 in Fig 6.2) in ΔE was chosen to be $\pm 3\sigma$ in size with the lower sideband (regions 7, 8 and 9 in Fig 6.2) defined as $-8\sigma < \Delta E < -4\sigma$ and the upper sideband (regions 1, 2 and 3 in Fig 6.2) defined as $4\sigma < \Delta E < 8\sigma$.

The signal region (regions 2, 5 and 8 in in $m_{\rm ES}$ Fig 6.2) is taken to be $5.27 < m_{\rm ES} < 5.30\,{\rm GeV}$. This distribution does not require the definition of sideband regions.

Table 6.2: Definition of ΔE regions.

Lower sideband (MeV/c^2)	Signal (MeV/c^2)	Upper sideband (MeV/c^2)
$-200 < \Delta E < -100$	± 75	$100 < \Delta E < 200$

The three data subsets required to extrapolate the size of the background components from the sideband regions into the signal region are formed

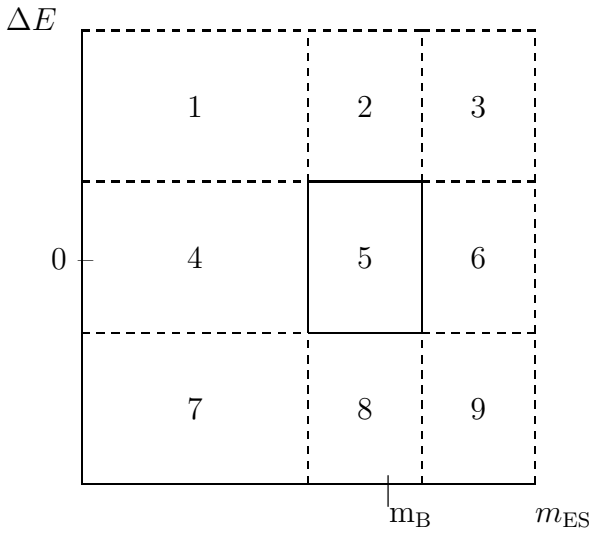

Figure 6.2: Regions of the $m_{\rm ES}$, ΔE plane. Regions 1, 2, 3 and 6, 7, 8 are the ΔE sidebands while region 5 is the signal box.

present. The estimate of the number of events found in the signal region is based upon the analysis of several Monte Carlo samples, one for each decay which contributes to this background, generated in a similar manner to the production of signal Monte Carlo samples.

- **Step 2: Continuum background.** The background from the $e^+e^- \to q\overline{q}$ continuum events is modelled by using events in the ΔE sidebands (regions 1-3 and 7-9 in Fig. 6.2).

- **Step 3: Fake D^0 peaking background.** To estimate the number of events with a final state similar to the signal modes, but no intermediate D^0 present, the continuum background PDF found in step 2 is combined with a Gaussian PDF. The $m_{\rm ES}$ distribution of events in the D^0 invariant mass sidebands is fitted with this composite PDF. The number of events found in the Gaussian PDF can then be extrapolated into the signal region.

- **Step 4: Yield measurement.** The number of signal events is measured for each decay type by fitting a PDF to the $m_{\rm ES}$ distribution of the events contained within the signal data subset. The PDF is constructed by combining

the PDFs that model the continuum and fake D^0 backgrounds with a second Gaussian PDF used to estimate the signal yield. The component due to fake K^{*-} decays is deducted from the result found to give a final yield.

- **Step 5: CP yield measurement.** The CP-odd and CP-even samples can be split into data sets based upon the charge of the reconstructed B meson. These samples are then fitted in the same manner as the yield measurement.

  A background from Non-Resonant decays must be treated separately from the main fit because this background has an unmeasured branching ratio and behaves like signal in $m_{\rm ES}$, ΔE and the invariant mass of the D^0. This background also introduces an additional strong phase. This work is presented in Section 7.4.4.

6.3 Applying the yield estimation strategy to Monte Carlo events

Before applying the fit strategy to data it was validated by studying Monte Carlo events. An advantage of the simulated sample is that it was generated with a known (zero) asymmetry. This means that $\mathcal{A}_\pm$ should be zero, while $\mathcal{R}_\pm$ should be equal to unity.

Another advantage of using Monte Carlo is that the analysis of real data can remain "blind". A blind analysis is one which does not make use of the on-peak data in the signal region until the selection criteria have been chosen and the yield estimation procedure has been created. This is done to ensure that the result is less likely to be biased by changing the selection or fit procedure until the expected results are seen. The use of blind analysis techniques is standard *BABAR* policy.

6.3.1 Estimating the fake K^{*-} background

Based upon the background studies performed in Section 5.6 it is expected that this background will affect the non-CP modes, but that it should not be a significant background for the CP modes.

These misreconstructed events originate from the PID algorithm mistakenly identifying a pion as a kaon. The size of this background is estimated by taking each

mode that was found to contribute to this background in Section 5.6 and applying the full analysis chain to a sample of Monte Carlo events where each event has been produced with one of the B mesons decaying to the background mode. Where no sample was available or where the number of events did not form a significant proportion of the background, the numbers from the background study were used with a conservative 100% uncertainty assigned. Table 6.3 summarises the results of these studies.

Although it is undesirable to rely on a Monte Carlo estimation, rather than using the distributions of the on-peak data sample, it was found to be necessary. Unlike the Fake D^0 background estimated in Section 6.3.3, we could not make use of the sidebands of the invariant mass distribution of the particle being misreconstructed. This was because the large natural width of the K^{*-} did not allow for sufficiently wide sidebands to be defined where we could be confident that they would not be contaminated by signal events.

Table 6.3: The estimated peaking background present due to misreconstructed $B^- \to D^0 X$ events in $185.8\,\mathrm{fb}^{-1}$. Where no pure sample is available or the number of events of a particular mode is small, a conservative 100% error is assumed.

Background Mode	$K^-\pi^+$	$K^-\pi^+\pi^0$	$K^-\pi^+\pi^-\pi^+$
$D^0\ \pi^-$	1.8 ± 0.75	4.0 ± 0.5	0.9 ± 1.05
$D^0\ \rho^-$	1.8 ± 0.75	5.8 ± 0.4	1.8 ± 0.75
$D^0\ a_1^-$	n/a	n/a	2.2 ± 2.2
Other Modes	0.9 ± 0.9	1.3 ± 1.3	4.0 ± 4.0
Total	4.5 ± 1.4	11.2 ± 1.5	8.9 ± 4.7

6.3.2 Accounting for the continuum background

An Argus function, which was first used by the Argus collaboration [24], is used to model the continuum background. This function is defined as:

$$\mathcal{A}(m_{\mathrm{ES}}) \;=\; m_{\mathrm{ES}}\sqrt{1-\left(\frac{m_{\mathrm{ES}}}{c}\right)^2}\,e^{-\eta\left(1-\left(\frac{m_{\mathrm{ES}}}{c}\right)^2\right)}. \tag{6.3}$$

The Argus function has two parameters, the first is the endpoint (c) which is the mass at which the function must go to zero. This reflects the fact that above the mass of the B there is insufficient energy to make heavier particles. The endpoint is calculated as, $\sqrt{s}/2$, where s is the centre-of-mass energy squared. This gives the

endpoint a value of 5.291 GeV.

The Argus shape parameter, denoted by η, affects the curvature of the function. For this parameter it is assumed that all eight decay modes will see a similar continuum background shape. This is not immediately obvious, and so to investigate the assumption Table 6.4 shows the value of the Argus shape parameter for all three mode types and the three data subsets. The values found in the nine possible combinations of these mode types and data subsets show that with a few exceptions the assumption appears valid. To ensure that this assumption is valid on data, Table 6.4 also includes the results of these fits to the on-peak data.

Table 6.4: The value of the Argus shape parameter (η) for the three defined data subsets and three types of D^0 decay. All analysis cuts have been applied with the exception of the D^0 mass cut in the non-CP modes.

Region	non-CP		CP-odd	
Dataset	Monte Carlo	On-Peak	Monte Carlo	On-Peak
Signal	-22.9 ± 3.1	blind	-39.5 ± 11.0	blind
m(D^0) sideband	-16.3 ± 2.8	-27.0 ± 3.1	-18.3 ± 8.8	-22.3 ± 10.1
ΔE sideband	-28.9 ± 3.2	-37.0 ± 2.8	-20.8 ± 6.7	-21.1 ± 7.8

Region		CP-even	
Dataset		Monte Carlo	On-Peak
Signal		-22.9 ± 12.6	blind
m(D^0) sideband		-17.0 ± 10.2	-14.6 ± 9.6
ΔE sideband		-18.9 ± 9.6	-27.3 ± 10.5

The benefit of making this assumption on the shape of the continuum background is that the ΔE sidebands of all eight modes can be treated as a single sample. This leads to a much better statistical precision on the modes where the D^0 is reconstructed decaying to a CP eigenstate, since measurement is dominated by the larger event sample of the non-CP modes.

The final value obtained when fitting all eight modes at once in the ΔE sideband is $\eta = -26.9 \pm 2.9$ for simulated events. A Gaussian is used to account for the effect of events which contain a B meson, but which is not fully reconstructed, leading to a value of ΔE offset from zero. This fit is shown in Fig. 6.3.

6.3.3 Estimating the background due to fake D^0 decays

The next stage is to estimate the size of the peaking background from fake neutral D mesons. This estimate is found by applying all analysis cuts and fitting an Argus

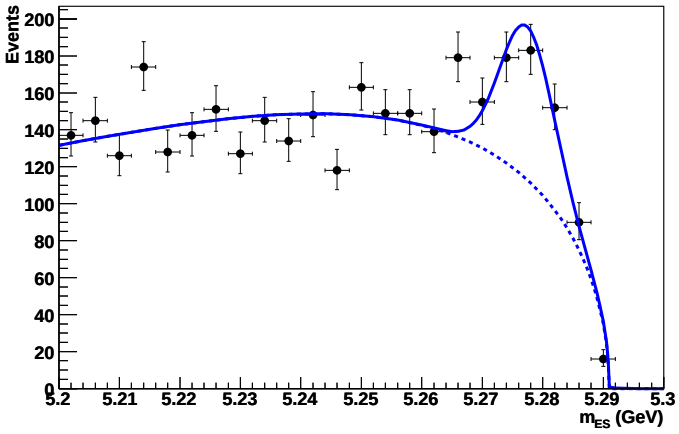

Figure 6.3: An Argus PDF (Dashed line) and a Gaussian PDF are combined to form a complete PDF (solid line) which is used to fit the $m_{\rm ES}$ distribution in the ΔE sidebands of Monte Carlo data. This is done to a data set consisting of all modes in order to fix the Argus shape parameter (η) for future steps in the fit procedure. The peak seen at the B mass is due to background events from B mesons which have not been fully reconstructed and so are in the sidebands of ΔE.

PDF plus a Gaussian PDF to the $m_{\rm ES}$ distribution in the D^0 invariant mass sidebands. The Argus PDF is used to model the continuum background and is fixed as described in Section 6.3.2. The mean and width of the Gaussian PDF, which models the fake D^0 background, are left adjustable.

The number of fake D^0 background events found must be extrapolated into the signal region. This is done by scaling the number of events found by the ratio $P_{\rm Sig}/P_{\rm Side}$ where $P_{\rm Sig}$ is the signal region phase-space and $P_{\rm Side}$ is the upper and lower sideband phase-space of the D^0 invariant mass.

The use of this method is based upon the assumption that there is a signal peak sitting upon a broad continuum of fake D^0 candidates in the D^0 invariant mass distribution. This assumption appears valid as shown in Fig. 6.4.

An example fit is shown in Fig. 6.5 for the $K^-\pi^+\pi^0$ mode. Each mode must be fitted separately because the ratio of the phase-space of the signal region to the sideband region varies.

Only the non-CP modes were found to suffer from this background. The total number of events found in the D^0 invariant mass sidebands of the non-CP modes after the required scaling was 13.8 ± 5.7.

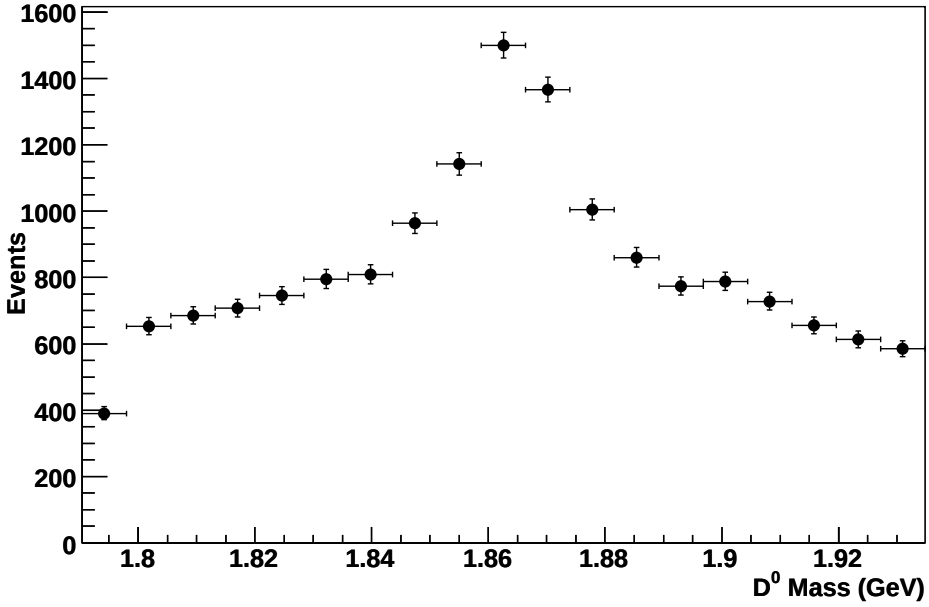

Figure 6.4: The D^0 invariant mass distribution on Monte Carlo data for non-CP modes where the D^0 decays to $K^+\,\pi^-$, $K^+\,\pi^-\,\pi^0$ and $K^+\,\pi^-\,\pi^+\,\pi^-$. All analysis cuts with the exception of ΔE and $m_{\rm ES}$ have been applied. The lowest bin shows a large drop because it extends beyond the point at which a preselection cut is applied.

6.3.4 Signal yield measurement

Before attempting to measure the yields where the D^0's CP eigenstate state is identified by its decay to a CP-even or a CP-odd mode, the yield of D^0's identified as being a non-CP eigenstate is found.

Table 6.5: The parameters used in the fit to simulated non-CP events. A value of "Free" indicates that this parameter is allowed to float in the fit performed at this stage.

PDF	Parameter	Value
Argus	η	-26.9
	endpoint	5.291 GeV/c^2
	$N_{\rm events}$	Free
Peaking Gauss	Mean	5.2789 GeV/c^2
	Width	Free
	$N_{\rm events}$	13.8
Signal Gauss	Mean	Free
	Width	Free
	$N_{\rm events}$	Free

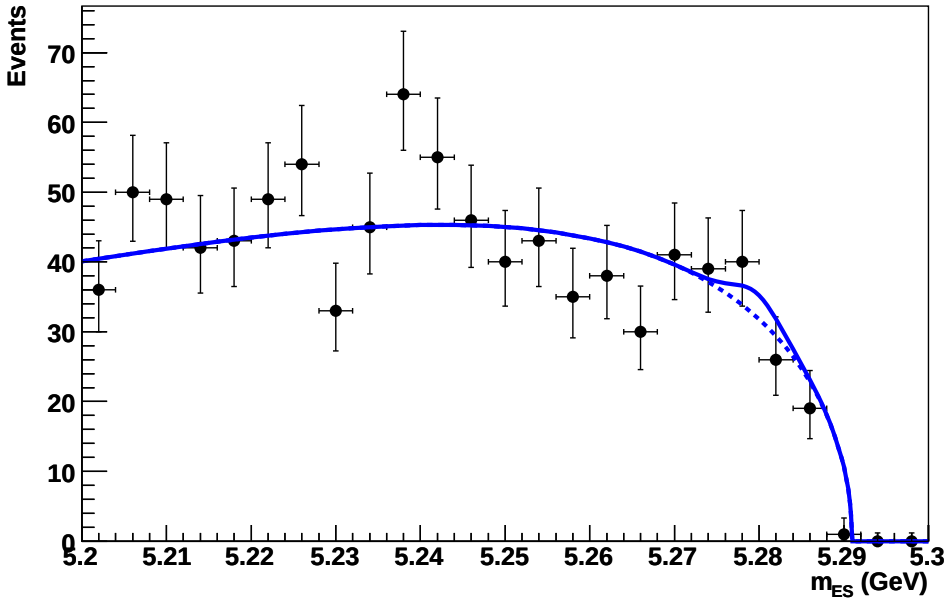

Figure 6.5: Fit to the $m_{\rm ES}$ distribution in the D^0 mass sidebands for the $K^-\pi^+\pi^0$ mode. Each mode is fitted separately because of the differing phase space weighting required. The black marks are the Monte Carlo data points, the solid blue line is the combined PDF and the dashed line is the Argus PDF only.

The fit to the $m_{\rm ES}$ distribution in the signal region is performed by combining an Argus PDF and two Gaussian PDFs. The first Gaussian PDF is fixed based on the earlier fit to account for any background due to fake D^0s. The second Gaussian PDF is used to estimate the signal yield. Where the number of fake D^0 background events was found to be consistent with zero, the PDF used to account for this background is omitted. The parameters of each of these PDFs are summarised in Table 6.5. The mean of the peaking background is set to the mass of the B meson to improve the reliability of the fit.

The fit to the non-CP modes is shown in Fig. 6.6. The results of these fits, taking into account the background events that contain a fake K^{*-} are shown in Table 6.6.

It is noted that the yields found with the fit are consistent with those found on the signal Monte Carlo for the efficiency calculation.

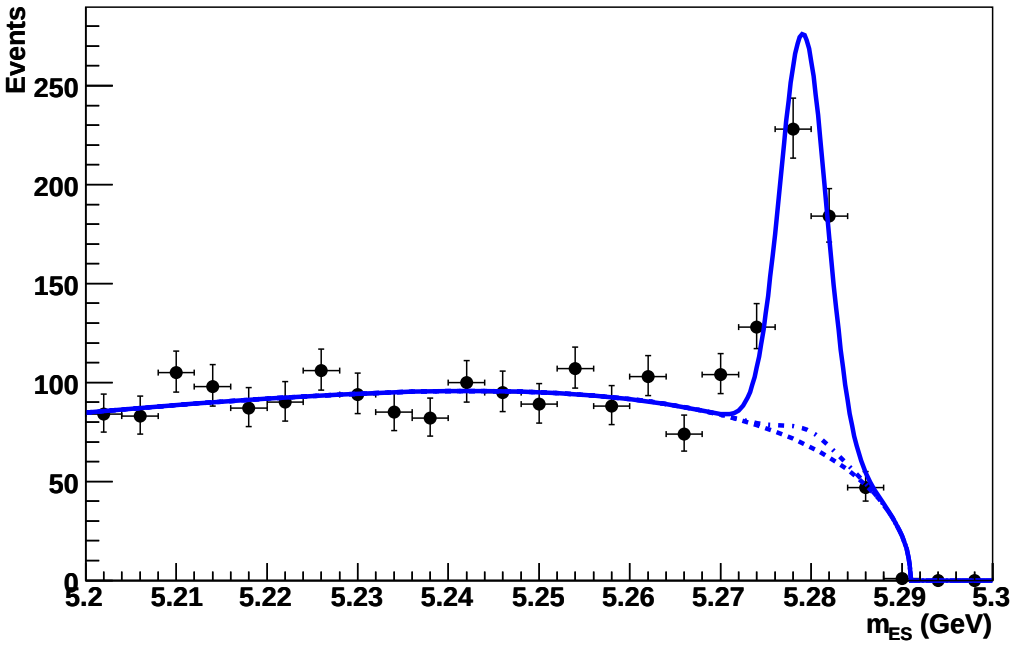

Figure 6.6: Fit to the $m_{\rm ES}$ distribution on Monte Carlo data with all other analysis cuts applied for the non-CP modes where the D^0 decays to $K^+\ \pi^-$, $K^+\ \pi^-\ \pi^0$ and $K^+\ \pi^-\ \pi^+\ \pi^-$. The black marks are the data points, the solid blue line is the combined PDF and the dashed lines are the Argus PDF with the peaking background Gaussian on top.

Table 6.6: The signal yield extracted for each type of D^0 decay on simulated events. The full analysis chain is applied with a fit in $m_{\rm ES}$ as described in the text.

	non-CP	CP-even	CP-odd
Yield	321.8 ± 25.0	12.4 ± 4.3	16.5±6.9
D^0 X background	24.6 ± 5.3	N/A	N/A
Total	297.2 ± 25.6	12.4 ± 4.3	16.5±6.9

6.3.5 CP yield measurement

Each of the data sets which contain D^0's decaying to states which identify the D^0 as having been a CP-odd or CP-even eigenstate are split into negative and positive subsets. The method used to measure the yield in section 6.3.4 is used to measure the number of signal events in each of the data subsets.

Because these data sets have less events, the signal mean and width must be fixed to achieve an accurate fit result. The mean is fixed to the mass of the B meson while the width is set to the width measured on the non-CP modes of $2.6 \pm 0.2\,\mathrm{MeV}/c^2$.

Table 6.7 summarises the values of the fit parameters used. Figure 6.7 shows the fits to measure the signal yields from both charge subsets of the CP-even and CP-odd decay modes.

Table 6.7: The parameters used in the fit to extract the CP mode yields from Monte Carlo. A value of "Free" indicates that this parameter is allowed to float at this stage.

PDF	Parameter	Value
Argus	η	-26.9 ± 2.9
	endpoint	5.291 GeV/c^2
	N_{events}	Free
Signal Gauss	Mean	5.2789 GeV/c^2
	Width	0.0026 GeV/c^2
	N_{events}	Free

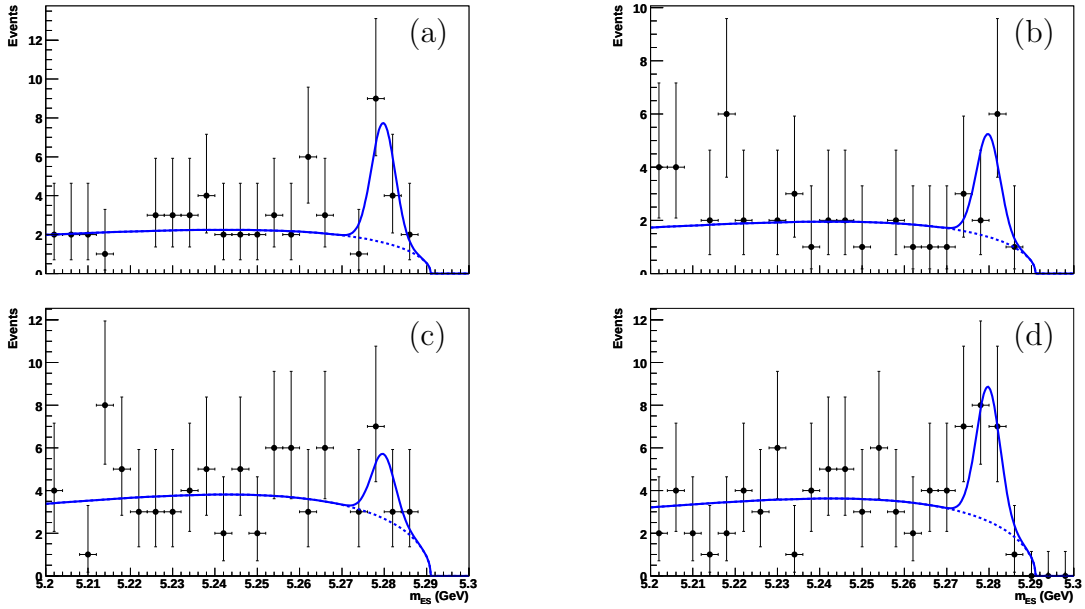

Figure 6.7: Fit to the m_{ES} distribution with all other analysis cuts applied. (a) Shows the yield extraction for positively charged CP-even events, (b) negatively charged CP-even events, (c) positively charge CP-odd events and (d) negatively charge CP-odd events. The black marks are the Monte Carlo data points, the solid blue line is the combined PDF and the dashed line is the Argus PDF only.

The results found in the CP-even data subsets were $N^{+}_{\text{CP-even}} = 10.8 \pm 3.9$ and $N^{-}_{\text{CP-even}} = 6.8 \pm 3.3$. The CP-odd results were $N^{+}_{\text{CP-odd}} = 5.3 \pm 3.5$ and $N^{-}_{\text{CP-odd}} = 11.0 \pm 4.4$. These results are compatible with the signal Monte Carlo results found in Section 5.4.

6.4 Validation of the yield estimation strategy with toy Monte Carlo experiments

Toy Monte Carlo is the term used for a simulated data set which is not the result of a simulation with the full analysis chain applied. Instead it is based upon a simple model using just the results obtained from another experiment or more detailed simulation. As such, toy Monte Carlo can be used to study the robustness of the yield estimation strategy by simulating several hundred experiments quickly and observing the variation in the results found.

6.4.1 Creating the toy Monte Carlo

The toy Monte Carlo used by this study with generated with a PDF created by combining the Argus PDF and two Gaussian PDFs in section 6.3.5. The parameters were fixed to those in Table 6.8 which were found when the three PDFs were fitted in the preceding Monte Carlo results section. With the parameters set, 200 toy experiments are generated. For each experiment, the fits described in the yield measurement sections are applied with all parameters set to the same values. This results in 200 toy measurements of each of the five event yields under study.

6.4.2 Validating the toy Monte Carlo

To test the toy Monte Carlo, a set of experiments was created where the number of events created per experiment was large and the shape of the distributions were well defined. The distributions resulting from this simulation were then fitted with the PDFs used to create the data, but with several parameters no longer constrained to the well defined input values. The results obtained were consistent with the values used to create the sample of toy experiments.

With the toy experiment production working, well defined toy Monte Carlo based on the results of Sections 6.3.4 and 6.3.5 was created. Figure 6.8 shows the distributions of the non-CP generated experiments and the experiments created to simulate the low statistics CP-odd modes. The left-hand side of this figure shows the yield found when applying the fits to each of the toy experiments. In the plots of the fitted number of events from each toy experiment it can be seen that the central value of the plots are within 1σ of those that were input into the toy Monte Carlo

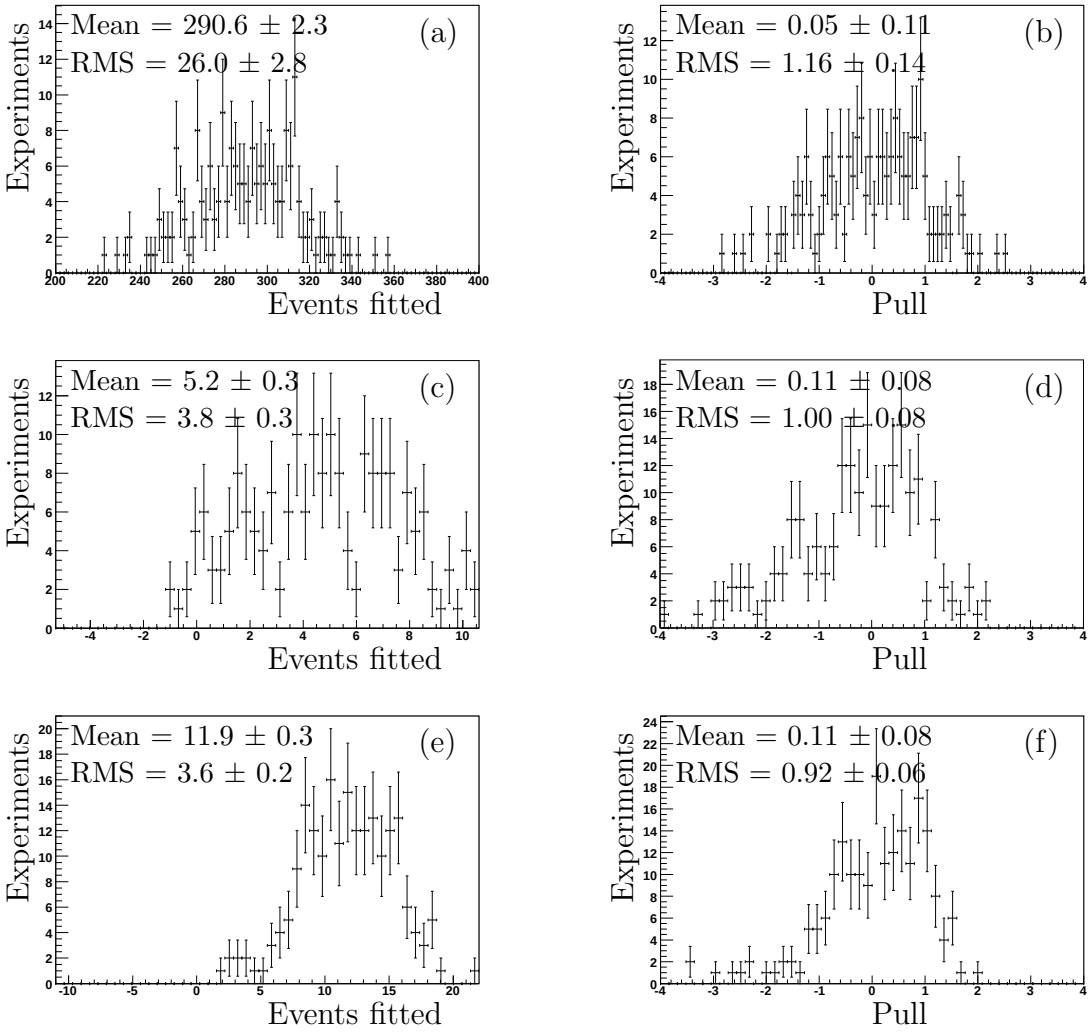

Figure 6.8: Toy Monte Carlo validation plots. The plots on the left-hand side are the fitted number of events found for (a) the non-CP yield, (c) the positive sample of CP-odd modes and (e) the negative sample of CP-odd modes. The plots on the right-hand side (b, d and f) are the pull distributions of these experiments.

Table 6.8: The PDFs and parameters used to create the toy Monte Carlo. The CP data sets do not suffer from a peaking background so the values are not applicable (N/A). The number of events specified are those required in the signal region.

PDF	Parameter	non-CP	CP-even +	CP-even-
Argus	η	-26.9		
	endpoint	$5.291\,\mathrm{GeV}/c^2$		
	N_{events}	362	7.4	6.4
Peaking Gauss	Mean	$5.2789\,\mathrm{GeV}/c^2$	N/A	N/A
	Width	$2.6\,\mathrm{MeV}/c^2$	N/A	N/A
	N_{events}	13.8	N/A	N/A
Signal Gauss	Mean	$5.2789\,\mathrm{GeV}/c^2$		
	Width	$2.6\,\mathrm{MeV}/c^2$		
	N_{events}	297.2	10.8	6.8
PDF	Parameter	CP-odd +	CP-odd-	
Argus	η	-26.9		
	endpoint	$5.291\,\mathrm{GeV}/c^2$		
	N_{events}	12.6	12.0	
Signal Gauss	Mean	$5.2789\,\mathrm{GeV}/c^2$		
	Width	$2.6\,\mathrm{MeV}/c^2$		
	N_{events}	5.3	11.0	

generation.

On the right-hand side of Fig. 6.8 is the pull, defined as $p = N_{\mathrm{Obs}} - N_{\mathrm{Exp}}/\sigma_{\mathrm{Obs}}$, where N_{Obs} is the observed number of signal events, σ_{Obs} is the error on N_{Obs} reported by the fit and N_{Exp} is the expected number of signal events, which in this scenario is the number of signal events generated in each toy experiment.

The pull plot is useful because it shows whether the number of events measured is being systematically overestimated, a positive mean value, or underestimated, a negative mean value. Ideally the pull will be centred on zero. The pull distributions in Figure 6.8 are all centred around 0 to within 1.5σ . This shows that fit used by this analysis does not suffer from a large systematic bias in the estimation of the number of signal events. Within statistical uncertainty the variance of the pull is found to equal one, as expected of a model that is working correctly.

6.5 Applying the yield estimation strategy to data

The toy studies showed that the fit procedure makes a good estimate of the number of signal events in a data set. With the fit procedure validated the analysis was

permitted to unblind, that is, the B Reconstruction Analysis Working Group of *BABAR* gave permission for the analysis to look at the on-peak data in the signal region. This meant that the yield estimation strategy could now be applied to the on-peak data set.

6.5.1 Estimating the fake K^{*-} background

The number of background events in this category is found by taking the estimate based on Monte Carlo from Section 6.3.1 above after efficiency corrections have been applied. These corrections compensate for the fact that Monte Carlo is not a perfect simulation of real data. The efficiency corrections are covered in detail in Section 7.2.

After all corrections the background that remains for the non-CP modes is found to be 23.1 ± 6.4 events. The larger relative error in comparison with the uncorrected value found on Monte Carlo is due to the uncertainty in the efficiency correction.

6.5.2 Accounting for the continuum background

The assumption that the Argus shape parameter can be fixed to a single value for all modes has already been shown to be valid in Section 6.3.2. Figure 6.9 shows the fit of the Argus PDF plus Gaussian PDF to the data sample.

The value of the Argus shape parameter found was $\eta = -35.1 \pm 2.80$. This compares to the value of $\eta = -26.9 \pm 2.85$ found on Monte Carlo. This is a 2σ difference. This difference between data and Monte Carlo is treated as a systematic error in Section 7.4.1.

6.5.3 Estimating the background due to fake D^0 decays

All analysis cuts are applied and an Argus PDF plus a Gaussian PDF is fitted to the $m_{\rm ES}$ distribution in the D^0 mass sidebands. The parameters of the Argus PDF are fixed to the values found in Section 6.5.2 while the parameters of the Gaussian PDF are left free to float.

An example fit to events in the $D^0 \to K^-\pi^+\pi^0$ mode is shown in Fig. 6.10. Each D^0 mode must be fitted separately because of the differing relative sizes of the signal and sideband phase-spaces. As with the Monte Carlo, the non-CP modes were the only ones found to suffer from this source of background.

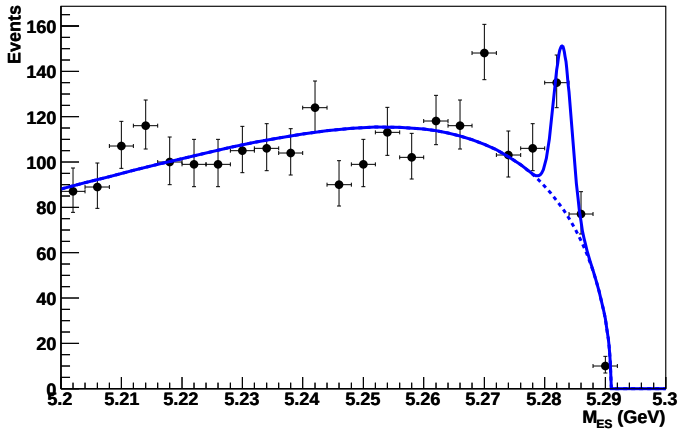

Figure 6.9: Fit to the $m_{\rm ES}$ distribution in the ΔE sidebands is applied to all eight modes on OnPeak data in order to fix the Argus shape parameter (η) for future steps in the fit procedure. An Argus PDF (Dashed line) and a Gaussian PDF are combined to form a complete PDF (solid line) which is used to fit the $m_{\rm ES}$ distribution in the ΔE sidebands. This is done to a data set consisting of all modes in order to fix the Argus shape parameter (η) for future steps in the fit procedure. The peak seen at the B mass is due to background events from B mesons which have not been fully reconstructed and so are in the sidebands of ΔE.

The number of events found in the D^0 invariant mass sidebands, once the different phase-space of the sidebands relative to signal region has been taken into account was 4.8 ± 3.5.

6.5.4 Signal yield measurement

The fit to find the yield of events where the D^0 is identified decaying to a non-CP state is shown in Fig. 6.11. The parameters used in this fit are defined in Table 6.9. The results of this fit and the fit to the CP-even and CP-odd modes are shown in Table 6.10.

There is a lower yield in comparison with the Monte Carlo results. This is shown in the Section 7.2 to be in part due to a number of efficiency corrections that must be applied to make a direct comparison. Indeed, because this analysis does not attempt to measure a branching ratio, the corrections shown are insufficient for making an accurate direct comparison. The recent branching ratio measurement by *BABAR* [14] suggests that the branching ratio for $B^- \to D^0 K^{*-}$ may be 19% lower than that used in the Monte Carlo of this analysis. If this figure is used to scale the expected yield, it is found that the yield on data is now compatible with Monte Carlo.

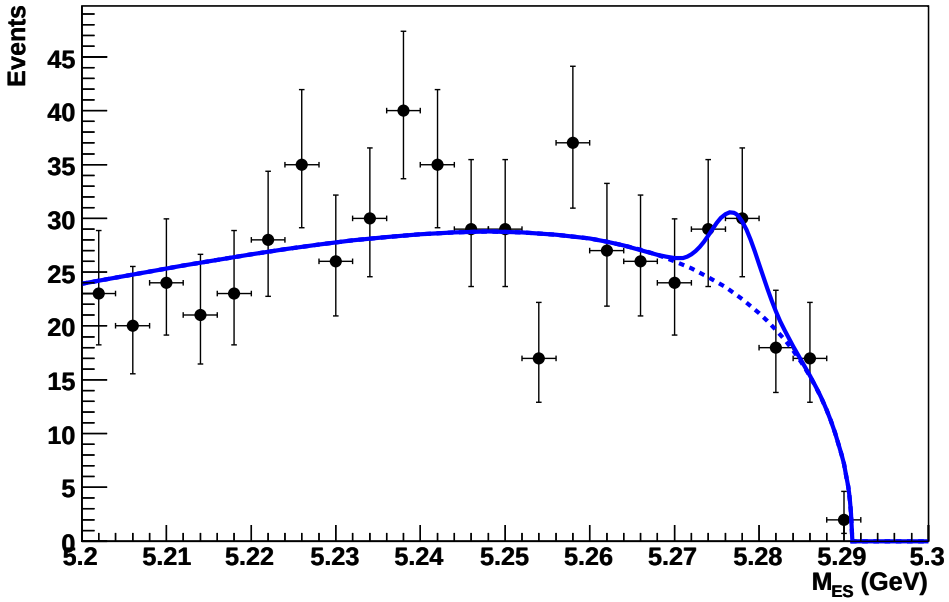

Figure 6.10: Fit to the $m_{\rm ES}$ distribution in the D^0 mass sidebands for the $K^-\pi^+\pi^0$ mode. The black marks are the OnPeak data points, the solid blue line is the combined PDF and the dashed line is the Argus PDF only.

Table 6.9: The parameters used in the fit to extract the signal yield from data. A value of "Free" indicates that this parameter is allowed to float in the fit performed at this stage.

PDF	Parameter	Value
Argus	η	-35.1
	endpoint	5.291 GeV/c^2
	$N_{\rm events}$	Free
Peaking Gauss	Mean	5.2789 GeV/c^2
	Width	Free
	$N_{\rm events}$	4.8
Signal Gauss	Mean	Free
	Width	Free
	$N_{\rm events}$	Free

Table 6.10: The signal yield found in data for the three types of D^0 decay.

	non-CP	CP-odd	CP-even
Yield	218.2 ± 21.1	0.6 ± 6.6	12.5 ± 4.5
D^0 X background	23.4 ± 6.1	N/A	N/A
Final Yield	195.1 ± 22.1	0.6 ± 6.6	12.5 ± 4.5

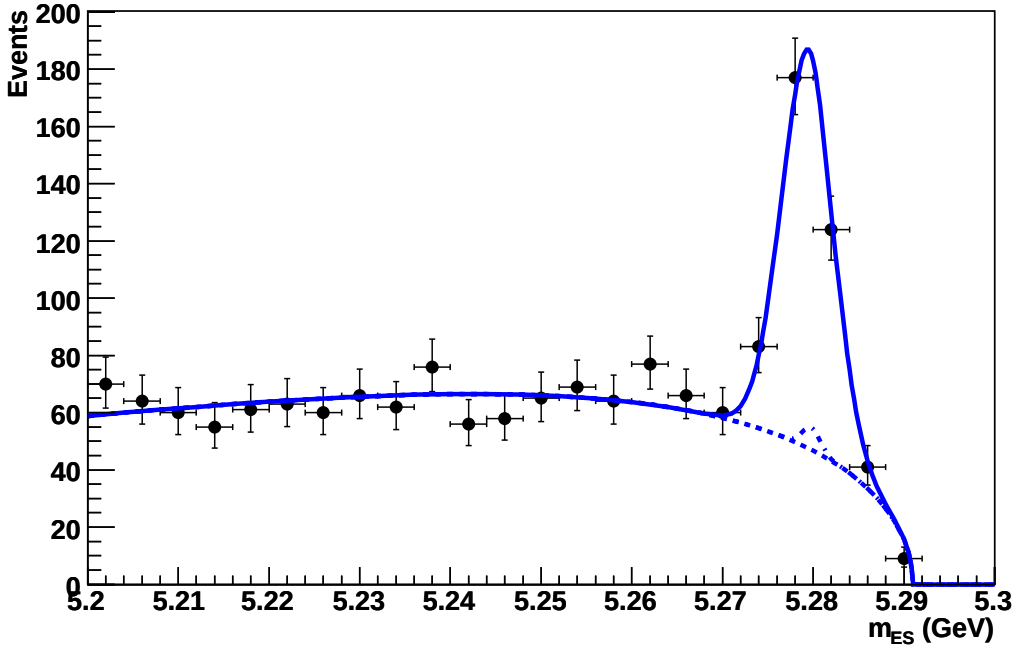

Figure 6.11: Fit to the $m_{\rm ES}$ distribution with all other analysis cuts applied for the non-CP modes where the D^0 decays to $K^+\,\pi^-$, $K^+\,\pi^-\,\pi^0$ and $K^+\,\pi^-\,\pi^+\,\pi^-$. The black marks are the OnPeak data points, the solid blue line is the combined PDF and the dashed lines are the Argus PDF with the peaking background Gaussian on top.

6.5.5 CP yield measurement

The measurement of the four yields, where the D^0's CP eigenstate is identified as odd or even and the charge is positive or negative, is achieved by splitting the data sample based on the charge of the reconstructed B meson. The same fit as that used to measure the yield in the data set that is not split on charge is applied. Because of the lower number of events available the signal Gaussian's width was fixed to $0.0028\,\mathrm{GeV}/c^2$ and its mean was fixed to the mass of the B meson. The value used to fix the width was the measured width of the signal Gaussian in the non-CP modes. The parameters used are shown in Table 6.11 which summarises the values of the fit parameters used.

The fits to each of the CP charge subsets is shown in Fig. 6.12. Table 6.13 summarises the yields measured.

The last result was found with a biased fit which was constrained to have a minimum value of 0. With an unbiased fit the yield measured was -2.2 $\pm$ 3.6. The

Table 6.11: The parameters used in the fit to extract the CP mode signal yield from Data. A value of "Free" indicates that this parameter is allowed to float at this stage.

PDF	Parameter	Value
Argus	η	-35.1
	endpoint	5.291 GeV/c^2
	N_{events}	Free
Signal Gauss	Mean	5.279 GeV/c^2
	Width	0.0028 GeV/c^2
	N_{events}	Free

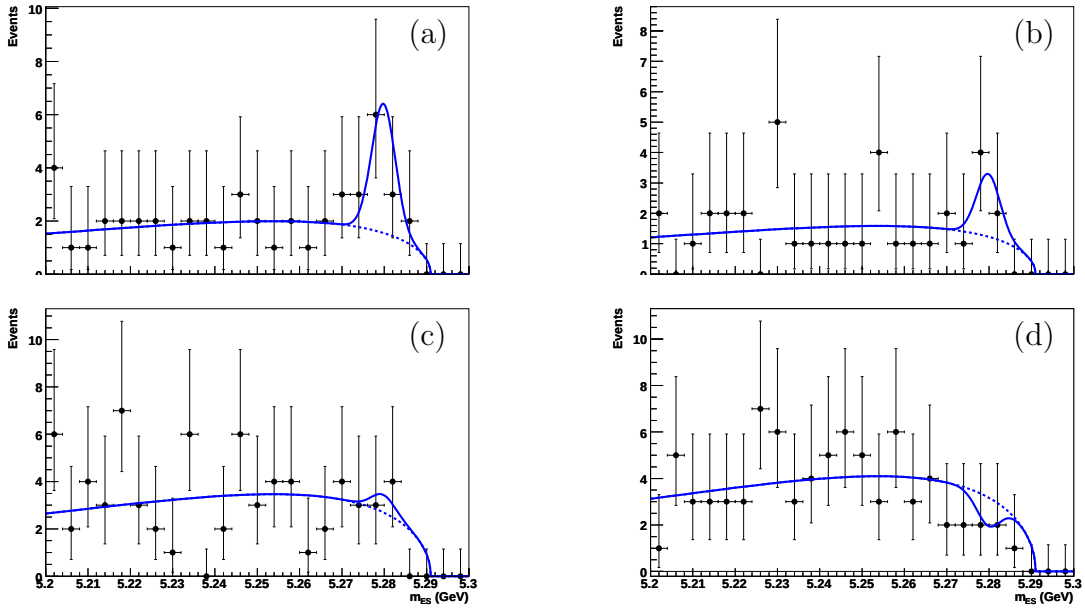

Figure 6.12: Fit to the m_{ES} distribution on data with all other analysis cuts applied. (a) Shows the yield extraction for positively charged CP-even events, (b) negatively charged CP-even events, (c) positively charge CP-odd events and (d) negatively charge CP-odd events. The black marks are the OnPeak data points, the solid blue line is the combined PDF and the dashed line is the Argus PDF only.

Table 6.12: The yields measured when the CP-even and CP-odd data is split into positive and negative samples based upon the charge of the reconstructed B meson.

Data sample	# events seen
CP-even Positive	8.5 ± 3.6
CP-even Negative	3.6 ± 2.7
CP-odd Positive	1.3 ± 2.0
CP-odd Negative	0.0 ± 1.7

unbiased fit is given in Fig 6.12.

6.5.6 Summary

In this chapter a yield estimation strategy was developed with Monte Carlo data. Toy Monte Carlo experiments were created to test the robustness of the fits used. With satisfactory results from these tests the analysis was approved to "unblind" meaning that the yield estimation strategy could be applied to real data in the signal region. This resulted in several yield measurements which will be used in the next chapter to calculate $\mathcal{A}_{\pm}$ and $\mathcal{R}_{\pm}$.

Table 6.13: A summary of the yields measured on data required to calculate $\mathcal{R}_{\pm}$ and $\mathcal{A}_{\pm}$. The CP modes have been split into positive and negative subsets.

Data sample	# events seen
CP-even positive	8.5 ± 3.6
CP-even negative	3.6 ± 2.7
CP-odd positive	1.3 ± 2.0
CP-odd negative	0.0 ± 1.7
non-CP	195.1 ± 22.1

Chapter 7

Results

This chapter presents the calculation of the GLW quantities $\mathcal{A}_+$, $\mathcal{A}_-$, $\mathcal{R}_+$, and $\mathcal{R}_-$ using the yields measured in the previous chapter. First it is shown how the yields measured relate to the decay rates which form $\mathcal{A}_\pm$ and $\mathcal{R}_\pm$. A number of studies are performed to calculate a set of further efficiency corrections which are required to enable the calculation of $\mathcal{R}_\pm$. The GLW quantities are calculated and sources of potential systematic error are considered.

7.1 Measuring the GLW quantities $\mathcal{A}_\pm$ and $\mathcal{R}_\pm$

It was shown in Chapter 2 that γ could be calculated by measuring the decay rates of several $B^- \to D^0 K^{*-}$ modes:

$$\mathcal{A}_\pm = \frac{\Gamma(B^- \to D^0_\pm K^{*-}) - \Gamma(B^+ \to \overline{D}^0_\pm K^{*+})}{\Gamma(B^- \to D^0_\pm K^{*-}) + \Gamma(B^+ \to \overline{D}^0_\pm K^{*+})}; \tag{7.1}$$

$$\mathcal{R}_\pm = \frac{[\Gamma(B^- \to D^0_\pm K^{*-}) + \Gamma(B^+ \to \overline{D}^0_\pm K^{*+})]}{\Gamma(B^- \to D^0 K^{*-}) + \Gamma(B^+ \to \overline{D}^0 K^{*+})}. \tag{7.2}$$

However, this analysis has measured several yields: $N_{\mathrm{non-CP}}$, $N^+_{\mathrm{CP-even}}$, $N^-_{\mathrm{CP-even}}$, $N^+_{\mathrm{CP-odd}}$ and $N^-_{\mathrm{CP-odd}}$. In order to measure $\mathcal{A}_\pm$ and $\mathcal{R}_\pm$ it must be shown how these yields relate to the decay rates.

A partial decay rate Γ_i is related to a branching ratio by

$$\mathcal{B}(B \to i) \;=\; \frac{\Gamma_i}{\Gamma_{\rm tot}} \tag{7.3}$$

and a branching ratio can in turn be found by

$$\mathcal{B}(B \to i) \;=\; \frac{N}{\epsilon_i \times N_B}. \tag{7.4}$$

In this equation N is the number of signal events observed and N_B is the total number of B mesons produced at the interaction region of the detector. The ϵ term is an efficiency correction. This is required because the *BABAR* detector is unable to detect and reconstruct every signal event. Because the total decay rate, $\Gamma_{\rm tot}$, and N_B are constants for all modes under study, they can be neglected in the ratio of branching ratios. Therefore we can write,

$$\Gamma_i = \;\; \mathcal{B}(B \to i) \propto \;\; \frac{N}{\epsilon}. \tag{7.5}$$

The branching ratios measured in this analysis can therefore be written as

$$\mathcal{B}(B^- \to D^0 K^{*-}) \times \mathcal{B}(D^0 \to i) \;\; \propto \;\; \frac{N}{\epsilon}. \tag{7.6}$$

The term for the branching ratio of the D^0 occurs because the D^0 is reconstructed in order to determine its CP eigenstate. Any CP violation, however, arises from the $B^- \to D^0 K^{*-}$ decay.

The efficiency correction ϵ requires a further correction (C) due to the simulation of the detectors response being imperfect. For convenience, the efficiency corrections and the factor accounting for the D^0 branching ratio are combined into a quantity, ω, where the value of ω for the $i^{\rm th}$ mode is given by,

$$\omega^i \;\; = \;\; \mathcal{B}(D^0 \to i) \times \epsilon_i \times C_i. \tag{7.7}$$

Because the event yields measured have been combined based upon the CP eigenstate of the D^0 the value of ω is found by simply adding the value of ω for each

contributing mode, i.e.,

$$\omega_{\text{non}-\text{CP}} = \omega_{\text{K}\pi} + \omega_{\text{K}\pi\pi^0} + \omega_{\text{K}\pi\pi\pi}. \tag{7.8}$$

It is now possible to rewrite $\mathcal{A}_\pm$ and $\mathcal{R}_\pm$ in terms of the measured yields,

$$\mathcal{A}_+ = \frac{\frac{N^+_{\text{CP}-\text{even}}}{\omega_{\text{CP}-\text{even}}} - \frac{N^-_{\text{CP}-\text{even}}}{\omega_{\text{CP}-\text{even}}}}{\frac{N^+_{\text{CP}-\text{even}}}{\omega_{\text{CP}-\text{even}}} + \frac{N^-_{\text{CP}-\text{even}}}{\omega_{\text{CP}-\text{even}}}}. \tag{7.9}$$

The subscript indicates the CP eigenstate of the D^0 meson and the superscript indicates the charge of the reconstructed B meson. The $\omega_{\text{CP}-\text{even}}$ factors cancel giving,

$$\mathcal{A}_+ = \frac{N^-_{\text{CP}-\text{even}} - N^+_{\text{CP}-\text{even}}}{N^-_{\text{CP}-\text{even}} + N^+_{\text{CP}-\text{even}}}. \tag{7.10}$$

For $\mathcal{R}_\pm$ the efficiencies do not cancel. This means that, for example, $\mathcal{R}_+$ is given by

$$\mathcal{R}_+ = \frac{N^-_{\text{CP}-\text{even}} + N^+_{\text{CP}-\text{even}}}{N^\pm_{\text{non}-\text{CP}}} . \frac{\omega_{\text{non}-\text{CP}}}{\omega_{\text{CP}-\text{even}}}, \tag{7.11}$$

To calculate $\mathcal{R}_+$ therefore, we must find the value of C for each mode. These further efficiency corrections are studied in the next section.

7.2 Further efficiency corrections

In the previous section it was shown that several further efficiency corrections must be applied to the reconstruction efficiency in order to account for differences in selection efficiency between real data and Monte Carlo.

Most of the corrections related to the selection criteria cancel. An example of this is the efficiency correction applied to the Particle Identification (PID) used to select the kaon from the K^{*-} decay. The correction that would need to be applied is the same for all modes because all modes select this kaon in the same way. By making use of these cancellations, the analysis avoids the systematic error associated

with each cancelling correction.

The selection effects which do not cancel in the measurement of $\mathcal{R}_+$ are the cuts applied to the D^0 helicity angle of the CP-even modes and the $m_{K^-\pi^0\pi^+}$ veto used in the $D^0 \to \pi^+\pi^-$ mode. No systematic correction has been calculated for these cuts because any error is expected to be small in comparison to the statistical and other systematic errors. The related analysis measuring the $K^{*-} \to K^0_S\pi^-$ decays provides evidence that these effects should be small [15].

Due to the large statistical error that affects the measurement of $\mathcal{R}_-$, the effect of these further corrections will have a minimal effect on the accuracy of the measurement. For this reason the corrections required due to the use of PID and the reconstruction of the ϕ and ω are neglected. Similarly, rather than apply a specific K^0_S reconstruction efficiency correction, a more approximate measure based on the charged tracks of the daughters of the K^0_S is used.

The studies performed that follow find further efficiency corrections for the tracking, particle identification and π^0 identification algorithms. Each efficiency correction in this section is recorded in Table 7.1 for each mode under study.

7.2.1 Tracking reconstruction efficiency corrections

Standard *BABAR* procedures [25] are used to find the correction that must be applied to the reconstruction of charged tracks. These corrections are based on a sample of $e^+e^- \to \tau^+\tau^-$ events where one τ is reconstructed decaying to a muon or an electron (e.g. $\tau^- \to e^-\bar{\nu}_e\nu_\tau$). This cleanly identifies the τ pair and dictates the charge of the second τ. The second τ in the event is then reconstructed decaying to one of two final states, $\rho^0 h^\pm \nu_\tau$ or $\pi^\pm\pi^\mp h^\pm\nu_\tau$, where h is either a pion or a kaon. The event must only contain three or five charged tracks and have a combined charge of -1, 0 or +1.

Because the τ must decay to an odd number of charged tracks to conserve charge, it is easy to determine the reconstruction efficiency by measuring our ability to reconstruct the hadron (h). The high $e^+e^- \to \tau^+\tau^-$ cross-section and large branching ratios involved allow the correction to be determined with a high statistical precision.

The tracking efficiency correction found by this method is applied on a per track basis. Where a "loose" track has been used the simulated event efficiency must be multiplied by 0.9975, i.e. a 0.25% correction. Where a "tight" track has been used, the multiplication factor is 0.9950, a 0.5% correction. If several tracks are used in

the reconstruction, the correction is found by multiplying the individual percentage corrections. The associated systematic error is 1.2% per track if there are less than five tracks in the event. If there are five or more tracks the systematic error is 1.4% per track. This larger error is due to the greater effect of the multiplicity on selecting the correct track. The efficiency correction associated with the first three uses of track selection criteria cancel because each mode uses these criteria at least three times. This cancellation is on the same basis as explained above because the efficiency correction will cancel when the GLW decay rate ratios are calculated. For the purposes of systematic error calculation, the increased systematic is still assigned where five or more uses of the charged track selection criteria have been used.

7.2.2 Particle identification efficiency corrections

The particle identification (PID) correction must be applied wherever the standard *BABAR* PID algorithms have been used. This analysis makes use of these algorithms for selecting the kaons from the K^{*-} and D^0 decays as well as the pions from the D^0 in the $D^0 \to \pi^+\pi^-$ mode.

The PID efficiency requires the full analysis chain to be performed on signal simulated events with the correction code turned on. The difference in the efficiency with and without the corrections applied gives the relevant correction needed.

The correction code is not applied to all simulated event samples because the time required to process each event is increased by a factor of three which would have required an additional four months of data processing. Table 7.1 shows the corrected efficiency with just kaon corrections applied, just pion corrections applied, and finally with both kaon and pion corrections applied. It can be seen that the correction needed for the pions from the $D^0 \to \pi^+\pi^-$ mode is 1.00. This correction value is not unusual, however the systematic error must still be taken into account because there is an uncertainty on this measurement.

In common with standard *BABAR* practice a systematic of 2% per use of PID is assigned to these corrections. No cancellation of efficiency corrections can be made because it is difficult to disentangle the effect of a single incidence of applying these criteria from the effect of all applications.

Table 7.1: The raw efficiency, $\epsilon_{\rm raw}$, is found before any corrections are applied. The corrections for kaon and pion particle identification are presented both when applied separately and together. Corrections for the use of π^0's and charged tracks are also found. The final row presents the fully corrected efficiency where all these factors have been accounted for. As discussed in the text, no PID correction is applied to the CP-odd modes due to the very large statistical errors.

	$K^-\pi^+$	$K^-\pi^+\pi^0$	$K^-\pi^+\pi^-\pi^+$
$\epsilon_{\rm raw}$	5.4 ± 0.1%	2.6 ± 0.1 %	3.0 ± 0.1 %
$\epsilon_{\rm corrected}$ (K PID only)	0.9555±0.0400	0.9592±0.0400	0.9463±0.0400
$\epsilon_{\rm corrected}$ (π PID only)	N/A	N/A	N/A
(A)$\epsilon_{\rm corrected}$ (K and π PID)	0.9555±0.0400	0.9592±0.0400	0.9463±0.0400
(B) π^0 (D^0) correction	N/A	0.9683±0.0300	N/A
(C) Tracking correction	cancels	cancels	0.9950±0.0280%
Total Correction (A× B× C)	0.9555 ± 0.0400	0.9288 ± 0.0675	0.9368 ± 0.0623
Efficiency after corrections	5.14 ± 0.32%	2.43 ± 0.25%	2.85 ± 0.29 %
	$K^0_S\pi^0$	$K^0_S\phi$	$K^0_S\omega$
$\epsilon_{\rm raw}$	0.72 ± 0.04%	3.33 ± 0.10 %	1.06 ± 0.07 %
(A) π^0 (D^0) correction	0.9683±0.0300	N/A	N/A
(B) Tracking correction	cancels	0.9975 ± 0.012	0.9950 ±0.0280%
Total Correction (A× B× C)	0.9683 ± 0.0300	0.9975 ± 0.0012	0.9950 ± 0.0280
Efficiency after corrections	0.70 ± 0.06%	3.33 ± 0.11 %	1.05 ± 0.10%
	K^+K^-	$\pi^+\pi^-$	
$\epsilon_{\rm raw}$	4.4 ± 0.1 %	4.2 ± 0.1 %	
$\epsilon_{\rm corrected}$ (K PID only)	0.9302±0.0600	N/A	
$\epsilon_{\rm corrected}$ (π PID only)	N/A	1.00 ± 0.04	
(A)$\epsilon_{\rm corrected}$ (K and π PID)	0.9302±0.0600	1.00 ± 0.04	
(B) π^0 (D^0) correction	N/A	N/A	
(C) Tracking correction	cancels	cancels	
Total Correction (A× B× C)	0.9302 ± 0.0600	1.00 ± 0.04	
Efficiency after corrections	4.13 ± 0.36%	4.20 ± 0.26%	

7.2.3 π^0 reconstruction efficiency corrections

The correction required for neutral pions is also a standard correction in *BABAR* analyses [26]. It is based on $e^+e^- \to \tau^+\tau^-$ events where the first τ is identified as decaying to $e\nu_\tau\bar{\nu}_e$. As with the tracking correction study this cleanly selects the τ pair and identifies the charge of the second τ. The second τ is then reconstructed decaying to $h^\pm\nu$ where in this case h is a $\pi^\pm$ or a $\rho^\pm$.

The efficiency correction is found by measuring a ratio of ratios. The first ratio

is

$$\frac{N_{\rm Data}(\tau \to \rho)}{N_{\rm MC}(\tau \to \rho)} = R_{\tau\to\rho}. \tag{7.12}$$

The number of successfully reconstructed events is N and the subscript indicates the result is from real data (Data) or from simulated events (MC). The second ratio is very similar,

$$\frac{N_{\rm Data}(\tau \to \pi)}{N_{\rm MC}(\tau \to \pi)} = R_{\tau\to\pi} \tag{7.13}$$

Because $\rho \to \pi\pi$ almost 100% of the time, the $\tau^{\pm} \to \rho^{\pm}$ reconstruction efficiency will be proportional to both the $\pi^{\pm}$ and the π^0 reconstruction efficiencies. The $\tau^{\pm} \to \pi^{\pm}$ reconstruction efficiency is only proportional to the $\pi^{\pm}$ reconstruction efficiency. This means that the ratio $R_{\tau\to\rho}/R_{\tau\to\pi}$ will give a good approximation to the relative π^0 reconstruction efficiency.

The value of this correction for each mode is given in Table 7.1. The correction is 0.9683 per neutral pion. This has an associated 3% systematic error. The correction for the π^0 from the K^{*-} is neglected because this π^0 is present in all modes under study and so any variation in efficiency will cancel.

7.2.4 Finding the effective efficiency to calculate $\mathcal{R}_{\pm}$

With the further efficiency corrections determined, the value of ω for the non-CP, CP-even and CP-odd modes can be calculated. The efficiency corrections are summarised in Table 7.1, and are combined with the branching ratios [12] and efficiencies of Table 5.4 to find ω for each mode. These values of ω are shown in Tables 7.2, 7.3 and 7.4 for $\omega_{\rm non-CP}$, $\omega_{\rm CP-odd}$ and $\omega_{\rm CP-even}$ respectively.

The ratio

$$\omega_{\rm non-CP}/\omega_{\rm CP-even} = 33.1 \pm 4.2,$$

while the value of

$$\omega_{\rm non-CP}/\omega_{\rm CP-odd} = 28.9 \pm 5.9.$$

Table 7.2: Calculating the relative efficiency of the non-CP modes.

	$K^-\pi^+$	$K^-\pi^+\pi^0$	$K^-\pi^+\pi^-\pi^+$
Corrected efficiency $\times 10^{-2}$ (A)	5.137 ± 0.321	2.430 ± 0.254	2.855 ± 0.293
$\mathcal{B}(D^0 \to \mathrm{X}) \times 10^{-2}$ (B)	3.8 ± 0.09	13.0 ± 0.8	7.46 ± 0.31
$\omega_i \times 10^{-3}$ (A×B)	1.95 ± 0.17	3.16 ± 0.53	2.13 ± 0.30
$\omega_{\mathrm{non-CP}} \times 10^{-3}$	7.24 ± 0.63		

Table 7.3: Calculating the relative efficiency of the CP-odd modes.

	$K^0_S\pi^0$	$K^0_S\phi$	$K^0_S\omega$
Corrected efficiency $\times 10^{-2}$ (A)	0.70 ± 0.06	3.33 ± 0.11	1.05 ± 0.10
$\mathcal{B}(D^0 \to \mathrm{X}) \times 10^{-2}$ (B)	1.3 ± 0.11	0.21 ± 0.06	0.85 ± 0.20
$\omega_i \times 10^{-3}$ (A×B)	0.09 ± 0.02	0.071 ± 0.02	0.09 ± 0.03
$\omega_{\mathrm{CP-odd}} \times 10^{-3}$	0.25 ± 0.04		

Table 7.4: Calculating the relative efficiency of the CP-even modes.

	K^+K^-	$\pi^+\pi^-$
Corrected efficiency $\times 10^{-2}$ (A)	4.13 ± 0.36	4.20 ± 0.26
$\mathcal{B}(D^0 \to \mathrm{X}) \times 10^{-3}$ (B)	3.89 ± 0.01	1.38 ± 0.05
$\omega_i \times 10^{-3}$ (A×B)	0.16 ± 0.07	0.06 ± 0.01
$\omega_{\mathrm{CP-even}} \times 10^{-3}$	2.19 ± 0.02	

7.3 Calculation of the GLW quantities

By taking the yields measured in Sections 6.5.4 and 6.5.5 and the values of ω measured in the previous section we can use Equations 7.10 and 7.11 to calculate the GLW quantities $\mathcal{A}_\pm$ and $\mathcal{R}_\pm$.

$$\begin{aligned} \mathcal{A}_+ &= -0.40 \pm 0.40 \text{ (stat)}, \\ \mathcal{A}_- &= -1.00 \pm 3.67 \text{ (stat)}, \\ \mathcal{R}_+ &= 2.06 \pm 0.80 \text{ (stat)}, \\ \mathcal{R}_- &= 0.19 \pm 0.50 \text{ (stat)}. \end{aligned}$$

7.4 Systematic Errors

In this section consideration is given to potential sources of systematic error. Systematic errors which affect both $\mathcal{A}_\pm$ and $\mathcal{R}_\pm$ are the yield estimation procedure and

the uncertainty due to non-resonant $B^- \to D^0 K\pi^-$ decays. $\mathcal{A}_\pm$ also suffers from a systematic error due to the potential of the detector to have different detection efficiencies for negative and positive particles. A source of error which only affects $\mathcal{R}_\pm$ is the calculation of ω. It is found that the dominant errors on this analysis are statistical and the uncertainty due to non-resonant decays. All others are small in comparison.

7.4.1 Yield estimation systematic error

The yield estimation strategy has errors associated with the uncertainty on the measurement of the fixed parameters of the yield estimation fit (Chapter 6) to $m_{\rm ES}$. This error affects the extraction of the yields and therefore the measurement of both $\mathcal{A}_\pm$ and $\mathcal{R}_\pm$. These errors are statistical in nature, but are included here for completeness.

To calculate the systematic error of a particular yield measurement, the fit is repeated with one of the fixed parameters varied by $\pm 1\sigma$. The difference in the resulting yield is recorded before resetting the fit to its original state and varying the next fixed parameter. This process is repeated until all fixed parameters have been varied. The parameters that are studied are the Argus shape (η), the mean of the background Gaussian and the mean and width of the signal Gaussian.

The differences found for each parameter are added in quadrature to give an overall estimate of the uncertainty on each measured yield. Included within this error is the uncertainty relating to the estimation of the size of the fake K^{*-} background.

When each parameter was varied for the CP-even and CP-odd modes, it was found that the resulting yield varied by no more than 0.2 events. This variation was small in comparison to the statistical uncertainty of each measurement which ranged from 1.7 to 3.6 events. This source of error has therefore been neglected for these modes.

The error on the measurement of the non-CP yield was found to be 10.5 events. This results in a systematic error on the calculation of $\mathcal{R}_+$ of 0.11 and a systematic on $\mathcal{R}_-$ of 0.01.

7.4.2 The systematic error on the calculation of ω

The systematic error on the calculation of ω arises from the uncertainty in the branching ratio measurements used and the corrected efficiencies. This error was calculated in Tables 7.2, 7.3 and 7.4 for $\omega_{\mathrm{non-CP}}$, $\omega_{\mathrm{CP-odd}}$ and $\omega_{\mathrm{CP-even}}$ respectively. The error on $\omega_{\mathrm{non-CP}}/\omega_{\mathrm{CP-odd}}$ leads to a systematic error of 0.04 on $\mathcal{R}_-$ while the error on $\omega_{\mathrm{non-CP}}/\omega_{\mathrm{CP-even}}$ gives an error of 0.26 on $\mathcal{R}_+$.

7.4.3 Charge bias

There is a potential for the detector to have a different detection efficiency for a positive particle than for an otherwise identical negative particle. This effect is expected to be small but to estimate it we can use the non-CP modes which should show no charge asymmetry.

The non-CP modes are studied with the same cuts as used in the analysis. The charge of the events found in the region $5.2 < m_{\mathrm{ES}} < 5.3$ is recorded. The number of positive events found was 820 while the number of negative events found was 766. This gives an asymmetry of 3.4% which when multiplied by the central value of $\mathcal{A}_+$ gives a systematic error due to this uncertainty of 0.01. For $\mathcal{A}_-$ the systematic error is 0.03.

7.4.4 Non-resonant $B^- \to D^0 K^- \pi^0$ background

It was shown in Section 2.5 that this analysis suffers from a non-resonant background due to $B^- \to D^0 K^- \pi^0$ decays. This background has a branching ratio that is not measured and is expected to introduce an additional strong phase that could interfere with the extraction of the weak phase γ.

To understand the effects of this background on the measurement of the GLW quantities $\mathcal{A}_\pm$ and $\mathcal{R}_\pm$ a study was performed by S.Ricciardi [27]. An overview of this study is given here because it leads to one of the dominant systematic errors in this analysis. The study modelled the effect of the non-resonant background by making use of the expected difference between the resonant and non-resonant decays when looking at the helicity distribution (Section 5.1) of the K^{*-} and the line-shape of the invariant K^{*-} mass distribution.

The helicity distribution of signal events should follow a $\cos^2\theta$ distribution while the non-resonant background should show a broad distribution. This angular depen-

dence is because the K^{*-} is a spin one [12] particle which is reconstructed decaying into two spin 0 particles. The K^{*-} mass distribution of the signal is modelled by a Breit-Wigner [12] while the non-resonant background should show a broad spectrum. The Breit-Wigner is defined as

$$BW(m_{K^-\pi^0}) = -\frac{m_{K^*}\Gamma}{m_{K^-\pi^0} - m_{K^*}^2 + im_{K^*}\Gamma} \tag{7.14}$$

and is a function of the invariant mass of the $K^-\pi^0$ system (denoted by $m_{K^-\pi^0}$). The natural width of the K^{*-} (Γ) is 50.8 MeV [12] and the mass of the K^{*-} (m_{K^*}) is 0.892 MeV [12].

From the Feynman diagrams for the $B^- \to D^0K^{*-}$ and $B^- \to K^-\pi^0K^{*-}$ decays a general amplitude parameterisation ($a_{\rm tot}$) can be formed. This incorporates the dependence on the K^{*-} helicity and invariant mass line-shape of the resonant ($a_{\rm Res}$) and non-resonant ($a_{\rm NR}$) modes:

$$a_{Res} = A\sqrt{3}\cos\theta\left[1 + r_B e^{i(\delta-\gamma)}\right] BW(m_{K^-\pi^0}), \tag{7.15}$$

$$a_{NR} = B\rho_c e^{i\Delta_c}\left[1 + r_B e^{i(\delta-\gamma)}\frac{\rho_u}{\rho_c}e^{i(\Delta_u-\Delta_c)}\right], \tag{7.16}$$

$$a_{Total} = a_{Res} + a_{NR}. \tag{7.17}$$

This parameterisation is dependent on $\cos\theta$ which is the angular dependence of the helicity distribution. The model also depends on the strong and weak phases, δ and γ, and r_B the ratio of the amplitude of $b \to u$ and $b \to c$ transitions. An additional four parameters are also required, the first two new parameters are

$$\rho_c = \frac{|A(B^- \to D^0K^-\pi^0)|}{|A(B^- \to D^0K^{*-})|} \tag{7.18}$$

$$\rho_u = \frac{|A(B^- \to \overline{D}^0K^-\pi^0)|}{|A(B^- \to \overline{D}^0K^{*-})|} \tag{7.19}$$

which are the ratios of the amplitude of the three-body background to the signal amplitude for $b \to c$ and $b \to u$ processes respectively. The second two parameters are Δ_c and Δ_u which are the phase differences between the three-body background and the signal. A and B are normalisation constants.

When modelling the non-resonant amplitude (a_{NR}) an ansatz is made to simplify the model where

$$\frac{\rho_u}{\rho_c} e^{i(\Delta_u - \Delta_c)} = \lambda = \frac{1 + \frac{e^{i\eta}}{3}}{e^{i\phi} + \frac{e^{i\eta}}{3}}. \tag{7.20}$$

Section 2.4 showed how $\mathcal{R}_\pm$ can be derived from the rates of decays of the type $B^- \to D^0 K^{*-}$. In a similar manner a modified $\mathcal{R}_\pm$ can be formed using the combined resonant and non-resonant amplitude a_{Total} from Equation 7.17.

$$R_{CP}^{Total} = \frac{\Gamma(B^- \to D^0_\pm[Res + NR]) + \Gamma(B^+ \to D^0_\pm[Res + NR])}{\Gamma(B^- \to D^0[Res + NR]) + \Gamma(B^+ \to \overline{D}^0[Res + NR])} \tag{7.21}$$

where the rates are of the form

$$\Gamma(B^- \to D^0_\pm[Res + NR]) = \int_{-0.4}^{1} d\cos\theta \int dm_{K^-\pi^0} |a_{Total}|^2. \tag{7.22}$$

The integral over the $\cos\theta$ dependence is made over the range $-0.4 < \cos\theta < 1$ because the events with a helicity less than -0.4 are rejected by the final selection criteria in this analysis. An integral over $m_{K^-\pi^0}$, the mass of the K^- π^0 system, is also performed. The systematic error is found by varying the values of all free parameters within their allowed ranges such that the error is given by

$$(\text{Max}\left\{\Delta_c, \delta, \lambda\right\}\left[R_{\text{Total}} - R_{\text{Res}}\right] - \text{Min}\left\{\Delta_c, \delta, \lambda\right\}\left[R_{\text{Total}} - R_{\text{Res}}\right])/2. \tag{7.23}$$

The fixed parameters are: γ set to one radian, r_B set to 0.2 and ρ_c set to 0.44.

The value of ρ_c is based upon the conservative value used by the sister analysis [15] of 0.22. The value we use is doubled to take into account the expectation that this analysis will see a larger proportion of non-resonant events as there are roughly twice as many Feynman diagrams contributing. This is a naive approximation, but it is expected to overestimate, and hence is conservative.

The same procedure of constructing measurables based upon non-resonant modified amplitudes is repeated to find the systematic error on $\mathcal{A}_\pm$. The systematic error resulting from this model was found to be 0.19 for $\mathcal{A}_+$ and $\mathcal{A}_-$ 0.30 for $\mathcal{R}_+$ and $\mathcal{R}_-$.

7.4.5 Summary of systematic errors

The systematic errors, including the total error, on the measurement of $\mathcal{A}_\pm$ and $\mathcal{R}_\pm$ are summarised in Tables 7.5 and 7.6. The dominant systematic error in all cases is that due to the non-resonant background studied in Section 7.4.4. However the largest single source of error on the measurements presented is the statistical error.

Table 7.5: Summary of the systematic errors on $\mathcal{A}_+$ and $\mathcal{A}_-$.

Source	$\mathcal{A}_+$ error	$\mathcal{A}_-$ error
Fit	0	0
Charge Bias	0.01	0.03
Non-Res	0.19	0.19
Total	0.19	0.19

Table 7.6: Summary of the systematic errors on $\mathcal{R}_+$ and $\mathcal{R}_-$.

Source	$\mathcal{R}_+$ error	$\mathcal{R}_-$ error
Fit	0.11	0.01
ω_{Rel}	0.26	0.04
Non-Res	0.30	0.30
Total	0.41	0.30

7.5 Summary of results

This analysis has measured the four GLW quantities:

$$\begin{aligned}
\mathcal{A}_+ &= -0.40 \pm 0.40\ (\text{stat})\ \pm\ 0.19\ (\text{syst}),\\
\mathcal{A}_- &= -1.00 \pm 3.67\ (\text{stat})\ \pm\ 0.19\ (\text{syst}),\\
\mathcal{R}_+ &= 2.06 \pm 0.80\ (\text{stat})\ \pm\ 0.41\ (\text{syst}),\\
\mathcal{R}_- &= 0.19 \pm 0.50\ (\text{stat})\ \pm\ 0.30\ (\text{syst}).
\end{aligned}$$

It can be seen that the statistical error dominates the precision of these measurements and that the uncertainty due to the non-resonant background dominates all other systematics errors which are comparably insignificant. In the next chapter, the

results are discussed. They are put into the context of other measurements of the GLW quantities and the future of the analysis is considered.

Chapter 8

Summary and Conclusions

The previous chapter took the yields measured of each type of D^0 CP eigenstate and used these to calculate four GLW quantities: $\mathcal{A}_+$, $\mathcal{A}_-$, $\mathcal{R}_+$ and $\mathcal{R}_-$. In this chapter a comparison of the results with similar analyses is made. The future of GLW measurements is discussed before a final summary of the analysis is presented.

8.1 A comparison with other measurements

The GLW method has been used by several other analyses which have differed from this analysis by using either decays containing a D^{*0}, or by reconstructing the K^{*-} decaying to $K^0_S\,\pi^-$. In fact, this analysis is the first to use the $K^{*-} \to K^-\pi^0$ decay mode with the GLW method.

The GLW quantities measured by analyses which use $B^- \to D^0K^{*-}$ modes where the $K^{*-} \to K^0_S\pi^-$ are presented in Table 8.1. This thesis has presented results which are compatible with those of the other analyses. It can be seen that this analysis suffers from comparatively large errors. The larger systematic error is due to the domination of the uncertainty related to the non-resonant background. The larger statistical error arises because, although this analysis benefits from larger branching ratios, the requirement to reconstruct the π^0 from the K^{*-} leads to a lower reconstruction efficiency. Another reason is the lower than expected yields measured in the CP-odd modes.

The measurements made by this analysis have been important because within a large collaboration a variety of modes must be studied. The results presented will contribute to the effort to constrain the size of the angle γ as well as help in

resolving the ambiguity that arises from the symmetry of the δ and γ terms in the GLW method.

Table 8.1: The world averages of $\mathcal{A}_{\pm}$ and $\mathcal{R}_{\pm}$. The figures for *BABAR* 2005 and Belle 2003 are taken from [15] and [16] respectively.

Result	$\mathcal{A}_+$	$\mathcal{A}_-$
This thesis	-0.40 ± 0.40± 0.19	-1.00 ± 3.67 ± 0.19
BABAR 2005	-0.08 ± 0.19± 0.08	-0.26 ± 0.40 ± 0.12
Belle 2003	-0.02 ± 0.33 ± 0.07	0.19 ± 0.50 ± 0.04
Average	-0.06 ± 0.18	-0.08 ± 0.32
Result	$\mathcal{R}_+$	$\mathcal{R}_-$
This thesis	2.06 ± 0.80 ± 0.41	0.19 ± 0.50 ± 0.30
BABAR 2005	1.96 ± 0.40 ± 0.11	0.65 ± 0.26 ± 0.08
Belle 2003	Unmeasured	Unmeasured
Average	1.96 ± 0.41	0.65 ± 0.27

8.2 The future for this analysis and the GLW method

Measurement of the angle γ is an important part of testing the Standard Model, and therefore further study is desirable. Research in this area is due to continue with publications by the *BABAR* collaboration using the larger data sets that will be available in the future. With a current data set in the region of $0.5\,\mathrm{ab}^{-1}$ and the *BABAR* detector approved to collect another $0.5\,\mathrm{ab}^{-1}$ by the end of 2008, the measurement of γ with the GLW method looks to be dominated by analyses which will combine the decay modes of $B^- \to D^{(*)0}K^{(*)-}$. This analysis has shown that it can contribute information to aid the constraint of the angle γ and so should be included in these future studies.

The key to making full use of the modes studied here in these efforts will be to reduce the non-resonant systematic error. This could be done by making a measurement of the non-resonant decay in order to increase our understanding. As well as aiding this GLW analysis, the non-resonant modes could themselves make a measurement of the angle γ [28]. It may also be possible to reduce the size of this systematic error by revisiting the event selection criteria. The selection criteria used in this analysis were optimised before the studies in Section 7.4.4 found that

the non-resonant background led to large systematic errors. The asymmetric cut applied to the helicity angle distribution of the K^{*-} (defined in Section 5.1) prevented a number of terms cancelling in the model produced by S. Ricciardi [27]. By changing the single cut to two symmetric cuts, or by removing the cut on this distribution altogether, it may be possible to trade a loss in the signal significance with a greater gain in the reduction of the systematic error from this source.

In the medium to long term the best chance for large increases in the precision of measurements of γ rests with a new generation of experiments such as LHCb and a Super B-factory. LHCb has the potential to measure γ with the GLW method to a precision of 5° [29] while the best estimates for a Super B-factory give a statistical uncertainty of 2° [30]. The estimate of the precision of the Super B-factory comes with a caveat that at such an early stage in the process of developing an experiment, estimates are uncertain. These precision estimates can be compared with today's combined direct measurement precision of 17° [18].

8.3 Final overview

This thesis has presented a study of the decay $B^- \to D^0 K^{*-}$ and its charge conjugate, $B^+ \to \overline{D}^0 K^{*+}$. The goal was to provide information on the matter anti-matter asymmetry known as CP violation by measuring the difference in decay rates of B^+ and B^- mesons. By using the Gronau-London-Wyler (GLW) method, the measurement of these decay rates for various decays of the D^0 meson were attempted. A set of selection criteria were develop to separate these signal modes from background and a yield estimation strategy was developed. Using these yields, this analysis successfully measured the GLW quantities $\mathcal{A}_\pm$ and $\mathcal{R}_\pm$. Using a dataset of 204 million $B\overline{B}$ pairs, the value of these quantities were calculated to be:

$$\begin{aligned}
\mathcal{A}_+ &= -0.40 \pm 0.40\ (\text{stat})\ \pm\ 0.19\ (\text{syst});\\
\mathcal{A}_- &= -1.00 \pm 3.67\ (\text{stat})\ \pm\ 0.19\ (\text{syst});\\
\mathcal{R}_+ &= 2.06 \pm 0.80\ (\text{stat})\ \pm\ 0.41\ (\text{syst});\\
\mathcal{R}_- &= 0.19 \pm 0.50\ (\text{stat})\ \pm\ 0.30\ (\text{syst}).
\end{aligned}$$

These measurements can be added to those of other GLW analyses in order to add information to the constraint of the angle γ of the unitarity triangle.

Bibliography

[1] I. J. R. Aitchison and A. J. G. Hey, Bristol, UK: Hilger, 1989 P.571

[2] F. Halzen and A. D. Martin, New York, USA: Wiley, 1984 P.396

[3] I. I. Bigi and A. I. Sanda, CP Violation, Cambridge, 2000

[4] A. G. Cohen, CP Violation and the origins of matter, Proceedings of the 29$^{\text{th}}$ SLAC Summer Institute, 2001

[5] A. G. Cohen, A. De Rujula and S. L. Glashow, Astrophysics. J. **495**, 1998, P.539

[6] P. F. Harrison, H. R. Quinn et al, (*BABAR*), The *BABAR* physics book: Physics at an asymmetric B-factory, **SLAC-R-504**, 1998

[7] M. Gronau and D. Wyler, Phys. Lett. **B265**, 1991, P.172

[8] M. Gronau and D. London, Phys. Lett. **B253**, 1991, P.483

[9] M. Gronau, Phys. Rev. **D58**, 1998, 037301

[10] M. Gronau Phys. Lett. **B557**, 2003, P.198

[11] I. I. Bigi and A. I. Sanda, Phy. Lett. **B 211**, 1988, P.213

[12] S. Eidelman et al, (Particle Data Group), Phys. Lett. **B 592**, 2002, P.1

[13] T. R. McMahon et al, (*BABAR*), Physical Review D69, **051101**, 2004

[14] B. Aubert et al (*BABAR*), Phys. Rev. **D73**, 111104, 2006

[15] B. Aubert et al (*BABAR*), Phys. Rev. **D72**, 071103, 2005

[16] K. Abe et al (Belle), BELLE-CONF-0316, 2003

[17] The HFAG Collaboration, http://www.slac.stanford.edu/xorg/hfag/triangle/summer2005/index.shtml

[18] The UTFit collaboration, http://utfit.roma1.infn.it/gamma/ckm-gamma.html

[19] The UTFit collaboration, http://utfit.roma1.infn.it/ckm-results/ckm-results.html

[20] PEP-II: An Asymmetric B Factory, Conceptual Design Report, **SLAC-R-418**, 1993

[21] B. Aubert et al (*BABAR*), Nuclear Instruments and Methods in Physics Research A, **479**, 2002, P.1

[22] *BABAR* event selection, http://www.slac.stanford.edu/BFROOT/www/doc/workbook/eventinfo/BtaCandInfo/CandLists.html

[23] R. A. Fisher, Annal Eugen. **7**, 1936, P.179

[24] H. Albrecht et al, (ARGUS Collaboration), Phys. Lett. **B 185**, 1987, P.218

[25] T. Allmendinger et al, Tracking efficiency studies, *BABAR* internal note, BAD 867.

[26] A. T. Allen et al, A measurement of π^0 efficiency using $\tau \to \rho\nu$ and $\tau \to \pi\nu$ decays, *BABAR* internal note, BAD 870.

[27] S.Ricciardi, Private communication, 2005

[28] T. Gershon, Workshop on the CKM Unitarity Triangle, IPPP Durham, eConf, **C0304052:WG406**, 2003.

[29] J. Libby, $B \to DK$ measurements of γ, LHCb Comprehensive Review, http://indico.cern.ch/conferenceDisplay.py?confId=741, 2006

[30] A. Soffer, γ from $B \to DK$, $B \to D\pi$ and variants, **SLAC-R-709**, P.158, 2004